

THE SOUND OF OSCILLATING AIR JETS: PHYSICS,
MODELING AND SIMULATION IN FLUTE-LIKE INSTRUMENTS

A DISSERTATION
SUBMITTED TO THE DEPARTMENT OF MUSIC
AND THE COMMITTEE ON GRADUATE STUDIES
OF STANFORD UNIVERSITY
IN PARTIAL FULFILLMENT OF THE REQUIREMENTS
FOR THE DEGREE OF
DOCTOR OF PHILOSOPHY

Patricio de la Cuadra

December 2005

© Copyright by Patricio de la Cuadra 2006
All Rights Reserved

I certify that I have read this dissertation and that, in my opinion, it is fully adequate in scope and quality as a dissertation for the degree of Doctor of Philosophy.

Chris Chafe Principal Co-Advisor

I certify that I have read this dissertation and that, in my opinion, it is fully adequate in scope and quality as a dissertation for the degree of Doctor of Philosophy.

Benôt Fabre Principal Co-Advisor

I certify that I have read this dissertation and that, in my opinion, it is fully adequate in scope and quality as a dissertation for the degree of Doctor of Philosophy.

Julius Smith

I certify that I have read this dissertation and that, in my opinion, it is fully adequate in scope and quality as a dissertation for the degree of Doctor of Philosophy.

Jonathan Berger

Approved for the University Committee on Graduate Studies.

Abstract

Flute-like instruments share a common mechanism that consists of blowing across one open end of a resonator to produce an air jet that is directed towards a sharp edge. Analysis of its operation involves various research fields including fluid dynamics, aero-acoustics, and physics. An effort has been made in this study to extend this description from instruments with fixed geometry like recorders and organ pipes to flutes played by the lips. An analysis of the jet's response to a periodic excitation is the focus of this study, as are the parameters under the player's control in forming the jet.

Experimental measurements are done in which the jet is excited with a controlled excitation consisting of two loudspeakers in opposite phase, which not only provides accurate control over the excitation but also allows for repeatability of the experiments. A Schlieren system is used to visualize the jet, and image detection algorithms are developed to extract quantitative information from the images. In order to study the behavior of jets observed in different flute-like instruments, several geometries of the excitation and jet shapes are studied. The obtained data is used to propose analytical models that correctly fit the observed measurements and can be used for simulations.

The control exerted by the performer on the instrument is of crucial importance in the quality of the sound produced for a number of flute-like instruments. The case of the transverse flute is experimentally studied. An ensemble of control parameters are measured and visualized in order to describe some aspects of the subtle control attained by an experienced flautist. Contrasting data from a novice flautist are compared. As a result, typical values for several non-dimensional parameters that

characterize the normal operation of the instrument have been measured, and data to feed simulations has been collected.

The information obtained through experimentation is combined with research developed over the last decades to put together a time-domain simulation. The model proposed is one-dimensional and driven by a single physical input. All the variables in the model are expressed in terms of pressure which allows for implementation and control in real-time. The model provides both a testbed to compare and validate measurements as well as a highly configurable and real-time musical instrument.

Acknowledgment

This research is the fruit of a collaboration between three laboratories, CCRMA (Center for Computer research in music and acoustic) at Stanford University, LAM (Laboratoire d'Acoustique Musicale) and IRCAM (Institut de Recherche et Coordination Acoustique/Musique) in Paris. This framework has been very enriching for me and I must express my gratitude to many persons from the three institutions without whom this work would not have been possible.

First of all I wish to express my sincere gratitude to Benôt Fabre from LAM, who guided this work, listened patiently to my questions and always had enlightened suggestions to make. His generosity, patience, hospitality, care, commitment and friendship enormously helped to make this thesis possible and an enjoyable experience for me.

I am greatly indebted to the Department of Music and CCRMA for their financial support throughout my studies at Stanford. Chris Chafe's endless enthusiasm, support and flexibility are greatly appreciated. Thanks to all the people who make CCRMA a great place to work. Especially to my friends Yi-Wen Liu, his mathematical talents have help me more than once, Craig Sapp and Scott Wilson our computer gurus and Jonathan Abel for his useful comments and help.

From the IRCAM, I wish to thank René Caussé who friendly gave me the opportunity to join his research group. Gérard Bertrand and Alain Terrier, masters of building devices and great French teachers and to my friends Christophe Vergez and André Almeida with whom we shared many good moments and stimulating discussions.

This work is dedicated to my family and very especially to my dearest wife Gabriela, who has always been there with her love, inspiration and encouragement.

Contents

Abstract	v
Acknowledgment	vii
1 Introduction	1
1.1 Motivation	1
1.2 Some history	2
1.3 Characteristic lengths	4
1.4 Lumped-elements or integral models?	6
1.4.1 Lumped-elements models	7
1.4.2 Integral models	7
1.5 What to model?	8
1.6 Thesis layout	8
2 Jet analysis	11
2.1 Introduction	12
2.1.1 Basic operation	12
2.1.2 Flutes geometry	12
2.1.3 Lumped vs Integral models	13
2.1.4 Limitation of current models and Motivation	13
2.1.5 Chapter layout	14
2.2 Jet instability	14
2.2.1 Jet Operation	14
2.2.2 Jet velocity profile	16

2.2.3	Linear theory	18
2.2.4	Experimental setup	22
2.2.5	Image data analysis	26
2.2.6	Influence of the channel length	28
2.2.7	Influence of the channel exit geometry	33
2.2.8	Discussion	34
2.3	Boundaries of the linear description	36
2.3.1	Discrete vortices model	36
2.3.2	Experimental protocol	40
2.3.3	Perturbation at the transition	40
2.3.4	Perturbation at the flue exit	44
2.3.5	Discussion	44
2.4	Conclusion	47
3	Control parameters	49
3.1	Introduction	50
3.2	Basic flute model	51
3.3	Control parameters and experimental setup	54
3.4	Data processing	55
3.5	Experienced flautist analysis	57
3.5.1	Three cases : D major scale, diminuendo and octaves	58
3.5.2	Global analysis	61
3.6	Comparison between a novice and an experienced flautist	65
3.6.1	Sound production	67
3.6.2	Control of the sound quality	67
3.7	Discussion	72
4	Real-time simulation	77
4.1	Introduction	77
4.2	Resonator	78
4.2.1	Visco-thermal Losses	79
4.2.2	Radiation and reflection from the end of the bore	80

4.2.3	Frequency range	83
4.2.4	Parametric implementation	83
4.2.5	Signal flow diagram	84
4.2.6	Input impedance	86
4.3	Excitation	87
4.3.1	Attacks	88
4.3.2	Jet formation	89
4.3.3	Receptivity and Instability	90
4.3.4	Sources	94
4.4	Implementation	99
4.4.1	Pitch adjustment	100
4.4.2	Flute laboratory	101
4.4.3	Pd/Max-MSP external object	102
4.5	Conclusions	104
5	Ouldémé flutes	105
5.1	Introduction	105
5.1.1	Experimental protocol	106
5.2	Investigation on Ouldémé Flute Functioning	106
5.2.1	Description of the way of playing	106
5.2.2	Adding water	107
5.2.3	Turbulent jet	108
5.2.4	Discussion - Toward a model of the Ouldémé flute	111
5.3	The model - Implementation	112
5.4	Adjusting and controlling the model	113
5.5	Conclusion	114
A	Understanding the Schlieren method	117
A.1	Fluid flow as a refractive index field	117
A.1.1	Relation between fluid density ρ and refractive index n	118
A.1.2	Deflection of a light ray in an inhomogeneous density field	119
A.2	Schlieren method	121

A.2.1 Analytical description	122
A.2.2 Geometric description	124
B Image detection algorithms	125
B.1 Image processing	125
B.2 Cross-correlation method	125
B.2.1 The algorithm	126
B.2.2 Position of the reference image	128
B.2.3 Phase analysis	129
B.3 Morphological method	130
B.4 Harmonic analysis method	131
B.5 Data analysis	133
B.6 Methods comparison	134
Bibliography	139

List of Figures

1.1	Excitation parameters	4
1.2	Approximate range of operation of the recorder, European transverse flute and organ in a W/h vs. Reynolds space. For the transverse flute, the player can move over the whole range with one instrument while in the organ several pipes are required to cover the range.	6
2.1	Jet emerging from the formation channel, oscillating and traveling towards the labium	12
2.2	Simplified segregation of the jet into linear growth, vortex street and later turbulences	15
2.3	Jet coming out from a long channel (left) is smoother than one coming from a short channel (right)	16
2.4	Changes in the jet profile as it travels away from the flue exit	17
2.5	Comparison between the three jet displacement models: Fletcher's model (solid line), Fletcher's model simplified by Verge (dashdot line) and experimentally observed oscillations (dashed line)	21
2.6	Air jet submitted to an acoustic excitation generated by loudspeakers. Acoustic velocity measured through the pressure gradient measured with two microphones (not in scale)	23
2.7	Comparison between CO ₂ and air, for $U_j = 5, 10$ and 20 m/s.	24
2.8	Schlieren system.	25

2.9	Images obtained via Schlieren technique. Reynolds: 200, Jet speed: 3 m/s, Excitation freq.: 108.28 Hz, Strouhal: 0.225. $V_{ac}/U_j = 0.005$. One cycle of oscillation, the acoustic velocity phase is 0 (a), $\pi/2$ (b), π (c), $3\pi/2$ (d). The two shear layers appear with opposite light refractive gradient, so that the upper shear layer gets darker while the lower shear layer gets lighter than the average gray level.	26
2.10	Position of jet detected by cross-correlation method. Time axis corresponds to frame times in seconds.	27
2.11	a): Schlieren image with the detection of position using the cross-correlation method. <i>Reynolds</i> = 200 and <i>Strouhal</i> = 0.225. Excitation frequency = 108 Hz, $V_{ac}/U_j = 0.005\%$. b) Top: (thick) Amplitude of the detected sinusoids, (thin) exponential fit. Bottom: (thick) Phase of detected sinusoids, (thin) linear fit.	29
2.12	Long and short formation channels.	30
2.13	CO ₂ jet profile. a) short channel, b) long channel. Jet speed= 5, 10, 20 m/s from top down. Nolle profiles (eq.2.2) are fit to the curves finding b and n for each curve	31
2.14	a) Dimensionless convection velocity and b) amplification coefficient, flue exit short (o), squared or long(x)	32
2.15	a) Dimensionless convection velocity and b) amplification coefficient for a long channel (solid line) and short channel (dashed line) calculated using Rayleigh's equation	33
2.16	Geometry of the three flue exits used, from left to right: Squared, Rounded, 45 degrees.	34
2.17	a) Dimensionless convection velocity and b) amplification coefficient, flue exit squared (o), rounded (x) and 45 degrees (+).	35
2.18	a) Dimensionless convection velocity and b) amplification coefficient as functions of the dimensionless acoustic velocity excitation V_{ac}/U_j	35
2.19	Schlieren images with position of the place where the jet breaks into vortices x_c and the amplitude of oscillation at that point η_c	36
2.20	Holger's sketch for vortex formation	37

2.21	Non-dimensional height of the jet perturbation at the jet transition ($H/2h$) as function of Strouhal. Sensitivity analysis with respect to γ ($b = \gamma * h$) and with respect to the exponent n of the Nolle profile (eq.2.2) for γ fixed = 0.5	39
2.22	Approximate values for η_c and h shown with a Schlieren image	40
2.23	Images obtained via Schlieren technique.	41
2.24	Model estimation for the jet displacement at the transition point η_c , eq.2.16 (solid line) and data obtained through experimentation for flue exits Squared (o), Rounded (x) and 45 Degrees (+)	42
2.25	a) Displacement of the jet at the transition point η_c . b) Distance from the flue exit to the transition point on the jet x_c . Flue exit squared. Reynolds = 200	43
2.26	a) Displacement of the jet at the transition point η_c . b) Distance from the flue exit to the transition point on the jet x_c . Flue exit squared. Reynolds = 200. Frequencies 108, 144 and 208 Hz	45
2.27	Perturbation at the jet origin η_0 as function of Stouhal. Reynolds = 200, flue exits Squared (o), Rounded (x) and 45 degrees (+)	46
2.28	a) Perturbation at the jet origin η_0 as function of the non-dimensional acoustic velocity V_{ac}/U_j . b) Phase difference between the acoustic excitation V_{ac} and the jet oscillation at the origin η_0 . Reynolds = 200. Frequencies 108, 144 and 208 Hz	46
3.1	General description of flutes operation	52
3.2	Experimental setup.	56
3.3	Image captured by the camera with detection of lips hole and flue-labium distance, showing on the right of th picture the 45 mirror that allows to measure simultaneously lip opening and lip-edge distance.	56
3.4	Parameters measured and calculated for the experienced player F_A playing a slurred D major scale from D3 (293Hz) to A4 (880Hz)	59
3.5	Parameters measured and calculated for the experienced player F_A playing a B4, diminuendo	60

3.6	Parameters measured and calculated for the experienced player F_A playing octave intervals : D3-D4 ; E3-E4 ; F3-F4 ; G3-G4 with medium dynamics (<i>mf</i>)	62
3.7	Global dependency between a) Jet velocity U_j and b) Jet length W with the frequency played. Ascending chromatic scale (+) and diatonic scale (o)	63
3.8	Global dependency between a) Flow Q and b) Str_W with the frequency played. Ascending chromatic scale (+) and diatonic scale (o)	64
3.9	Collapsed data from several musical exerpts. a) Re vs. W/h b) Str_h vs. Str_W	66
3.10	a) Jet velocity U_j and b) Jet length W as functions of frequency. Octave series, experienced flautist (+), novice (o)	68
3.11	Str_W as function of frequency. Octave series, experienced flautist (+), novice (o)	69
3.12	a) Lips surface S_m and b) Flow Q_j as function of frequency. Octave series, experienced flautist (+), novice (o)	70
3.13	a) Re and b) Radiated power over power of the jet flow $\frac{P_{rad}}{P_p}$ as function of frequency. Octave series, experienced flautist (+), novice (o)	71
3.14	Acoustic pressure inside the mouth. Octave series, experienced flautist (+), novice (o)	73
4.1	Resonator from a transverse type flute	78
4.2	Optimized implementation for a three-port junction	79
4.3	Visco-thermal losses for a 60 cm cylinder with 9 mm radius.	81
4.4	Reflection coefficient for a cylinder of radius = 9 mm	82
4.5	Comparison between reflection and visco-thermal losses for a cylinder of 9mm radius and 60 cm length	84
4.6	Reflection frequency response obtained by varying the parameter a	85
4.7	Block diagram of the flute model resonator	86
4.8	Input impedance of the three-tubes resonator model	87
4.9	Organ pipe geometry.	88

4.10	One-dimensional models for the impedance seen by the jet at the flue exit	89
4.11	Measured values for (top) the convection velocity times jet height (αh) and (bottom) the amplification growth over jet velocity (c_p/U_j) as function of Strouhal number ($\omega h/U_j$).	92
4.12	Jet filter frequency response projected in two peak and one shelf filter, for a $U_j = 20m/s, x = 4.5mm$ and $h = 1mm$	93
4.13	Hyperbolic tangent stretched with the factor ψ	95
4.14	Contour of acoustic pressure (relative peak values) during edge-tone generation, measured by Coltman [16]	96
4.15	Comparison between the equi-potential and streamlines produced by a doublet and a dipole. a) Dipole streamlines; b) Dipole equi-potential lines; c) Doublet streamlines; d) Doublet equi-potential lines.	97
4.16	Sources detail	99
4.17	Code structure	100
4.18	Excitation widget	101
4.19	Resonator widget	102
4.20	Time-domain visualization widget	103
4.21	Frequency-domain visualization widget	103
4.22	pd patch with external object of the flute model	104
5.1	Ouldémé flutists.	107
5.2	Center line detection by image processing	109
5.3	Jet under acoustic excitation by loudspeakers. From top to bottom: $Re = 200, 500$ and 3000	109
5.4	Influence of Reynolds number (Re) over the speed of the perturbations(c_p/U_j) for a constant Strouhal number ($Str=0,018$).	110
5.5	Influence of Strouhal number over adimensional amplitude, for a constant Reynolds number ($Re = 2600$).	111
5.6	Synthetic flute with sensors.	114
5.7	Ouldémé flute players using synthetic flutes.	115

A.1	Deflection of a light ray in an inhomogeneous test object	120
A.2	Schlieren basic implementation	122
A.3	Shift of slit-shaped light source image in the plane of the schlieren knife edge	123
A.4	Idealyzed triangular jet traveling perpendicular to the plane shows how the density changes are converted into lighth intensity in the screen . .	124
B.1	Intensity level of a single column from a Schlieren image	126
B.2	Curve obtained from a cross-correlation of the same column in different moments of the sequence	127
B.3	Position of jet, excitation frequency = 532.28 Hz	128
B.4	The phase is preserved using the cross-correlation algorithm	129
B.5	Original Schlieren image superimposed with edge detection (black line) and median line (white line).	131
B.6	Evolution of one pixel $c(x, y, t)$ in time	132
B.7	Continuous value $\bar{c}(x, y)$ for the oscillation of each pixel in time . . .	132
B.8	Amplitude of the fitting sinusoid to each pixel $ \hat{c}_n(x, y) $	133
B.9	Integrated amplitudes along the columns, values for the first four har- monics. Linear amplitude	134
B.10	Fitted position of jet, excitation frequency = 532.28 Hz	135
B.11	Amplitude and phase of the jet transverse displacement of the jet using the cross correlation method (pink line) and the morphological method (green line), excitation frequency = 448.28 Hz	136
B.12	Amplitude and phase of the jet transverse displacement of the jet using the cross correlation method (pink line) and the morphological method (green line), excitation frequency = 1760.30 Hz, Turbulent jet (Re=3000).138	

Chapter 1

Introduction

1.1 Motivation

Physical modeling of instruments from the flute family is the main subject of this thesis. Flutes may be the oldest tunable human instruments [25] and are present in many cultures around the world. This is probably because of their simple principle of operation that consists of blowing across an open end of a resonator creating a jet that is directed towards a sharp edge [30].

Flutes present an enormous variety in both geometry and playing technique. Some provide soft and pure tones like recorders and ocarinas, while others can sound loud and noisy like zamponas and shakuhachis. They differ in the shape of the resonator. Most are cylindrical although there are also conical and even spherical. But the most important differences are due to the excitation mechanisms. The air jet is created in a formation channel whose geometry can be fixed, like in organ pipes and recorders, or completely adjustable like in lip-played instruments. The speed of the jet also contributes to the differences. The jet can be used in its sub-laminar, laminar or turbulent regimes. Some flutes can utilize all the regimes in their normal operation such as the transverse flute. It produces whistle tones which are obtained with sub-laminar flow, pianissimos and pianos with laminar jets, and fortes and very high pitches with turbulent jets. Although many aspects of the flute instruments are common to most flutes, this thesis is centered in the european transverse flute since it

encapsulates a rich variety of sound production and, because of its complexity, there is comparatively little research devoted to it.

One of the reasons that makes physical modeling, and particularly flute physical modeling attractive is that it brings together aspects of several domains such as fluid dynamics, aeroacoustics, signal processing, physics, experimentation, music and programming. From a musical point of view, aside from recreating sounds from existing flutes, it could lead to a rich production of new sounds that, since they are based on physical descriptions, remain close to sounds we find in nature. Other sound synthesis techniques are sometimes judged inexpressive for being strange to our natural hearing experiences. It also could provide ideas to improve the design of existing instruments. The empirical optimization carried out by instrument makers for several centuries has produced very good results and most instruments are optimal under current or historic musical criteria. Therefore, to reach the level where design suggestion can come out of the physical models, a very high level of refinement must be achieved.

1.2 Some history

The first published studies about the functioning of flute-like instruments probably come from Mersenne [61] and Bernoulli [7] and they consist of analyses of the resonance frequencies of the bore. This approach is still followed today [89] and is very useful for the understanding of several construction properties mainly from the resonator: position, diameter and height of the chimney and toneholes, shape corrections, etc. The next stage in modeling consists of describing the source mechanisms. Helmholtz [46] and Rayleigh [72] were the first to propose such a description. Helmholtz described them as flow sources or a monopole while Rayleigh argued that since the sources act at an open end of the bore they should be described as a dipole. In fact, close to the open end of the resonator there are large velocity fluctuations but the pressure fluctuations are small. Helmholtz rapidly changed his opinion, as he made clear in the comments on the second version of his book. Surprisingly, the same discussion reappeared this century in the sixties, between Elder [28], Coltman

[13] and Fletcher [42]. Like in many of his works, Coltman's pragmatic, careful and clever approach unquestionably resolved the discussion [14].

At the beginning of the sixties, the works by Powell [69] on the edge-tone suggested a feedback loop model. The different components of the model are analyzed as independent blocks that are then connected together. The analysis of the loop gain fixes the phase and magnitude necessary for the loop to oscillate, and predicts the conditions and frequency for a linear model of oscillations. However, the actual amplitude of the oscillation can only be predicted by a non-linear model [39]. His approach has inspired many other descriptions based on loop systems. The linear model is very often solved analytically while a non-linear model requires a numerical approach.

An important period in the development of flute models came with the work of Mc Intyre et al. [59], who were the first to propose a time simulation from a set of simplified equations derived from physical models. Their models were so neat and elegant that many researchers were persuaded that the secrets of the flute functioning had been found and captured in a physical model. Unfortunately, as it turned out, the model was better suited to the violin and clarinet but the flute doesn't even oscillate with the values published [32]. After fine tuning the parameters and adding non-physical elements, like a DC blocking filter and feeding the system with white noise, the model produces sound but is impossible to relate the quantities in the model with physical variables. A more rigorous approach considering fluid mechanics and aero-acoustics has been followed by Howe [48] for the flute and by Crighton [21], Elder [28] and Bechert [4] for the edge-tones. In parallel, a group centered in Eindhoven Netherlands [86, 85, 87, 84, 33, 32] adopted an intermediate path inspired by the work by Powell [69], Fletcher [36], Holger [47], Coltman [13, 16] and Cremer [20]. Their approach lies between the rigorous formulation and the simplified description, producing good quality sound synthesis through models that use lumped elements with a sufficient amount of aero-acoustics.

1.3 Characteristic lengths

Flute-like instruments can be described as a coupling between the hydrodynamic modes of a jet and the acoustic modes of a resonator. Several lengths are useful to characterize it.

The Reynolds number (Re) is used to describe the type of jet. Reynolds observed in flutes vary from some hundreds, in instruments like the recorder [29], up to about 10000 in the transverse flute.

$$500 < Re = \frac{U_j h}{\nu} < 1000 \quad (1.1)$$

Where U_j is the central speed of the jet at the flue exit, h the canal height and ν the kinematic viscosity of the air ($\nu = 1.5 \times 10^{-5} m^2/s$).

The instability of the flow is characterized by the Strouhal number, which corresponds to the non-dimensioned frequency. The definitions of this number vary depending of the situation and the author. Thus, for the experimental measurements $Str = \omega W / U_j$, where ω is the pulsation and W the flue-labium distance (fig.1.1), and sometimes is defined as $Str = fh / U_j$ where $f = \omega / 2\pi$.

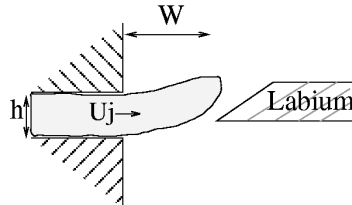


Figure 1.1: Excitation parameters

Theoretical analyses of the jet instability very often use a parameter of semi-length of the jet b , like for instance in the Bickley velocity profile $U_j(y) = U_0 \text{sech}^2(y/b)$ [69, 41]. The relation between the experimental parameter h and the theoretical parameter b is not clear. In a first approximation, it is possible to deduce it through a conservation balance between the jet inside and outside the channel. Assuming a Poiseuille profile inside and a Bickley outside, impulse and central speed conservation

gives $b = 2h/5$ [85]. Flow simulations [75] and the measurements done by Nolle [64], have given better estimations for the jet velocity profile.

In the normal operation of flutes we observe about half hydrodynamic wavelength λ_h between the flue exit and the labium. The propagation velocity of the perturbations on the jet is about 50% of U_j . We found then that for $W = \lambda_h/2$:

$$Str_W = \frac{fW}{U_j} \approx 0.25 \quad (1.2)$$

which shows up as a central value in the operation range [29, 84, 33, 75].

The instability of the jet is related to the presence of two shear layer on both sides of the jet. Therefore it is studied as a function of another version of the Strouhal number based on the lateral dimension of the jet, $Str_h = fh/U_j$ (b is sometimes replaced by h depending on whether it is an experimental or theoretical approach). That is why the ratio W/h that shows up naturally from the division of the two versions of Strouhal, is a determinant parameter in the operation of the instrument. There are flutes using “thick jets” with values of the ratio W/h in the lowest integers (transverse flute, shakuhachi playing loud in the low register, etc); and flutes using “thin jets” with values of W/h going up to 16 (some organ pipes).

$$2 < \frac{W}{h} < 16 \quad (1.3)$$

Fig.1.2 shows the operational range for some flute-like instruments in a space defined by W/h and the Reynolds number.

In the organ, all the pipes are fed by a single blowing mechanism (*soufflerie*). The builder can adjust the pressure going to each pipe by changing the overture of the foot and the geometry of the pipe. Thus he obtains a very large range of operation. Jet models should be adapted to operate in the different areas of the operation range.

Finally, the amplitude of the acoustic oscillation is evaluated by comparing acoustic velocity in the mouth of the instrument with the jet central velocity. The jet central velocity can be found using the Bernoulli equation by measuring the pressure difference along the jet path. The average speed can be estimated by measuring the flow [60]. The acoustic velocity in the mouth of the instrument is often deduced from

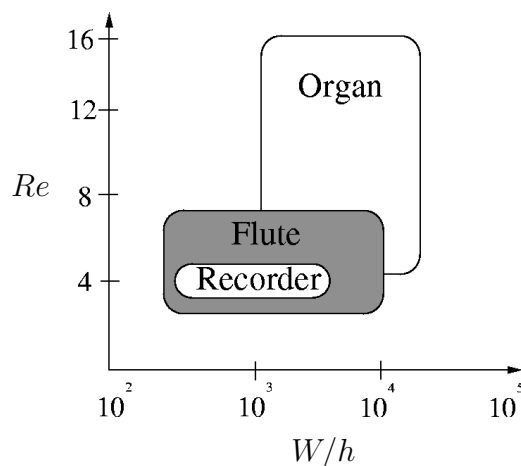


Figure 1.2: Approximate range of operation of the recorder, European transverse flute and organ in a W/h vs. Reynolds space. For the transverse flute, the player can move over the whole range with one instrument while in the organ several pipes are required to cover the range.

measurements of the acoustic pressure inside the resonator, sometimes considering the non-uniformity of the flow in the mouth [85]. In normal playing conditions, it is observed that the amplitude of the acoustic velocity V_{ac} is on the order of one tenth of the jet central velocity:

$$\frac{V_{ac}}{U_j} \approx 10^{-1} \quad (1.4)$$

1.4 Lumped-elements or integral models?

The elements involved in the physical description of flute-like instruments are, in principle, related in ways that are difficult to separate. The acoustic resonance in the tube can't be separated from the radiation at the end of the bore, and it is exactly there where the aero-acoustic sources act. It may then seem artificial to pretend model the system in lumped elements, where one output is connected to the input of the following: jet, aero-acoustic sources and resonator.

1.4.1 Lumped-elements models

Historically the separation in blocks is inherited from the disciplines that study the problems: the flow instability and the jet are traditionally the domain of *fluid mechanics*, the acoustic resonance of tubes with complex forms is domain of *acoustics* and the sound production from a stationary flow is studied in *aero-acoustics*.

Different orders of magnitude both temporal and spatial may justify the separation in independent elements, which corresponds to different approximations from the Navier-Stokes equation.

Jet studies often suppose that the phenomena is developed in a compact region of small dimensions with respect to the acoustic wavelength, where the acoustic propagation is neglected. On the other hand, the resonator description neglects the convection effects. These hypotheses are only valid for low frequencies including the first harmonics of the produced sound. The approximation seems reasonable if we consider that the internal functioning of the instrument is dominated mainly by the fundamental and first two harmonics.

From the point of view of the radiated sound and human perceptive audition the higher harmonics are very important. The radiation is inefficient at low frequencies. Therefore low frequencies remain inside the bore allowing the self-oscillations and assuring a good quality coefficient for the first modes of the resonator. High frequencies are small inside the resonator but they are radiated more efficiently.

The lumped-models approach relies on the hypothesis that the interaction between blocks is localized. The jet is supposed to be perturbed locally at the flue exit, the sound produced by an non-stationary flow is localized at the labium, the resonator is excited at one point, the labium, and the output is measured at the end of the bore.

1.4.2 Integral models

A more rigorous approach is proposed by the integral models such as Howe [48], Crighton [21], Elder [28] and Bechert [4]. These models describe the flow/acoustic field interaction in an integral manner using a mathematic formalism that is valid

only for idealized geometries, and difficult to solve. They often use very restrictive hypotheses such as shear layer infinitely thin or punctual vortices.

Lumped-models is the approach followed throughout this thesis. Despite their difficulties, integral models are probably the best alternative to follow after reaching the limits of the lumped formulation [32, 31].

1.5 What to model?

The sound produced by an instrument is the result of the work done by the instrument's builder and the player. Beyond flutes, in many instrument families, the builder works mainly in the resonant part of the instrument (violin's body, position of pistons, shape of the brasses etc.), while the player focuses on the control over the non-linear excitation, which could be long (sustained excitation, like violin bow or woodwind blow) or short (non-sustained excitation such as percussion, plucked guitar, etc).

In flute-like instruments the builder can also influence the excitation. The more he influences the excitation the more the sound is determined by the instrument. The instrument would produce sound without the need of an instrumental technique and the player could concentrate on organizing the musical discourse. These instruments would have the same sound regardless of the player. Modeling only the instrument would be enough to obtain convincing sounds. This is the case of organ pipes.

On the other hand, some flute-like instruments assign a predominant role in the sound production to the player. These instruments require learning a technique before producing a sound and the final sound will be very different from player to player, as is the case of lip-played flutes. Therefore, a correct model of these instruments must include a description of the techniques used by the player.

1.6 Thesis layout

The thesis is made up of four chapters which are written as independent papers and are intended to be self-contained. Therefore some redundancies can be expected when reading it as a whole.

Chapter 2 describes experimental measurements on jets excited with a controlled excitation consisting of two loudspeakers in opposite phase. A Schlieren system is used to visualize the jet and image detection algorithms are developed to extract quantitative information from the images. In order to study the behavior of jets observed in different flute-like instruments, several geometries of the excitation and jet shapes are studied. The data obtained is used to propose analytical models that correctly fit the observed measurements and can be used for simulations. Part of this chapter has been published as conference papers in [23, 22].

The control exerted by the performer on the instrument is of crucial importance in the quality of the sound produced for a number of flute-like instruments. In chapter 3 the transverse flute is experimentally studied. An ensemble of control parameters are measured and visualized in order to describe some aspects of the subtle control attained by an experienced flautist. Contrasting data from a novice flautist are compared. As a result, typical values for several non-dimensional parameters that characterize the normal operation of the instrument have been measured, and data to feed simulations has been collected. This chapter has been submitted to JASA [66] and has been partially published as a conference paper in [67].

In chapter 4 the information obtained through experimentation is combined with research developed over the last decades to put together a time-domain simulation. The model proposed is one-dimensional and driven by a single physical input. All the variables in the model are expressed in terms of pressure which allows for implementation and control in real-time. The model provides both a testbed to compare and validate measurements as well as a highly configurable and real-time musical instrument.

Finally, in chapter 5 an application of the real time simulation is presented. A multi-disciplinary study carried out at the IRCAM is described. A virtual flute based on physical modeling and controlled by the flutists through a dedicated midi control interface was developed and used to assist an ethnomusicology study on the Ouldémé flautists from north Cameroon. This chapter has been partially published as conference papers in [26, 11].

Chapter 2

Jet analysis of flute-like instruments by means of image processing

Abstract

Presently most models for jet oscillations are based on linear jet instability analysis described by Rayleigh. These models show two weak points in the application to flute modeling: the initial perturbations induced by transverse acoustic velocity is not clearly described, and the jet transverse oscillation in some flutes may reach amplitudes that exceed the boundaries of a linear model. In this chapter we present results of an experimental study of the receptivity problem. The method utilized consists of visualizations of jet motion under transverse acoustic perturbation generated by loudspeakers. Hot-wire is also used to measure velocity profiles. It is impossible to observe the jet/acoustic-velocity interaction directly, therefore we have chosen experiments that permit an indirect description of the problem through its consequences. The experiments examine variations of the flue exit geometry and changes in the amplitude of the acoustic excitation. Oscillations of the jet are visualized using the Schlieren technique. Images are analyzed with specially developed image-processing algorithms.

2.1 Introduction

2.1.1 Basic operation

Instruments from the flute family share a similar principle of operation. An unstable jet comes out from either a formation channel or the lips of a player and travels towards a sharp edge commonly refer to as the labium (fig.2.1). On its way, the jet crosses the acoustic field produced by the the flute pipe or resonator which perturbs its trajectory. Air jets are intrinsically unstable, therefore this perturbation travels and gets amplified spontaneously along the jet. The interaction of the perturbed flow with the labium provides the necessary acoustic energy to sustain the acoustic oscillation in the pipe, closing a feedback loop.

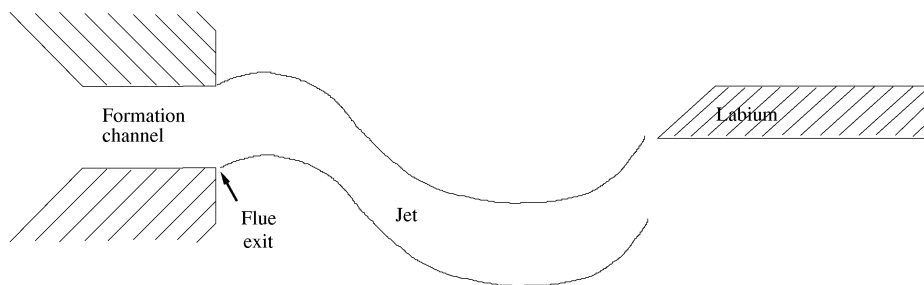


Figure 2.1: Jet emerging from the formation channel, oscillating and traveling towards the labium

2.1.2 Flutes geometry

Flute-like instruments present an immense variety of geometries and playing techniques. In particular they show important differences in the shape at the channel exit. Organ pipes may have a flue channel terminated by a 90 degree angle. Recorders show a 45 degree cut at the flue exit and recorder makers insist on not rounding the edges at the flue exit, claiming that this would destroy the sound of the instrument. This may seem contradictory since lip-played instruments (like flutes, shakuhachis, quenás, etc) obviously show a rounded flue exit.

An enormous amount of research has been devoted to the study of flutes with fixed geometry like recorders and organ pipes, mainly because of simplicity and repeatability in experimentation. Although some important results of such research can be generalized to other flutes, new models are required to understand the complexity and variety of sounds produced by flutes.

2.1.3 Lumped vs Integral models

The current research body can be classified, in its most fundamental structure, in two groups. Models that seek an integral description of the problem and those that split the problem into lumped elements that can be analyzed independently and then connected back together to reconstruct the original problem. A detailed review of such lumped models can be found in [32] and is the approach assumed throughout this chapter. Lumped models sacrifice rigor in the interaction between elements to provide a simple and tractable approximation to the problem. Integral models are more rigorous and are expected to produce more realistic results but for the moment their mathematical complexity makes them valid only for idealized geometries and not suitable for real-time implementations.

2.1.4 Limitation of current models and Motivation

The jet behavior under transverse acoustic excitation appears to be the most difficult part of the models at the moment. Most authors use a jet instability model inspired by the work of Rayleigh [72] followed by Sato [73], Fletcher [42], Mattingly & Criminale [57]. This model is based on a linear perturbation of the stream function that describes the jet.

None of the current models explain the initial perturbation of the jet induced by the acoustic field. Verge [84] was the only one to propose an analytical model for the initial perturbation of the jet that allows the transverse displacement to be zero at the flue exit. Verge himself observed that the jet displacement predicted by his theory was worse than the traditional semi-empirical model.

There are some additional inconveniences when applying the models to flute-like instruments. They are based on a linear perturbation theory and are therefore restricted to small transverse jet oscillations. While flow visualizations in different geometries of flutes [33] show transverse oscillations of the jet with amplitude greater than the flue channel height, they are only valid for short distances, typically smaller than the hydrodynamic wavelength on the jet since further downstream the flow shows a tendency to roll up into discrete vortices. And finally, since the viscosity is normally neglected, the models assume a constant jet velocity profile downstream from the flue exit. This is only valid for low Reynolds numbers (while most of the instruments from the flute family operate at Reynolds numbers above 1000) and for smooth initial velocity profiles.

2.1.5 Chapter layout

Throughout this chapter, flow visualizations of oscillating jets under sinusoidal acoustic excitation are done using Schlieren method [62] and jet velocity profiles are measured through hot-wire techniques. In section 2.2 the *jet instability* is measured, observing the influence of formation channel and the geometry of the flue exit in the propagation of the perturbation. Section 2.3 explores the *receptivity problem*, measuring the phase response of the jet to a perturbation at the flue exit and the boundaries of validity for a linear model.

2.2 Jet instability

2.2.1 Jet Operation

Air jets are intrinsically unstable. A perturbation applied at the origin is convected downstream while being amplified [72]. The interaction between jet and acoustic field is assumed to be localized and occurs at the flue exit. That is the place where the jet exits the confined channel to travel freely out towards the labium (fig.2.1). The shear layers of the jet are modulated by the acoustic field causing the jet oscillations to lock on the frequency of the acoustic excitation. Thus, a laminar jet submitted to a

periodic excitation, oscillates at the same frequency of the excitation and amplifies the perturbation until it reaches a lateral displacement that prevents its structure from being cohesive, eventually causing the jet to break into vortices that later become turbulences (fig.2.2).

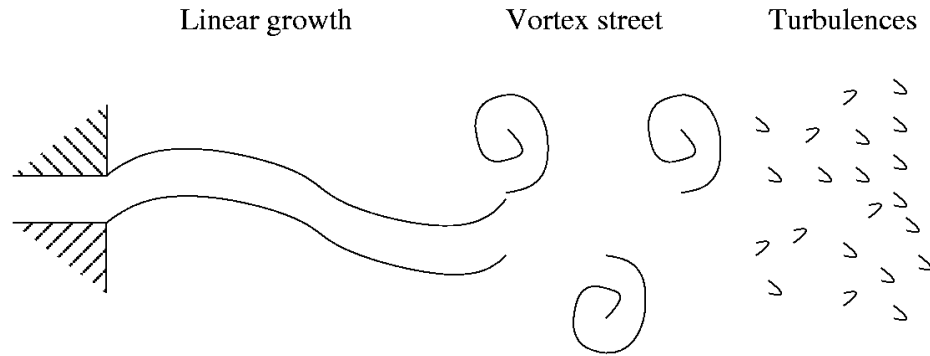


Figure 2.2: Simplified segregation of the jet into linear growth, vortex street and later turbulences

Jet-resonator interaction

In flute-like instruments, the perturbed jet transfers energy inside the resonator by interacting with the labium close to an open end of the resonator. On the other hand, the resonator perturbs the jet mainly with a combination of two contributions: the acoustic waves traveling inside the resonator and the hydrodynamic feedback coming from the interaction between the jet and the labium. The latter has been widely studied in an edge-tone configuration (ex.[69, 76]), which consists on an oscillating jet hitting a sharp edge without the presence of a resonator.

The *jet receptivity* refers to the way in which the jet reacts to the acoustic excitation and the *jet instability* refers to the way the perturbation evolves as it travels away from the origin.

Jet development

Most instability models (e.g. [84, 42]) are developed under the assumption of a linear perturbation of potential flow where vorticity is conserved. None of them provide a

complete description of the jet development. The most accepted approach found in the literature consists of splitting the jet in two segments. One segment is linear, from the jet origin until where it breaks into vortices, and is well described by Rayleigh's theory [72]. The other is nonlinear and similar to a Von Karman vortex street that is described by Holger's model [47].

2.2.2 Jet velocity profile

As will be discussed in section 2.2.3, according to Rayleigh's approach the instability is expected to depend on the jet velocity profile. The velocity profile at the flue exit depends primarily on the history of the flow in the channel before separation occurs. While traveling inside a confined channel with constant section, viscosity slows down particles close to the walls making the boundary layers thicker, injecting vorticity and smoothing out the velocity profile. Thus we observe smoother profiles coming out from a long channel and sharper profiles coming out of shorter channels (fig.2.3). While Ségoufin [77] provides a good understanding on the effect of the formation channel length, none of the available models are good enough to take into account the effect of the channel geometry (length and flue exit shape) on the jet response.

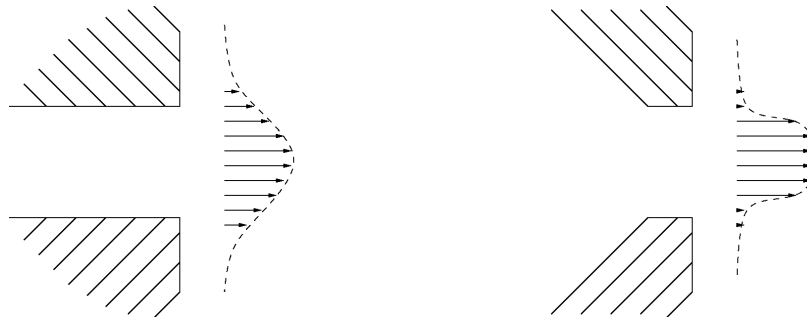


Figure 2.3: Jet coming out from a long channel (left) is smoother than one coming from a short channel (right)

Studies on the edge-tone frequency as well as shifts in the oscillation thresholds [76] predict a higher convection velocity on jets issuing from short channels, but no direct measurements have been done yet.

The velocity profile also evolves as the jet moves away from the flue exit. Air particles outside the jet interact and some of them become part of the jet smoothing the profile as it travels away from the flue exit (fig.2.4

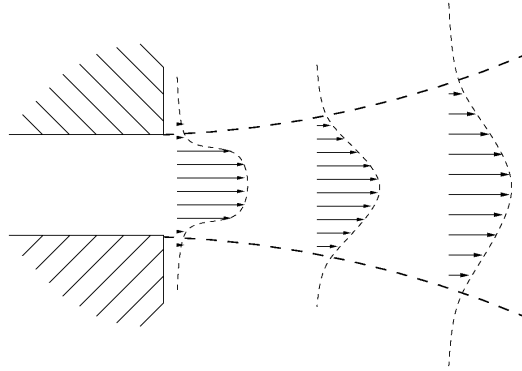


Figure 2.4: Changes in the jet profile as it travels away from the flue exit

Analytical descriptions

Smooth velocity profiles are often approximated by a Bickley profile:

$$U(Y) = U_j \operatorname{sech}^2\left(\frac{y}{b}\right) \quad (2.1)$$

where b is a parameter that can be related to the jet height [84]. For profiles with thinner boundary layers Nolle [64] proposes a family of self-similar profiles of the form:

$$U(Y) = U_j \operatorname{sech}^2\left(\left(\frac{y}{b}\right)^n\right) \quad (2.2)$$

Where n is a parameters makes the jet profile more squared as it grows.

Central velocity

The central speed of the jet U_j at the channel exit can be estimated assuming atmospheric pressure outside the channel and using Bernoulli's equation:

$$U_j = \sqrt{\frac{2p_f}{\rho_1}} \quad (2.3)$$

Where p_f is the pressure in the cavity before the channel, and ρ_1 the gas density.

The velocity profile is difficult to estimate. Only recently, the technical development of direct flow simulations and hot-wire anemometry allowed an estimation for different channel configurations [75, 64]. For this reason, early studies on the subject assumed either a Bickley profile or top-hat profile.

2.2.3 Linear theory

As pointed out in section 2.2, jets are intrinsically unstable and therefore a perturbation propagating downstream naturally amplifies. A finite modulation of the vorticity in the shear layers can be assumed at the jet origin. The modulation is applied to both shear layers in counter phase. That is, when modulation is maximum in one shear layer it is minimum in the other one, and vice versa, triggering sinuous modes on the jet. The perturbation will grow exponentially as it travels away from the flue exit, up to the point where the flow rolls up and finally breaks into vortices and later turbulence as shown in fig.2.2.

Theoretical approach

Under a potential flow assumption, Rayleigh proposes an equation for the conservation of vorticity for a two-dimensional flow:

$$\left(U(y) - \frac{\omega}{\alpha(\omega)} \right) \left(\frac{\partial^2 \phi}{\partial y^2} - \alpha^2(\omega) \phi \right) - \frac{\partial^2 U(y)}{dy^2} \phi = 0 \quad (2.4)$$

Where $U(y)$ jet velocity profile is assumed to be a function of the vertical coordinate y only and ω is the temporal pulsation. It admits wave-like solutions of the form:

$$\phi = \varphi(y) e^{i(\omega t - \alpha x)} \quad (2.5)$$

Where φ is the complex amplitude of the stream function ϕ , ω the angular pulsation, t time and α the wave number. Relation 2.4 provides a link between the jet velocity profile U_j and the complex wave number α , which can be solved analytically for simple velocity profiles, like top-hat [84] or Bickley [57].

Spatial and temporal analysis

Theoretically either ω or α could be complex, thus there are two possible analyses of ϕ : a spatial analysis which consists of assuming ω is real while looking for a complex wave number $\alpha = \alpha_r + i\alpha_i$, and a temporal analysis which looks for a complex ω while assuming α real. The spatial analysis has shown a better fit to measurements [64] and is more adequate to the study of flutes since the jet is excited at a frequency governed by the acoustic resonances of the pipe and the analysis of steady state oscillations is not compatible with complex ω . Thus, the convection velocity corresponds to $c_p = \omega/\alpha_r$ and the spatial amplification growth is given by the coefficient α_i .

The convection velocity has been observed to be about half of the jet central speed U_j [72], but its actual value depends on the jet velocity profile and may depend on frequency.

Transverse displacement

In order to calculate the transverse displacement $\eta(x)$ of the jet at a distance x from the flue exit, one has to integrate the transverse velocity over the particle path, from the flue exit to the actual position.

$$\eta(x, t) = \int_{t-\frac{x}{\bar{v}_0}}^t V_t(t) dt \quad (2.6)$$

Where the transverse velocity component V_t is the sum of the acoustic velocity and the transverse velocity of the instability wave ($V_t = V_{ac} + v_y$), which can be calculated by differentiation of the stream function ($\partial\phi/\partial x$) [70].

Fletcher [42] proposes a semi-empirical model for the jet displacement. A harmonic acoustic field $v = V_{ac}e^{j\omega t}$ causes the initial acoustic displacement of the jet that propagates with a phase velocity c_p and grows with a rate α_i . In order to fulfill the condition of a zero transverse motion at the flue exit, Fletcher's model adds an 'ad-hoc' correction. The resulting transverse jet displacement is then given by:

$$\eta(x, \omega) = -j\left(\frac{v}{\omega}\right) \left(e^{j\omega t} - \cosh(\alpha_i x) e^{j\omega(t-\frac{x}{c_p})} \right) \quad (2.7)$$

Where the $e^{\alpha_i x}$ has been replaced by $\cosh(\alpha_i x)$ in order to fulfill the condition $\partial\eta/\partial t = 0$ at $x = 0$.

Verge [84] pointed out the lack of physical background in Fletcher's approach since fluids, by definition don't oppose to displacements or deformations but only to rates of deformation, and tried a different approach by matching vorticities at the flue exit. His model, although physically more consistent, didn't fit measurements as well as Fletcher's.

In order to simplify the model and isolate the amplification from the convection he proposed a modification of it:

$$\eta(x, \omega) = -j\left(\frac{v}{\omega}\right) \left([e^{j\omega t} - \cosh(\alpha_i x)] e^{j\omega(t - \frac{x}{c_p})} \right) \quad (2.8)$$

There is an evident misbehavior of this model at low frequencies due the factor $1/\omega$ and a phase difference of $\pi/2$ between the perturbation V_{ac} and the oscillation at $x = 0$.

We propose an empirical model that fits better our data. Through our analyses we observe that the jet oscillation can be described, at the beginning of the oscillation, by :

$$\eta(x, \omega) = \eta_0 e^{\alpha_i x} e^{j\omega(t - x/c_p)} \quad (2.9)$$

with an exponential growth of the oscillating amplitude $\hat{\eta}(x) = \eta_0 e^{\alpha_i x}$. A comparison between the three models is shown in fig.2.5.

The problem of determining the amplitude of the excitation at the flue exit η_0 , or the response of the jet to the acoustic perturbation, hasn't yet found an adequate description [32]. Nolle [64], using hot wire technology, studied the instability problem experimentally for a specific geometry. He validates his measurements using Mattingly's [57] solution to Rayleigh's equation (eq.2.4). Ségoufin [76, 77] studied the effects of the formation channel by numerical integration of Rayleigh's equation.

Throughout this chapter results on experimental measurements are presented for a broader scenario that includes different channel lengths and flue exit geometries inspired by the variety found in real instruments of the flute family. Departing from

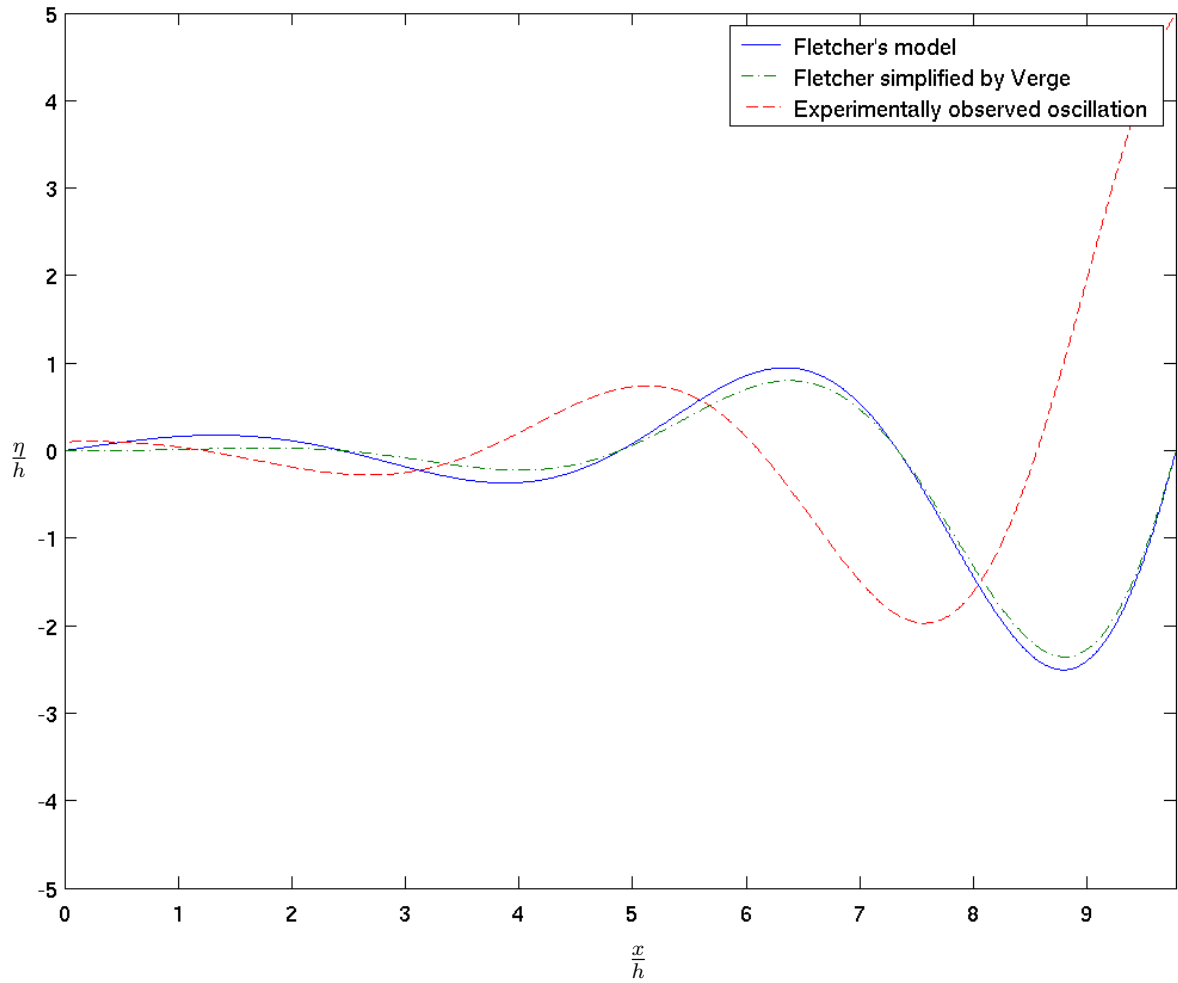


Figure 2.5: Comparison between the three jet displacement models: Fletcher's model (solid line), Fletcher's model simplified by Verge (dashdot line) and experimentally observed oscillations (dashed line)

the methods used in previous studies, our measurements are done entirely with non-intrusive visualization techniques. Digital image processing algorithms have been developed to analyze the data. To provide a theoretical reference, we measure the jet profile of the different configurations using hot-wire technology. Then, Rayleigh's equation is numerically integrated to calculate the wave number α and contrasted with measurements.

2.2.4 Experimental setup

The analytical models proposed are in two dimensions. To approximate that condition with a real jet, the width of the jet is set much bigger than its height (1mm height, 20mm width) which also produces a jet that resembles those from recorders and organ pipes.

Air jet velocity

A jet issuing from a flue exit is submitted to a sinusoidal acoustic excitation generated by loudspeakers, as shown in fig.2.6. The jet velocity is controlled with a manual valve measuring the pressure p_f in the cavity just before the formation channel. A Reynolds number of 200 was chosen (Reynolds = $U_j h / \nu$, where $h = 1\text{mm}$ is the jet height, ν : the air kinematic viscosity) giving a jet velocity = 3 m/s which assures laminar behavior.

Acoustic excitation

Acoustic velocity is created with two loudspeakers in opposed phase. The choice of two loudspeakers as opposed to one provides a more homogeneous acoustic field together with a minimum acoustic pressure at the position of the flue exit (half way between the loudspeakers). The uniformity of the acoustic field in the region of interest was further checked using a velocity sensor.

Both the frequency and amplitude of the acoustic excitation can be accurately controlled. Changes in frequency affect the Strouhal number (Strouhal = fh/U_j ,

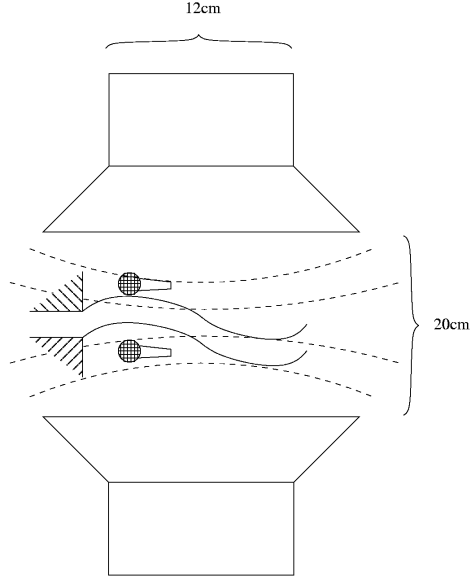


Figure 2.6: Air jet submitted to an acoustic excitation generated by loudspeakers. Acoustic velocity measured through the pressure gradient measured with two microphones (not in scale)

with U_j the central jet speed at the exit deduced using eq.2.3) while the amplitude affects the acoustic velocity magnitude, responsible for the excitation of the jet.

The phase and amplitude of the acoustic excitation are measured using two calibrated microphones aligned along the propagation direction of the acoustic waves at a distance $\Delta y = 17.2\text{mm}$ (fig.2.6). Pressure gradient in the direction y transverse to the jet direction, was measured and converted into acoustic velocity through Euler's relation:

$$-\rho_0 \frac{dv}{dt} = \frac{\partial P}{\partial y} \quad (2.10)$$

assuming sinusoidal acoustic excitation $v = V_{ac} e^{-j\omega t}$,

$$V_{ac} = \frac{1}{j\omega\rho_0} \frac{\Delta P}{\Delta y} \quad (2.11)$$

Jet fluid

The fluid used for the jet is CO_2 which has a mass density higher than air (CO_2 : $\rho_1 = 1.98\text{kg}/\text{m}^3$, air : $\rho_0 = 1.2\text{kg}/\text{m}^3$). This choice is a compromise between having

enough difference to allow good optical results and being close enough to emulate the behavior found in flute-like instruments. Fig.2.7 shows velocity profiles of both gases at different central velocities U_j . We observe small differences between them supporting the validity of our measurements.

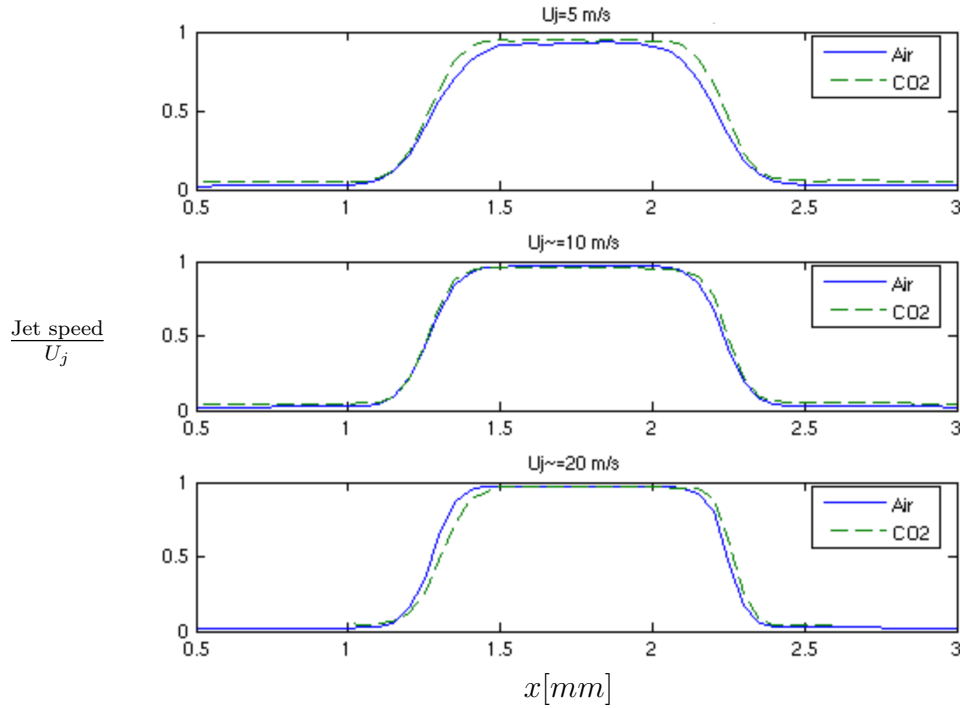


Figure 2.7: Comparison between CO2 and air, for $U_j = 5, 10$ and 20 m/s.

Visualization method

The CO2 jet remains invisible to our naked eyes, but changes in the fluid density cause variations in the refractive index that can be visualized using the Schlieren technique [62]. With the knife edge placed horizontal (y direction), vertical mass density gradient is converted into intensity at the camera, making the jet visible (fig.2.8).

Sequential images are taken with a digital camera [PCO,Sensicam, fast shutter] with exposure time of the electronic shutter set to one microsecond. Synchronized strobe light is used to provide the necessary contrast. Signals triggering the flash, the

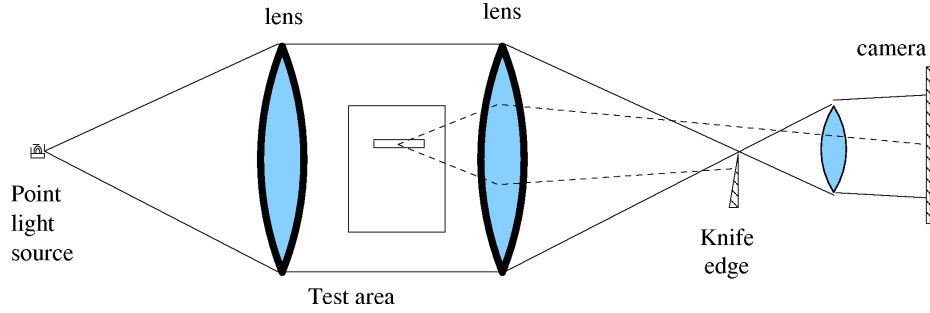


Figure 2.8: Schlieren system.

camera capture and the acoustic excitation come from different channels of the same wave generator, assuring good synchronization for the stroboscopic effect.

The frequency of images capture f_c is set such that multiples of it are slightly different from the excitation frequency f_e , providing an aliased representation of the oscillation. The number of images per cycle of oscillation \hat{I} can be adjust by controlling these two frequencies through the following relation:

$$\frac{\hat{I}}{f_c} = \frac{1}{f_e \bmod f_c} \quad (2.12)$$

Certainly successive images come from different periods of the excitation signal, but they can be collapsed in the same cycle since the oscillation is stationary.

The frequency of the camera f_c was set to 12 frames per second, while the acoustic excitation frequency f_e ranged from 24.28 to 516.28 Hz, providing $\hat{I} = 50$ images per cycle and a Strouhal span of 0.045 to 1.1. Images are captured in raw bitmap files, with size 1280 x 448, and 8 intensity bits (fig.2.9).

Images obtained with Schlieren method are extremely sensitive to variations in the setup. Small differences in the parameters produce enormous image variations (see appendix A). Therefore images obtained from different trials are very often different, requiring robust image analysis methods to analyze them.

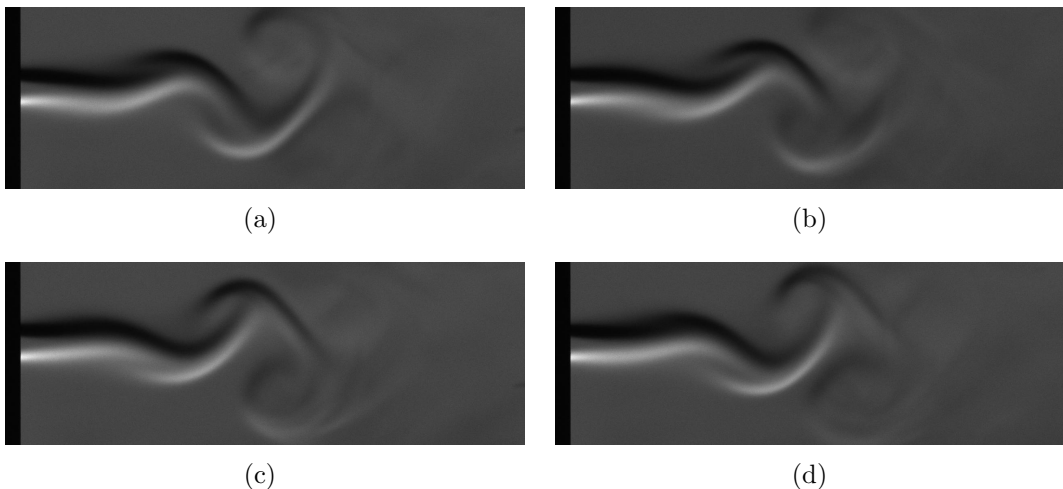


Figure 2.9: Images obtained via Schlieren technique. Reynolds: 200, Jet speed: 3 m/s, Excitation freq.: 108.28 Hz, Strouhal: 0.225. $V_{ac}/U_j = 0.005$. One cycle of oscillation, the acoustic velocity phase is 0 (a), $\pi/2$ (b), π (c), $3\pi/2$ (d). The two shear layers appear with opposite light refractive gradient, so that the upper shear layer gets darker while the lower shear layer gets lighter than the average gray level.

2.2.5 Image data analysis

Three algorithms have been developed to automatically determine the transverse displacement of the jet for every image. Their details, strengths and weaknesses are explained in appendix B. The algorithm based on cross-correlation between images at different times is chosen for the analysis in this chapter.

An example of the jet position obtained with this method is shown in fig.2.10, where two cycles of oscillation are displayed in a 3D mesh.

All columns of the image oscillate in time at the frequency of the excitation. Therefore, for each column we fit a sinusoid at that frequency:

$$Y(f) = \frac{1}{N} \sum_{i=0}^{N-1} X_i e^{\frac{-j2\pi f}{f_s}} \quad (2.13)$$

where, N is the number of pixels per column. Fig 2.11 shows an example of the position detection super-imposed to one image together 2.11(a) with the amplitudes

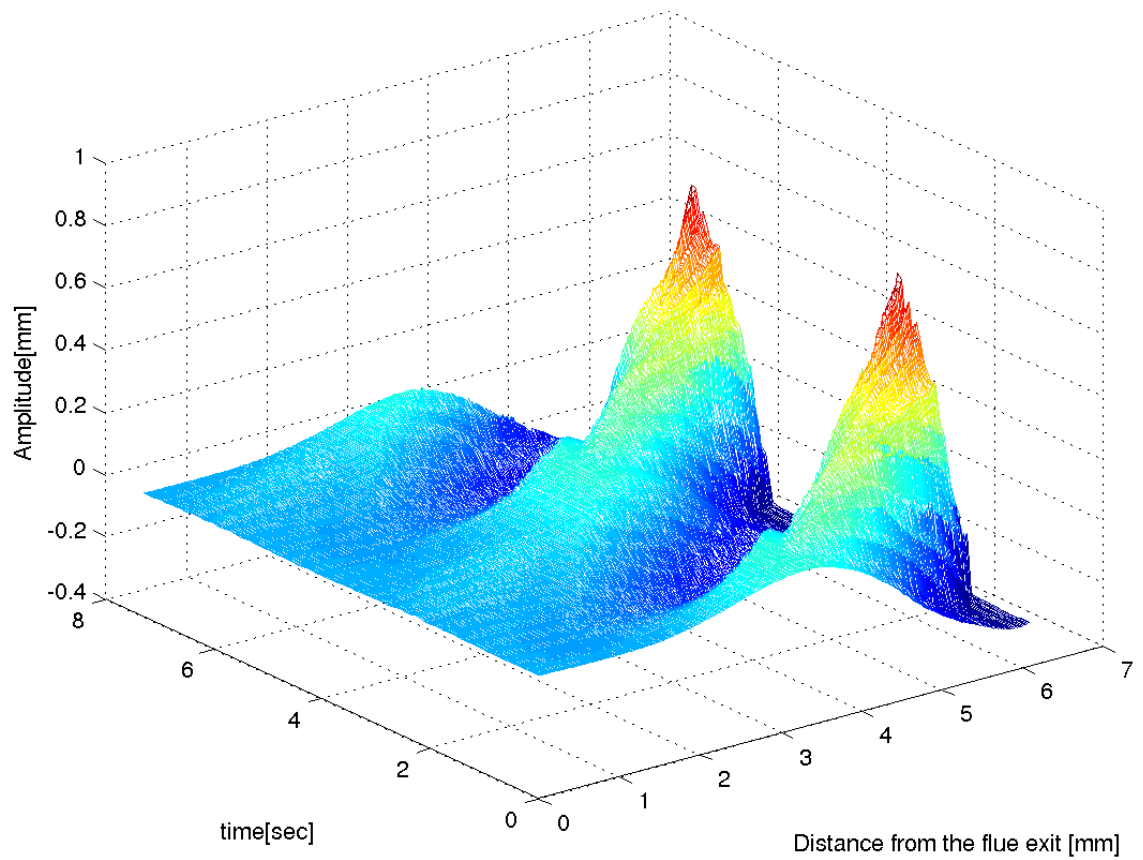


Figure 2.10: Position of jet detected by cross-correlation method. Time axis corresponds to frame times in seconds.

$|Y(f)|$ and phases $\angle Y(f)$ calculated for the complete sequence 2.11(b). Both detections begin at the end of the black region to the left of the image, which corresponds to the lateral view of the flue exit wall.

The linear model predicts an exponential growth α_i for the perturbation and constant convection velocity c_p . They can be obtained by fitting an exponential to the amplitude along the horizontal axis, $\eta_0 e^{\alpha_i x}$ (fig.2.11(b) top, thin curve), and by fitting a line to the phase, and finding its slope $c_p = \frac{d\angle Y(x)}{dx}$ (fig.2.11(b) bottom, thin curve).

The phase behaves linearly on the range of interest but typically shows a small curvature close to the origin. This is a singularity, where the jet is being formed and the interaction with the acoustic field occurs. Therefore two curves have been fit to the phase, a linear fit to be used with the linear model and a fourth order polynomial fit which gives a good approximation to the phase at the origin. The phase reference is arbitrary but common to the jet vertical oscillation and the acoustic excitation.

2.2.6 Influence of the channel length

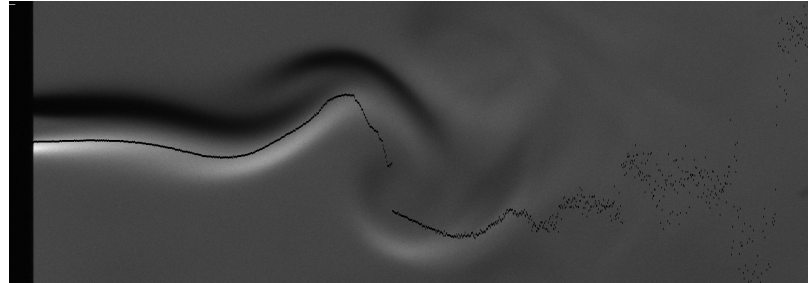
Formation channels of two different lengths have been studied. A long channel of 10 mm and one short of 1 mm (fig.2.12).

Measuring the velocity profile

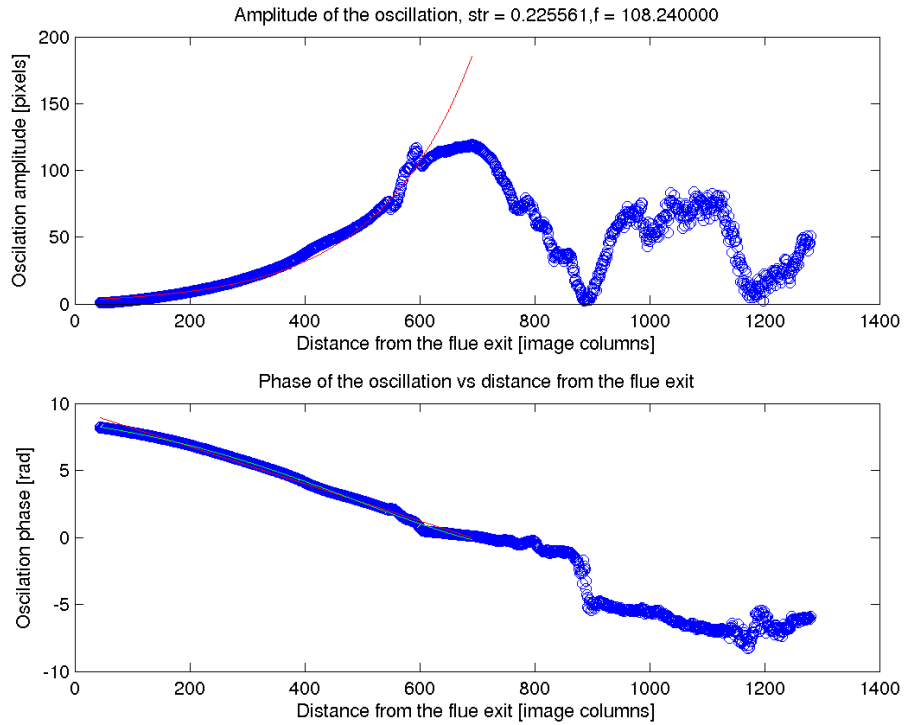
Hot-wire anemometry is used to measure the velocity profile for three central jet velocities U_j of 5, 10 and 20 m/s. The sensor has been placed at a distance of 1 mm away from the flue exit. Nolle profiles (eq.2.2) are fit to both curves. Fig.2.13 show the measured data as well as the curve fits.

The thickness parameter b from eq.2.2 seems to remain close to $0.5h$, ranging from $0.45h$ to $0.5h$. The exponent n remains equals to 4 for the short channel and moves from 2 to 4 for the long channel as U_j moves from 5 to 20 m/s.

For jets with slow central velocity (5 m/s, fig.2.13 top), we observe that the long channel has smoother profile than the short. But for faster central velocity (20 m/s,



(a)



(b)

Figure 2.11: a): Schlieren image with the detection of position using the cross-correlation method. $Reynolds = 200$ and $Strouhal = 0.225$. Excitation frequency = 108 Hz, $V_{ac}/U_j = 0.005\%$. b) Top: (thick) Amplitude of the detected sinusoids, (thin) exponential fit. Bottom: (thick) Phase of detected sinusoids, (thin) linear fit.

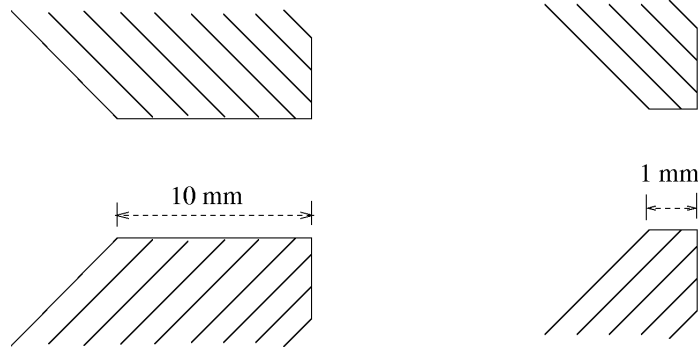


Figure 2.12: Long and short formation channels.

fig.2.13 bottom) both profiles look alike. The long channel enlarges the shear layers because of the fluid viscosity. Its incidence on the jet is smaller as the jet gets faster.

Thus we expect our results from this analysis to depend on U_j . In the case of the short channel, the smoothness of the profile comes mostly from the effect of viscosity on the 1-mm path traveled by the jet from the flue exit to the place where the measurements are done.

Analysis from images

The estimated convection velocity c_p is represented as the non-dimensional variable c_p/U_j and is shown in fig.2.14(a) as function of the Strouhal number ($Str = fh/U_j$). It is about 0.5 for the short channel and 0.3 for the long one, which confirms the observations done by Ségoufin [76] studying the frequency of the oscillations in edge tones. This can be interpreted, as suggested by Ségoufin, in terms of the boundary layers' thickness of the jet, which becomes thinner in the case of short channel. Both curves are almost constant, thus the factor $e^{i\omega x/c_p}$ from eq.2.9 could be approximated by a simple delay in the range of Strouhal studied.

The amplification growth α_i is represented as the non-dimensional variable $\alpha_i h$ and is presented in fig.2.14(b) as function of Str . When Str is set to values higher than those presented in fig.2.14(b), α_i decreases and eventually the jet becomes stable around $Str = 2$. The shape of both curves is concave which coincides with the theoretical analysis [57] and implies more amplification in certain frequency ranges.

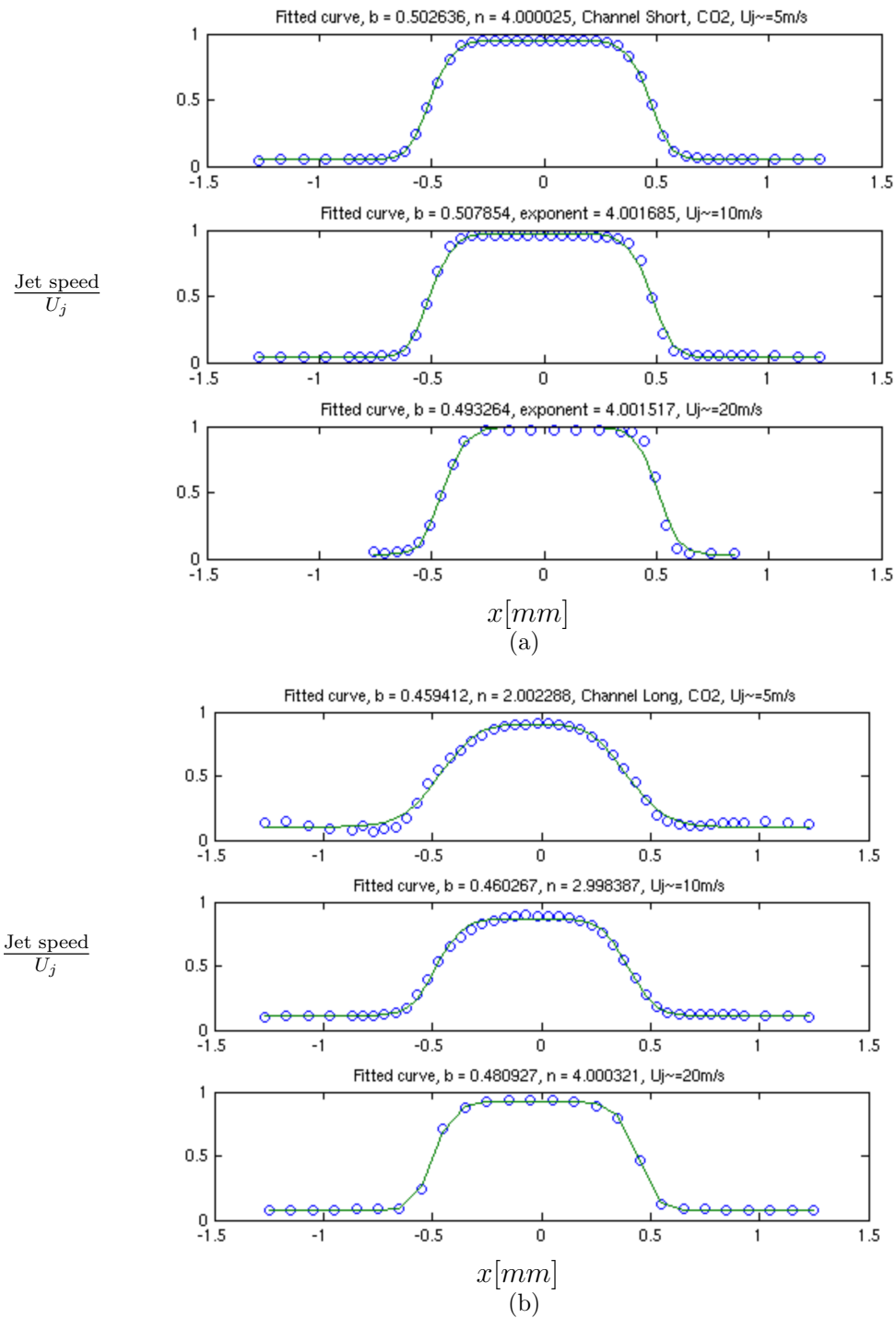


Figure 2.13: CO₂ jet profile. a) short channel, b) long channel. Jet speed= 5, 10, 20 m/s from top down. Nolle profiles (eq.2.2) are fit to the curves finding b and n for each curve

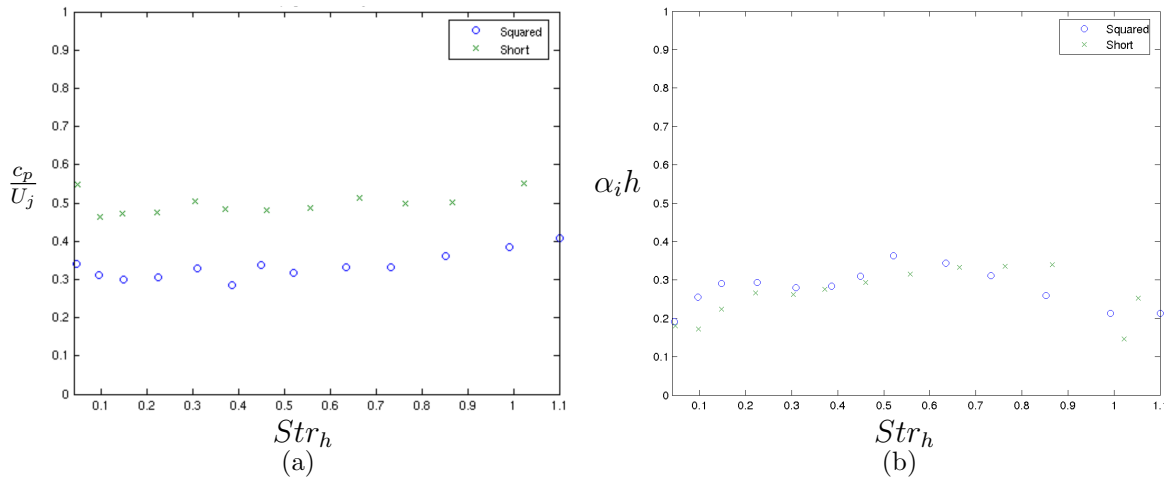


Figure 2.14: a) Dimensionless convection velocity and b) amplification coefficient, flue exit short (o), squared or long(x)

Differences between the two cases are not significant. The amplification growth seems not to depend on the channel length.

Rayleigh's numerical analysis

Using the analytical expression for the profiles and Rayleigh's conservation of rotational (eq.2.4) the theoretical value for both c_p and α_i are calculated using numerical integration and are displayed in fig.2.15 as functions of the Strouhal number.

Comparison between theoretical and experimental results

Rayleigh's equation assumes inviscid, incompressible fluid. Moreover, the jet velocity profile is assumed to be the only function of the vertical coordinate which implies that it keeps its shape throughout the whole trajectory. Consequently, we can expect some differences in the experimental results. The comparison will show these tendencies along with qualitative differences.

In the range of Str_h (0.1-1.1) the convection velocity increases when the jet gets sharper, as was already observed in the experiments. From the numerical analysis,

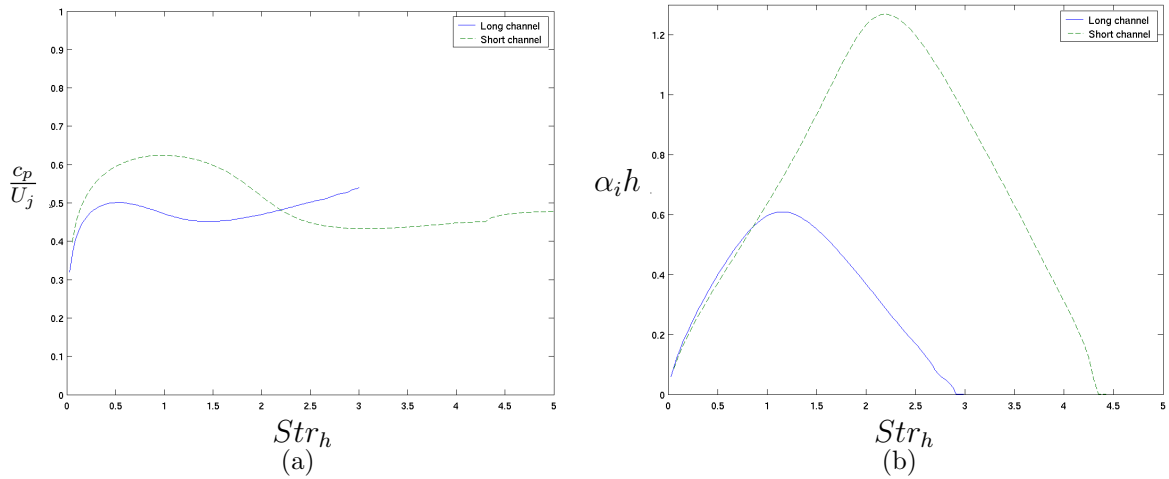


Figure 2.15: a) Dimensionless convection velocity and b) amplification coefficient for a long channel (solid line) and short channel (dashed line) calculated using Rayleigh's equation

C_p/U_j ranges from 0.45 to 0.65, as opposed to the experiments where it varied from 0.3 to 0.5. The disparity can be attributed to simplifications described above.

The amplification growth α_i shows very small differences between short and long channel, also observed in the experiment. However, an ascending shape which peaks at a Str_h greater than the measured one.

2.2.7 Influence of the channel exit geometry

To study the effects of the flue exit geometry, three channels with different flue exits are studied. We refer to them as squared, rounded and 45 degrees, as shown in fig.2.16. These all have a similar channel length of 10 mm. The channels are chosen to cover a variety of geometries commonly observed in real flute-like instruments, as was described in section 2.1.2.

Analysis from images

The measured convection velocity c_p is represented as the non-dimensional variable c_p/U_j and is shown in fig.2.17(a) as function of Str . There is no significant difference

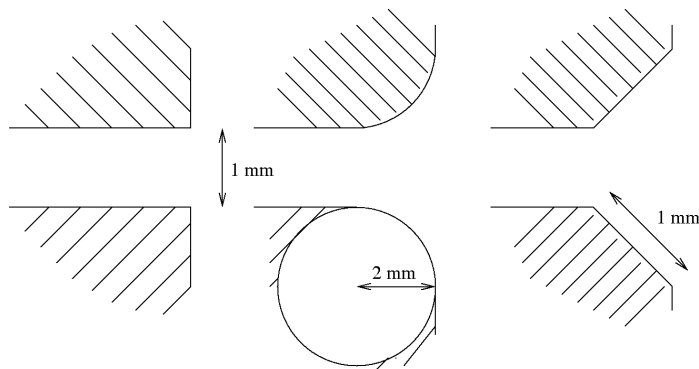


Figure 2.16: Geometry of the three flue exits used, from left to right: Squared, Rounded, 45 degrees.

among the three cases studied, all of them are approximately 0.3. The convection velocity seems to be independent of the flue exit which confirms that it depends mostly on shear layer formation in the channel.

The amplification growth α_i is represented as the non-dimensional variable $\alpha_i h$ and is presented in fig.2.17(b) as function of Str , for the three cases studied. Although there is some dispersion in the data, concave shapes are observed again, but this time both the curvature ratio and the maximum frequency vary with the different geometries. Peaks, or preferred frequencies lie between Str 0.4 and 0.6. The magnitudes of the amplification coefficient for the three exits are in agreement both with the experimental measurements by Nolle [64] and theoretical values by Mattingly and Criminale [57].

2.2.8 Discussion

The flue exit geometry is judged by instrument builders as critical to the sound quality. Its effect seems not to be related to the instability of the jet but rather with the complex interaction between the jet shear layers and the acoustic field at the flue exit. A detailed analysis of the velocity field in the vicinity of the flue exit should be carried out in order to interpret these results further.

The convection velocity of the perturbation c_p as well as the amplification coefficient α_i seem to depend mainly on the velocity profile.

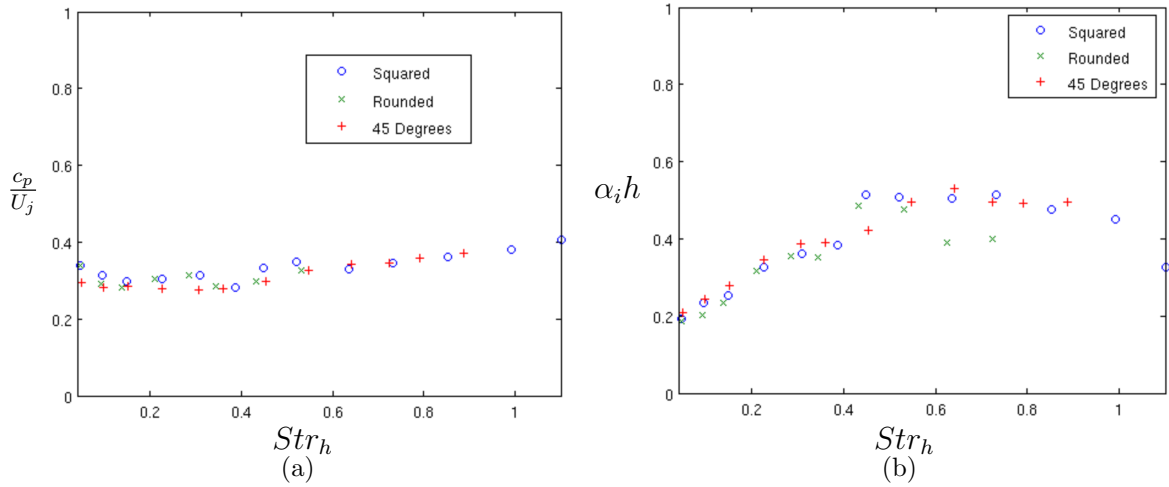


Figure 2.17: a) Dimensionless convection velocity and b) amplification coefficient, flue exit squared (o), rounded (x) and 45 degrees (+).

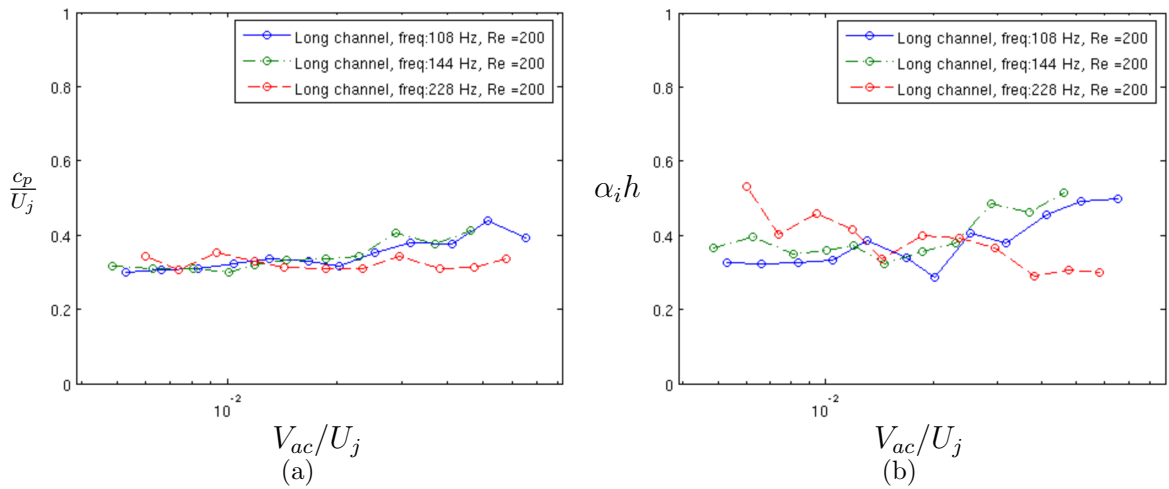


Figure 2.18: a) Dimensionless convection velocity and b) amplification coefficient as functions of the dimensionless acoustic velocity excitation V_{ac}/U_j

Another set of measurements has been carried out to observe the independence of both variables with respect to the amplitude of the excitation V_{ac} . A squared exit is chosen together with three excitation frequencies: 108, 144, 228 Hz which corresponds to Strouhal 0.22, 0.29 and 0.46. The amplitude of the acoustic velocity was varied from 0.03% of U_j up to 1.2%. The results are shown dimensionless in fig.2.18. We observe that both variables remain constant in the range of excitations studied.

2.3 Boundaries of the linear description

Holger's analysis of the fully developed jet [47] is adapted to study the jet oscillation at both boundaries of Rayleigh's linear model. The distance from the flue exit to the place where the jet breaks into vortices (x_c) as well as the amplitude of the oscillation at that position (η_c) are investigated in this section. Elements that are used together with the empirical model proposed in section 2.2.3 to propose a semi-empirical model for the jet oscillation at the origin (η_0). Fig.2.20 shows these values super-imposed over a Schlieren image.

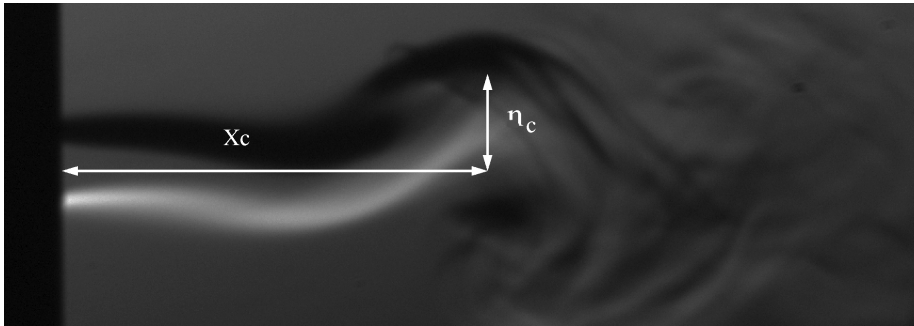


Figure 2.19: Schlieren images with position of the place where the jet breaks into vortices x_c and the amplitude of oscillation at that point η_c

Both the amplitude of the acoustic excitation and the Strouhal number have been observed to have an effect on the parameters studied.

2.3.1 Discrete vortices model

In the context of edge-tone analysis, Holger proposed a model to describe the behavior of the jet when vortices are fully developed, beyond the boundaries of Rayleigh's linear model. In his description, vorticity in the shear layers of the jet grows exponentially downstream, from the flue exit until they reach an ultimate strength observed in a stable vortex street configuration (fig.2.20). Although the model is conceived for edge tones which correspond to a much smaller transverse perturbation (about a factor of 100) the overall description is in good agreement with our visualization (see for instance fig.2.23).

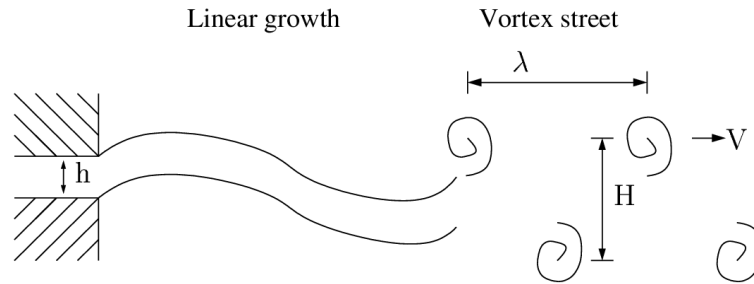


Figure 2.20: Holger's sketch for vortex formation

Momentum balance

In his analysis Holger assumes a parabolic (Poiseuille) velocity profile at the flue exit. Then, using momentum conservation and kinematic observations, he obtains energy transformations and geometric relations.

Doing a similar exercise but with a Bickley profile (eq.2.1) we obtain the momentum of the jet at the flue exit:

$$Mx_{jet} = \rho \frac{\lambda}{V} U_j^2 \phi \quad (2.14)$$

where

$$\phi = \frac{2}{3} b \tanh\left(\frac{h}{2b}\right) \left[3 - \tanh^2\left(\frac{h}{2b}\right) \right] \quad (2.15)$$

The jet momentum is then balanced with the momentum of the vortex street giving the following relation:

$$\frac{H/2}{h} = \left(\frac{\phi}{16} \frac{\pi \tanh^2 \left(\frac{\pi H}{\lambda} \right)}{\left(\left(\frac{\pi H}{\lambda} \right) \tanh^2 \left(\frac{\pi H}{\lambda} \right) - \frac{1}{2} \right)} \right) Str^{-2/3} \quad (2.16)$$

Where Str is the Strouhal number defined as $Str = fh/U_j$, H is the vortex street height and h the channel height as shown in fig.2.20.

Sensitivity analysis

In section 2.2.6, the velocity profile parameter b was observed to be proportional to the channel height h ,

$$h = \gamma b \quad (2.17)$$

The value of γ has been theoretically estimated [85] to be 2/5 through momentum balance assuming a Poiseuille profile inside the channel and a Bickley outside. Our measurements for long and short channels with different central jet velocities show that this value lies between 0.45 and 0.5 (section 2.2.6).

H has been observed to be approximately equal to half of the wave length $H/\lambda = 0.5$ [47], but it depends on the jet velocity profile. Therefore a sensitivity analysis of eq.2.16 needs to be carried out. First, γ is varied from 0.45 to 0.5 as observed in the star-lines in fig.2.21. The street height H slightly increases with γ .

Then, γ is fixed to 0.5 and a Nolle profile is considered (eq.2.2) in which case it is difficult to obtain an analytical expression for $H/2h$ as in eq.2.16 and numerical integration must be used to study the effect of a variation of the exponent n from 2 to 4. Again, we observe in fig.2.21 H growing with γ .

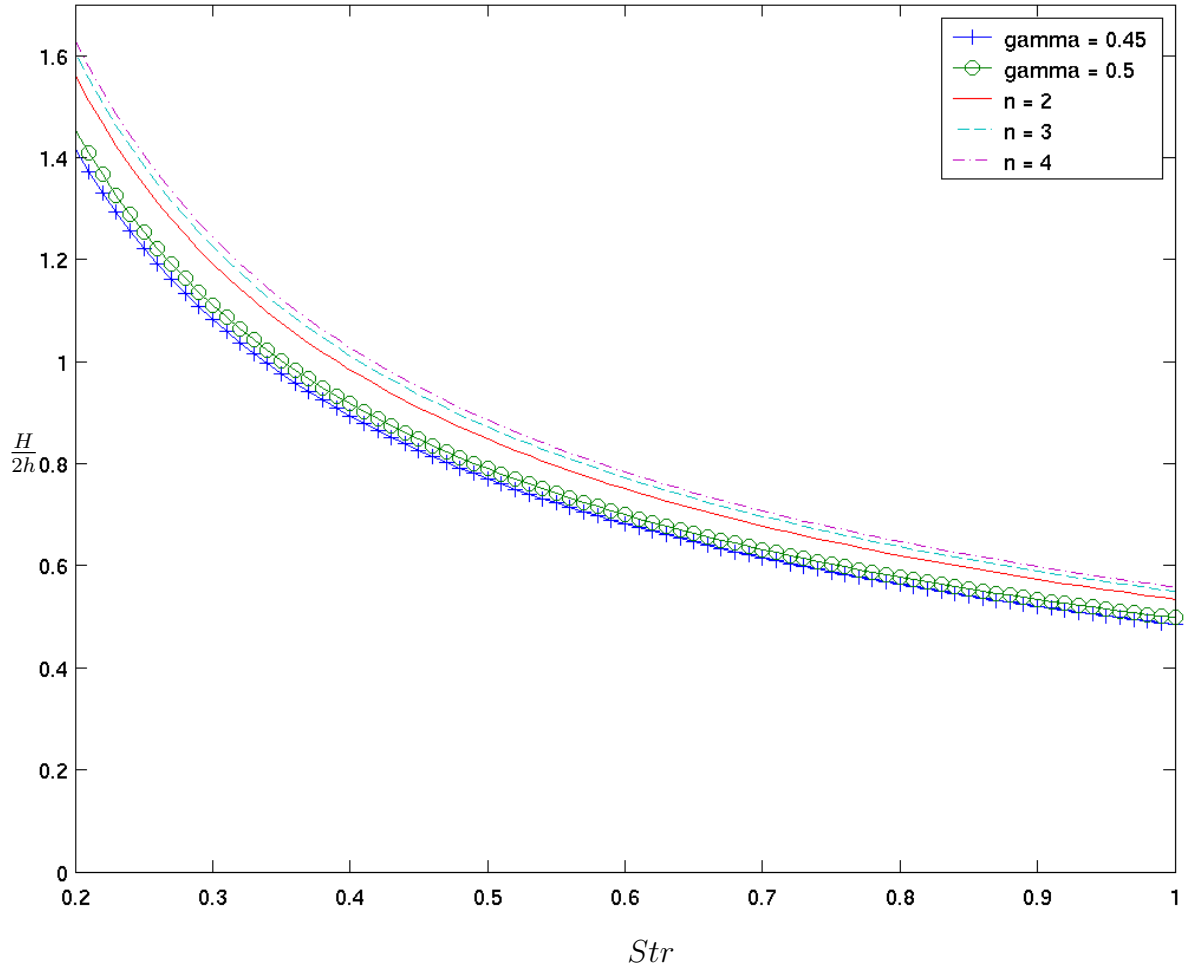


Figure 2.21: Non-dimensional height of the jet perturbation at the jet transition ($H/2h$) as function of Strouhal. Sensitivity analysis with respect to γ ($b = \gamma * h$) and with respect to the exponent n of the Nolle profile (eq.2.2) for γ fixed = 0.5

Upper boundary

Visualizations of oscillating jets (fig.2.22) show that $H/2$ can set as an upper boundary to η_c .

$$\eta_c \leq H/2 \quad (2.18)$$

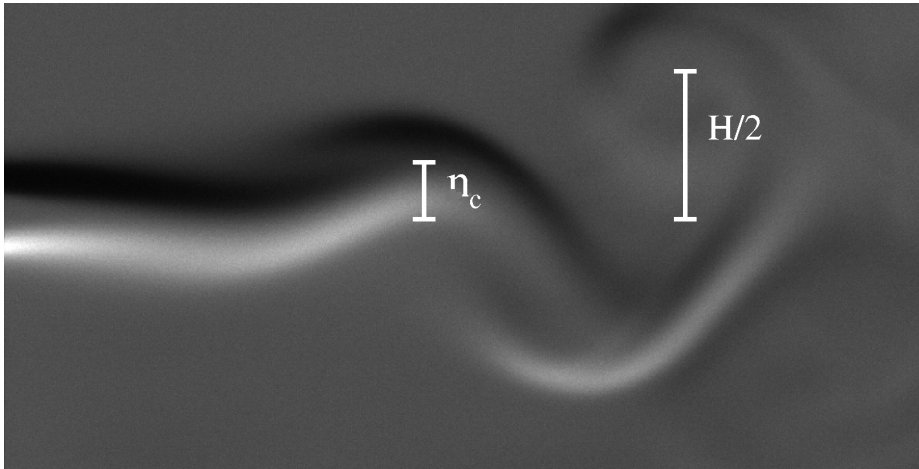


Figure 2.22: Approximate values for η_c and h shown with a Schlieren image

Using that assumption, we proceed with experimental measurements to study the dependencies of x_c and η_c on the amplitude of the excitation V_{ac} and the Strouhal number.

2.3.2 Experimental protocol

A setup similar to that described in section 2.2.4 was used. A central jet velocity of 3 m/s (Reynolds = 200) and a frequency of oscillation of 108 Hz (Strouhal = 0.22) was chosen. This combination provides a convenient oscillation where the parameters x_c and η_c can easily be detected.

The amplitude of the acoustic velocity was varied from 0.5% of U_j up to 7%. These values are below the 10% observed in real flutes, but it is a restriction imposed by the power handling of the speakers.

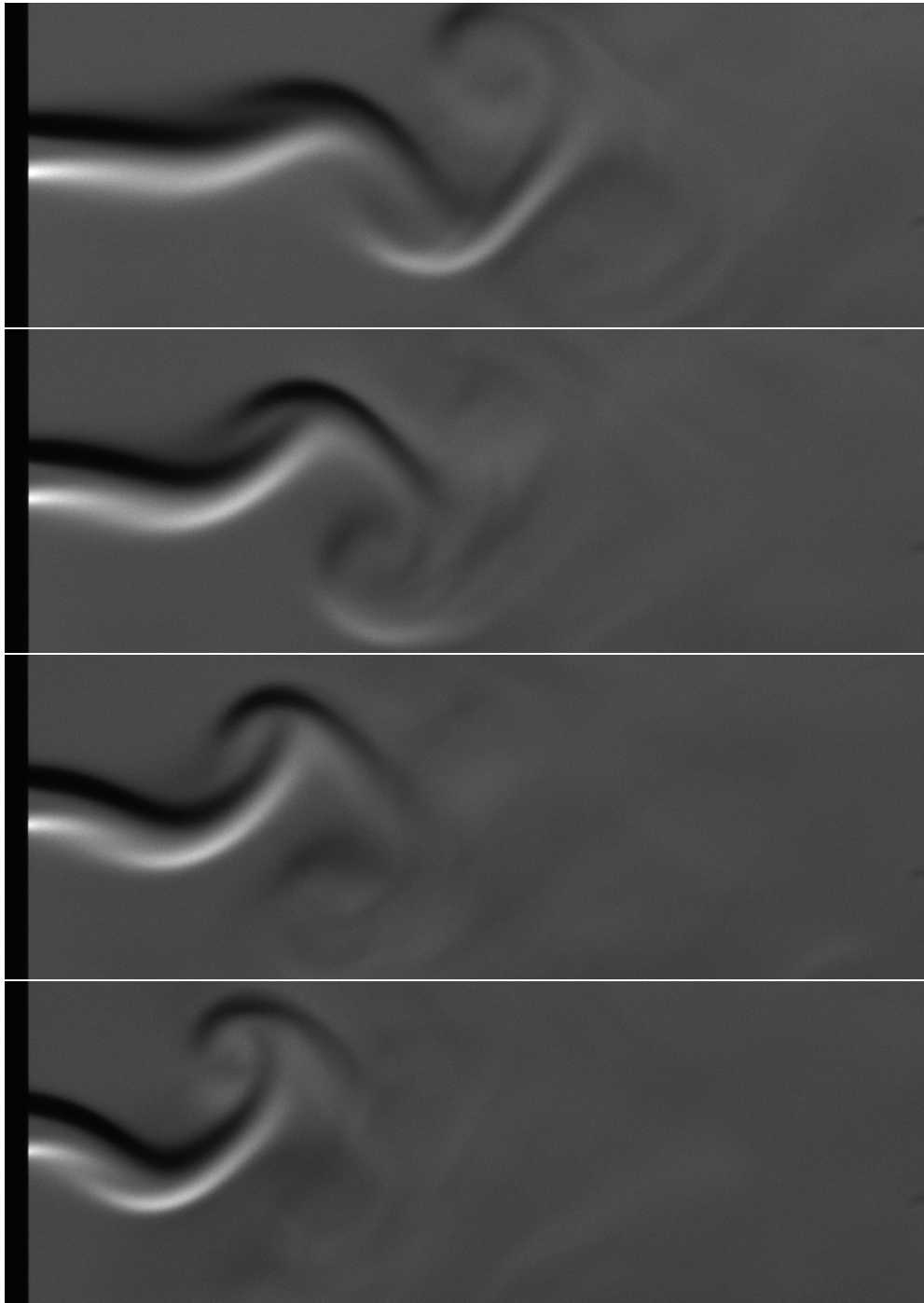


Figure 2.23: Images obtained via Schlieren technique. Reynolds: 200, Jet speed: 3 m/s, Excitation freq.: 108.24 Hz, Strouhal: 0.22. From top to bottom V_{ac}/U_j : 0.53%, 1.3%, 2.54%, 6.54%.

2.3.3 Perturbation at the transition

Detecting x_c and η_c

A feature of the cross-correlation method was used to detect x_c and η_c from Schlieren images: the cross-correlation between images works properly only when the light intensity shape of a particular column translates from one image to another with a similar shape. This is the case in the laminar portion of the jet, from the flue exit to the point where the jet breaks into discrete vortices. Beyond this point, the intensity profile of the image columns becomes incoherent and sinusoids don't fit the data properly.

In fig.2.11(b) we observe the amplitude growing exponentially until approximately the point where the jet breaks into vortices, x_c and η_c are measured at the maximum of this curve, which is considered the breaking point between the two models outlined by Holger.

Amplitude of the perturbation η_c at the transition point

The measured amplitude of the perturbation η_c at the transition point is displayed in fig.2.24 as a function of Strouhal. We observe a decaying shape similar to that predicted by eq.2.16. A curve for $H/2h$ from eq.2.16 with $\gamma = 0.5$ and $n = 2$ is superimposed over the data. Measured values are in good agreement with the proposed model.

η_c is also displayed as function of the dimensionless amplitude of the acoustic velocity V_{ac}/U_j in fig.2.25(a). The data shows a constant behavior for the range of values studied. Therefore, η_c does not seem to depend on the amplitude of the excitation V_{ac} . The value observed for this particular case is around 2 and is expected to depend on Strouhal, as will be discuss later.

Horizontal position of the transition x_c

The experimental results obtained for x_c are shown as a function of the dimensionless amplitude of the acoustic velocity V_{ac}/U_j in fig.2.25(b).

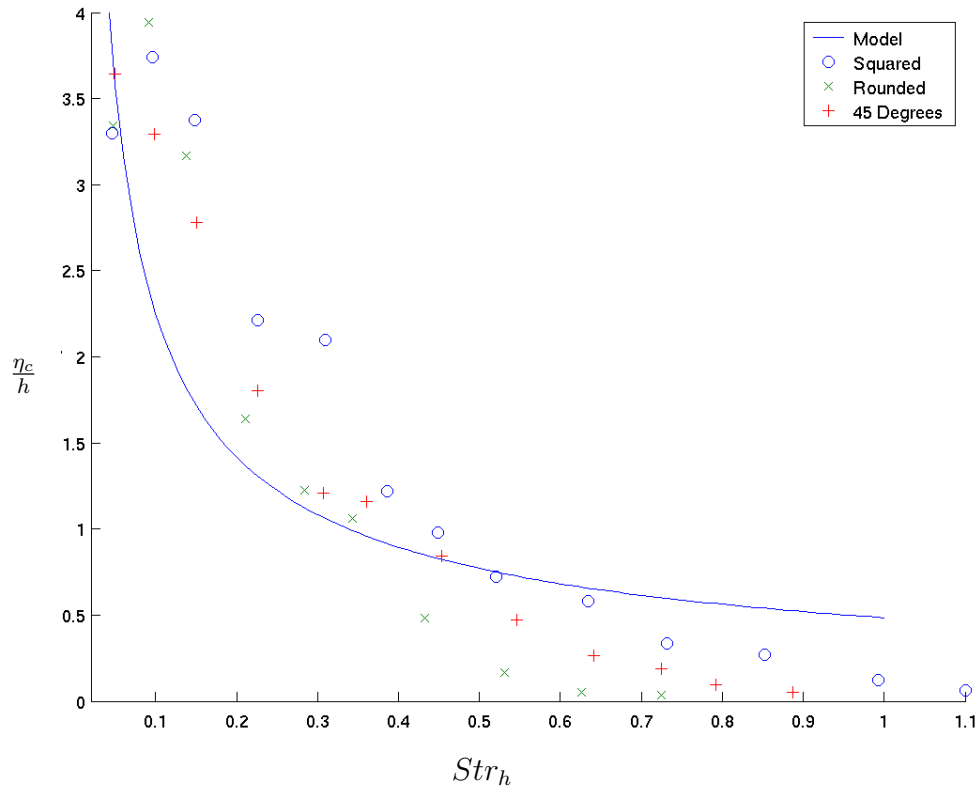


Figure 2.24: Model estimation for the jet displacement at the transition point η_c , eq.2.16 (solid line) and data obtained through experimentation for flue exits Squared (o), Rounded (x) and 45 Degrees (+)

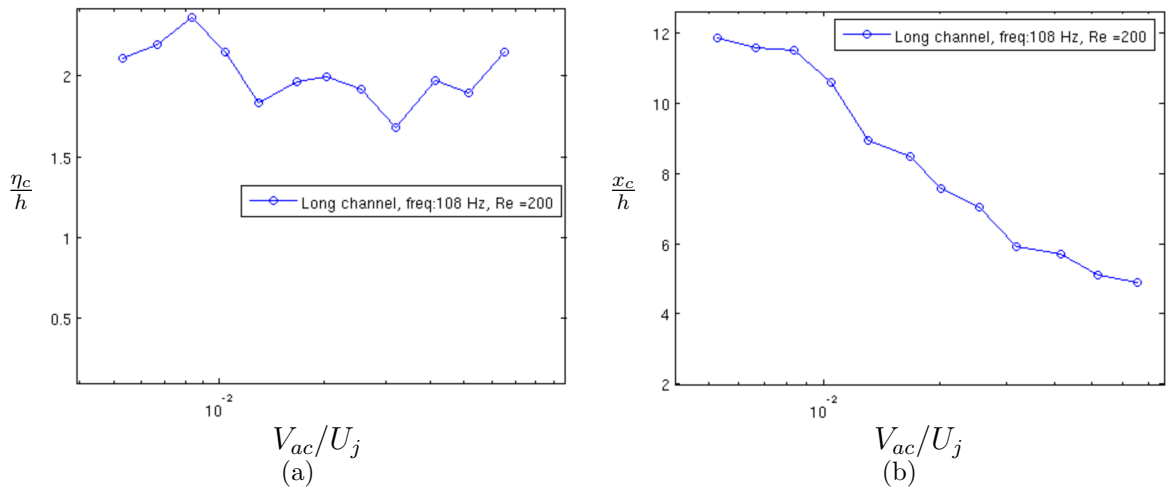


Figure 2.25: a) Displacement of the jet at the transition point η_c . b) Distance from the flue exit to the transition point on the jet x_c . Flue exit squared. Reynolds = 200

As a first approximation, it appears that x_c follows a logarithmic decay, which can be expressed in a dimensionless form as :

$$\frac{x_c}{h} = \frac{x_0}{h} - k \log \frac{V_{ac}}{U_j} \quad (2.19)$$

Where x_0 and k are parameters to fit from the data. A more detailed model should take into account the dependency of x_c and η_c on Re and Str .

In the literature, the horizontal position at which the jet breaks into vortices x_c has been assumed to be of the order of 1 to 3 hydrodynamic wavelengths [47].

2.3.4 Perturbation at the flue exit

There is no analytical model in the literature for the initial amplitude and phase of the jet perturbation.

Amplitude of the perturbation at the flue exit

As discussed in section 2.2.3, our analyses show that the jet oscillation can be described, after a short distance from the flue exit, by equation 2.9. With an exponential growth of the oscillating amplitude $\hat{\eta}(x) = \eta_0 e^{\alpha x}$. We can also consider $H/2$ from eq.2.16 to be the upper boundary for the amplitude of oscillation $\eta_c \leq H/2$. Thus, combining equations 2.9, 2.16 and 2.19, we estimate a boundary for the initial amplitude of the perturbation :

$$\frac{\eta_0}{h} \leq \frac{\epsilon}{e^{\alpha x_0}} \left(\frac{V_{ac}}{U_j} \right)^{kh \log e} Str^{-\frac{2}{3}} \quad (2.20)$$

Where ϵ is taken from eq.2.16

$$\epsilon = \left(\frac{\phi}{16} \frac{\pi \tanh^2 \left(\frac{\pi H}{\lambda} \right)}{\left(\left(\frac{\pi H}{\lambda} \right) \tanh^2 \left(\frac{\pi H}{\lambda} \right) - \frac{1}{2} \right)} \right) \quad (2.21)$$

2.3.5 Discussion

Frequency dependence of η_c and x_c

Both η_c and x_c have been observed to depend on frequency in a way that the bigger the frequency the smaller η_c and x_c . This dependency has been studied in another set in which three frequencies of oscillation are chosen: 108, 144, 228 Hz corresponding to Strouhal 0.22, 0.29 and 0.46 and the amplitude of the excitation V_{ac} is varied in the way described in section 2.3.2.

η_c and x_c are made non-dimensional through the characteristic distance U_j/f which is proportional to the hydrodynamic wavelength $\lambda_h = C_p/f$ when the convection velocity C_p is independent of frequency. That is the case over the range of frequencies of interest, as observed in fig.2.14(a).

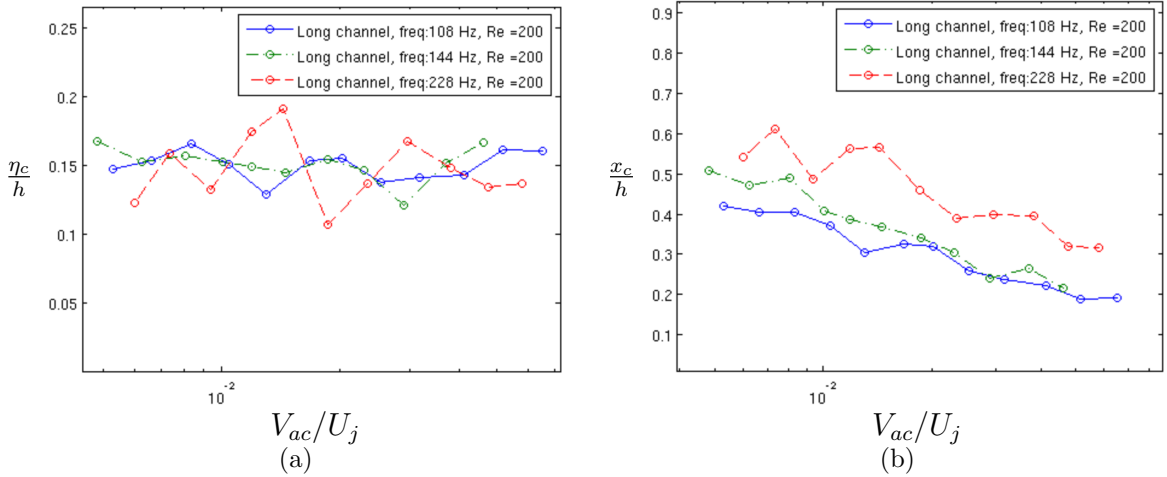


Figure 2.26: a) Displacement of the jet at the transition point η_c . b) Distance from the flue exit to the transition point on the jet x_c . Flue exit squared. Reynolds = 200. Frequencies 108, 144 and 208 Hz

The displacement at the transition point η_c is shown in fig. 2.26(a). The curves for the three frequencies collapse into one flat line, which shows that the non-dimensional value $\frac{\eta_c f}{U_j}$ captures the relation between the variables involved and that η_c can probably be better explained as function of the hydrodynamic wavelength λ_h .

The distance from the flue exit to the transition point x_c is presented in fig. 2.26(b). A logarithmic decay is observed again. The three curves are closer to each other than in the case where they are made non-dimensional with respect to the jet height h . This shows that the proportionality between the hydrodynamic wavelength and x_c is a correct first order description and that it probably can be improved with a non-linear relation between the two parameters.

Amplitude of oscillation and frequency dependence of η_0

Our model for the amplitude of oscillation at the origin η_0 shows a dependency on the Strouhal as $Str^{-2/3}$ as shown in eq.2.20, which corresponds with the overall shape of our measurements shown in fig.2.27

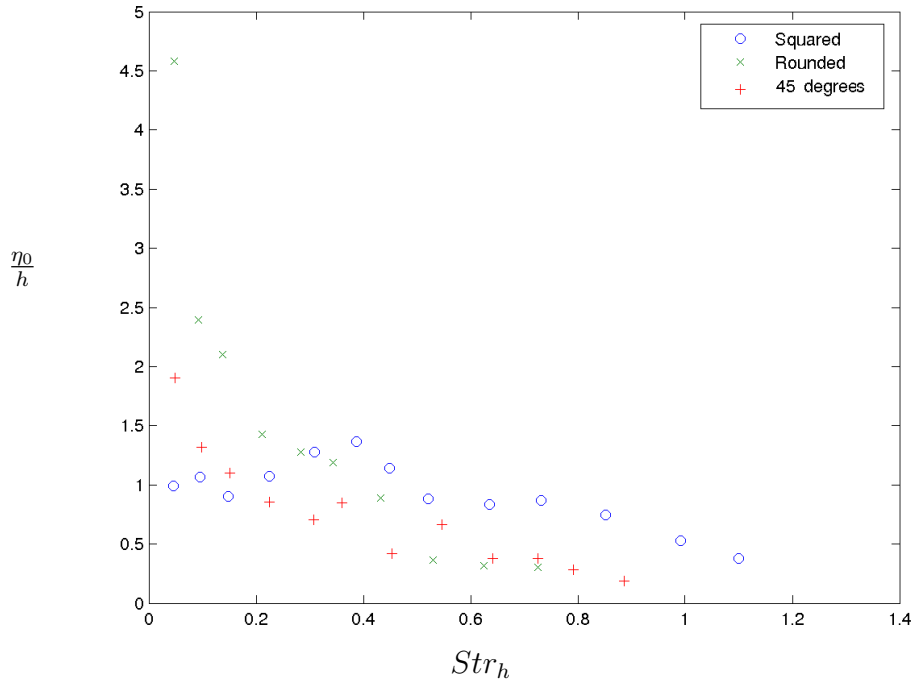


Figure 2.27: Perturbation at the jet origin η_0 as function of Stouhal. Reynolds = 200, flue exits Squared (o), Rounded (x) and 45 degrees (+)

When η_0 is displayed as function of the acoustic excitation V_{ac} we observe a decay of the shape as $1/\omega$. Searching for a relevant variable to make it non-dimensional we observe that the hydrodynamic wavelength has no influence close to the jet exit and

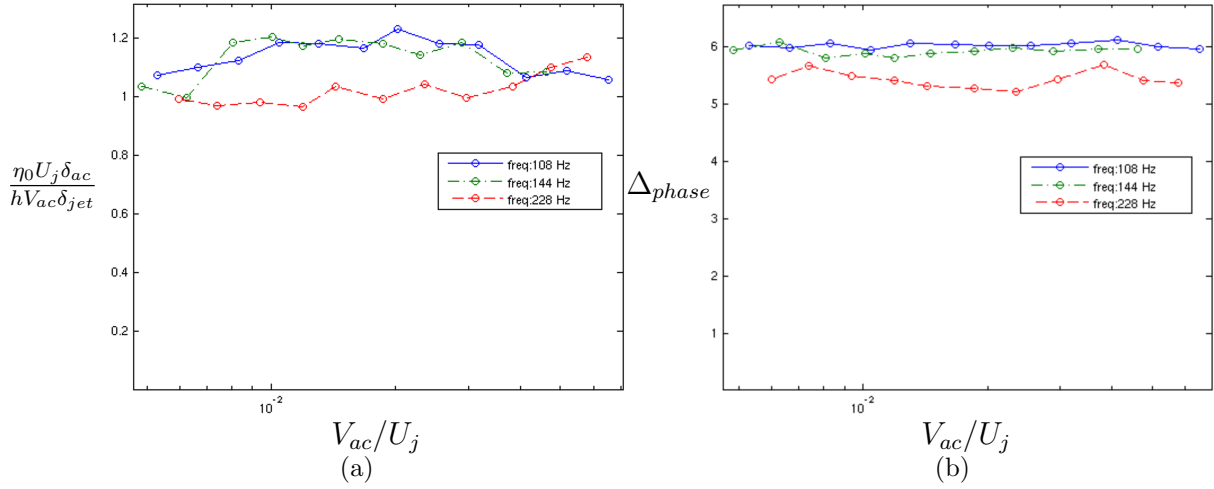


Figure 2.28: a) Perturbation at the jet origin η_0 as function of the non-dimensional acoustic velocity V_{ac}/U_j . b) Phase difference between the acoustic excitation V_{ac} and the jet oscillation at the origin η_0 . Reynolds = 200. Frequencies 108, 144 and 208 Hz

reasonable quantities to include in the description would be the shear layers of both the jet δ_{jet} and the acoustic field close to the wall $\delta_{acoustic}$.

$$\delta_{jet} = \frac{L}{\sqrt{Re}} \quad (2.22)$$

$$\delta_{acoustic} = \sqrt{\frac{2\nu}{2\pi f}} \quad (2.23)$$

Using these two values we propose to include in the analysis the following non-dimensional number:

$$\frac{\eta_0 U_j \delta_{acoustic}}{h V_{ac} \delta_{jet}} \quad (2.24)$$

Fig.2.28(a) shows the results obtained using it. Again, we observe the three lines collapsed together producing a constant value of 1, which validates the assumption that the shear layers have an influence on the jet receptivity. An accurate model would need a detailed description of the total flow (from jet and from acoustics) at the flue exit.

Phase between the perturbation and the jet oscillation at the flue exit

The phase difference between the acoustical excitation V_{ac} and the jet displacement at the origin η_0 is obtained from the image analysis and is displayed in fig.2.28(b). The phase difference remains very close to 2π (or zero –which is the same in this case) for the range of excitations and frequencies studied, showing that both signals are in phase.

The phase difference observed here differs from the semi-empirical models proposed by Fletcher and Verge which predict a phase difference of $\pi/2$.

2.4 Conclusion

Jet visualizations together with data analysis have been utilized to study the behavior of a jet perturbed by an oscillating acoustic field. They provide non-intrusive and powerful tools to study the excitation mechanisms in flute-like instruments.

The new tools have been used to study problems that haven't found an adequate explanation through conventional methods, such as the influence of the excitation geometry in the jet instability and receptivity; they also provide a useful alternative to validate observations made in different contexts, such as the relation between the jet velocity profile and the convection velocity of the perturbation.

Throughout this chapter, a set of experiments has been described which study jet receptivity and instability. Observations, analysis and preliminary models have been proposed for the described problems. Above all, we have demonstrated a promising tool that can be used to further explore some of the mysteries of the operation of flute-like instruments.

Chapter 3

Analysis of flute control parameters

Abstract

The sound produced by flutes depends not only on the physical characteristics of the instrument but also on the control exerted by the musician. The latter is very important in some instruments of the flute family, especially in those where the air jet is shaped with the lip of the player. Some of the most relevant parameters controlled by the flautist, such as the distance from the lips to the sharp edge, the shape of the lips hole and the speed of the jet, are experimentally measured in this chapter. Data produced by an experienced and a novice flautist are collected, analyzed and compared. Subjects are studied under normal musical playing conditions, playing phrases made out of simple musical intervals with subjective dynamics. Images of performer's lips are taken together with measurements of the blowing pressure and the sound radiated by the instrument. Data analysis shows remarkable differences between the two subjects. The optimized coordination of several parameters in order to obtain a desired musical response, coupling between performer's mouth and the instrument, as well as the efficient use of the available resources are some of the differences observed.

3.1 Introduction

The control exerted by the performer on the instrument can be of crucial importance in the quality of sound produced. There are some instruments from the flute family such as organ pipes where the quality of the final sound is left almost entirely to the design of the instrument builder. The other extreme is where the interaction of the performer has an enormous influence on the quality of sound produced, such is the case for the European transverse flute, the South American quenas and the Japanese shakuhachi.

While manipulating the excitation mechanisms has the most effect on the sound quality, some instruments allow for a degree of tone control through changes in the resonator. Cross fingering and half holing techniques used in instruments like the shakuhachi have a clear effect in the tone of the instrument. In this chapter we concentrate on the control exerted through the excitation mechanisms on the European transverse flute.

Producing sound on a modern transverse flute normally requires only a few weeks of training, though it typically takes a couple of years to be able to produce the standard compass (C3(262Hz) - B5(1319Hz)). Good control of the sound quality to perform at professional level takes at least 10 years [82, 44].

The performer orchestrates simultaneous and synchronized control over several parameters. The air pressure is modulated in the lungs to produce a desired air jet velocity. The tongue provides an exit valve that is used to produce the different types of attacks and, in combination with the velocity of the outgoing air jet, shape the global intention of musical phrases. The geometry of the lips hole shapes the cross section of the air jet and by pushing the lips forward and backward the flautist controls the distance the jet travels before reaching the sharp edge. This movement also alters the surface of the open extremity and therefore the input impedance of the tube [12]. Through years of practice an experienced flautist learns refined controls over the mechanisms described above.

Several books and methods have been published (ex. [82, 44]) describing the embouchure techniques from a pedagogical point of view. Throughout this chapter

data is analyzed from the point of view of the physics of the air jet excitation of the flute, and is interpreted in terms of the current knowledge of the physics of flute-like instruments.

Measurements captured from two flautists, one experienced and the other a novice, are analyzed and compared aiming to fulfill two principal objectives: observe the equilibrium between the different parameters that are necessary to produce a flute tone, and contrast the differences in control applied by the two players. Data can also be generalized to provide a simplified caricature of the flautist's behavior, which could be useful to provide synthesis control inputs for a flute physical model. A study with more subjects remains to be done to generalize some of the observation of this chapter.

The article is structured as follows: Section 3.2 presents a summary of the current knowledge of the physics of flute-like instruments to determine the parameters that need to be measured. Section 3.3 presents the experimental setup used to do the measurements and Section 3.4 presents the data and its processing. The analysis of the playing of the experienced flutist is then presented in Section 3.5 and Section 3.6 compares the behavior of the experienced and novice player. Finally, the main results are discussed in Section 3.7.

3.2 Basic flute model : current state of knowledge of flute-like instrument physics

Flute operation can be globally described as a coupling between the hydrodynamic modes of a jet with the acoustic modes of a resonator. An integral approach of this problem has been proposed by Howe [48], Crighton [21] in the case of the edge-tone, Elder [28] and Bechert [4], for simplified geometrical conditions. The pipe resonances depend, among other things, on the characteristics of the pipe ends. The operation of the jet takes place in one open end, which is also where part of the acoustic radiation of sound takes place. Therefore a lumped study of the pipe resonances, the jet instability and the aero-acoustic sources induced by the jet is questionable, as discussed in [32].

However, the description of the flute operation in such independent elements is more tractable and has become very popular in the literature [87, 37, 18]. The different elements (resonator, jet, sources) are supposed to interact locally and are therefore analyzed separately and then concatenated to produce a simplified caricature of the flute operation, as sketched in fig.3.1.

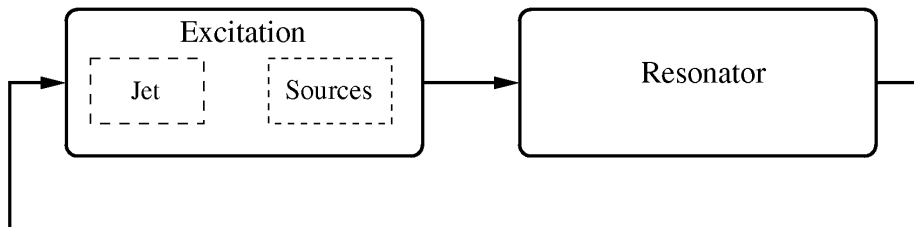


Figure 3.1: General description of flutes operation

The acoustic resonances of the flute body have been studied in details by Fletcher [41], Wolfe [89], Benade [6], Coltman [15], Castellengo [9], Nederveen [63]. The pipe may then be described by its input acoustic admittance at the embouchure hole.

The jet transverse oscillation induced by a harmonic acoustic perturbation is expressed as the propagation of a wave of growing amplitude. For soft blowing conditions, the jet is laminar. The instability of a laminar jet was first described by Rayleigh [72] and followed by Mattingly & Criminale [57], Fletcher [42], Nolle [64], Ségoufin [76]. The convection velocity as well as the spatial amplification factor of the wave are function of the dimensionless frequency, the Strouhal number ($Str_h = fh/U_j$ where f is the frequency, h is the height of the flue from where the jet flows and U_j is the velocity of the jet centerline).

Following Nolle [64] and de la Cuadra [23], the jet instability appears to be maximum around:

$$0.02 < Str_h = fh/U_j < 0.05 \quad (3.1)$$

depending on the jet velocity profile. For a jet issuing from a very short channel such as the player's lips, the velocity profile is expected to be sharp [77, 64] and the maximum amplification of the instability is expected for $Str_h \approx 0.03$.

The structure of the jet is related to the Reynolds number ($Re = U_j h / \nu$, where ν is the kinematic viscosity of the air, $\nu = 1.510^{-5} m^2/s$). When blowing harder, the jet becomes turbulent. Although difficult to predict [83, 55], the transition from laminar to turbulent jet seems to occur in the range $Re = 2500 - 3000$. Re up to 10000 has been measured in the higher register of the flute. Because of the chaotic nature of turbulence and of the fast kinetic energy dissipation induced, the instability of a turbulent jet submitted to a transverse acoustic field is more difficult to describe. The work of Bechert [4] offers a simplified model, while the work of Thwaites [80, 81], shows a way to transpose the results obtained for laminar jet to weakly turbulent jets. Turbulence is known to produce a breathy wide band noise [55, 48]. As discussed by Verge [84], this noise filtered by the passive resonance of the pipe is an important part of the perceived characteristic flute sound. In western classical technique, the player is expected to reduce as much as possible this part of the flute sound, while it is considered as an expressive resource that needs to be enhanced and controlled by the player in other musical practices such as the traditional Japanese shakuhachi technique [10].

Laminar and turbulent jets may be used in normal operation of flutes, and because the transition from laminar to turbulent is dependent on the upstream flow conditions, one might expect an experienced performer to be able to influence that transition.

Changing the blowing pressure allows the flautist to adjust the delay induced by the convection of perturbations on the jet. As shown by Coltman [13], the flute sounds at the frequency of its passive resonance for a delay equal to half of the oscillating period. This corresponds to the optimal phase relation of the sound source at the labium compared to the acoustic field as discussed by Fabre [33]. Coltman also shows that, in order to develop the harmonic content of the sound, players may blow at pressures a little higher than this optimal pressure, resulting in a playing frequency slightly above that of the passive resonance of the pipe. The convection velocity of perturbations on the jet is about 30% to 50% of the jet centerline velocity [72], the optimal condition corresponding to half a period delay on the jet may be expressed

as :

$$Str_W = \frac{fW}{U_j} = 0.15 \dots 0.25 \quad (3.2)$$

where W is the flue-exit to labium distance. Combining equations 3.1 and 3.2, the optimal range of the thickness ratio W/h of the jet is :

$$3 < W/h = \frac{Str_W}{Str_h} < 12 \quad (3.3)$$

In the case of a short channel like the lips, the maximum jet instability occurring at $Str_h \approx 0.03$ indicates an optimal value of $W/h \approx 8$.

The acoustic pressure at the flue exit may induce a modulation of the jet velocity at the frequency of the sound. A simple model of the influence of the mouth cavity on the jet velocity fluctuations has been proposed by Verge [86]. Jet velocity fluctuations are expected to induce varicose modes on the jet. In the case of a short channel like the lips, the jet velocity fluctuations are shown by Verge to induce acoustic losses. The effect of the varicose modes on the harmonic content of flute sound is not fully understood yet.

Finally, the production of acoustic energy by the oscillating jet is commonly described as a dipole [16, 85, 27, 60] with a strength proportional to the total jet flow Q_j .

In the present research, the players' control is analyzed in terms of the physics of the sound production. Therefore the main control parameters measured (W, h, U_j) are analyzed in terms of the dimensionless numbers discussed above : Str_W, Str_h, Re .

3.3 Control parameters and experimental setup

Among the large number of parameters controlled by the flautist, a limited group has been selected for the measurements. The parameters chosen are those presumed more relevant to the sound production. There are also some parameters not incorporated for reasons of technical simplicity, this is the case of jet angle of incidence and the

labium offset with respect to the jet axis, which would require a more complex setup to be measured.

The experiment was done in a small room without anechoic treatment. The dimensions of the room are 2.76 x 6.45 x 3.15 mts (56 mts³) which provides an environment similar to that found in a normal practice room. The experiment has been set as close as possible to the normal playing conditions except that the flute was fixed with the help of a camera tripod and therefore the flautist needs to accommodate his body to the position of the flute, and cannot turn it in or out. This was a necessary compromise to assure the accuracy of the measurements. The perceived sound quality produced by both subjects was very close to what they would do in normal conditions.

The musical material chosen included intervals such as fifths, octaves and scales, and some dynamic changes like *crescendo* and *diminuendo*. The “score” explores the complete register of the instrument as well as specific issues in flute technique.

Fig.3.2 shows a scheme of the setup. The flute used for the experiment is a Yamaha 281 S, a very popular beginner flute, silver plated and with C-foot extension. To measure the pressure inside the mouth cavity, the end of a calibrated differential pressure sensor is placed inside the mouth of the player through a soft tube (23.5 cm. long and 1 mm. internal diameter). Another microphone is placed 1.5 m away from the embouchure to register the radiated sound.

A digital camera is placed 2 meters away from the embouchure. It is almost aligned with the direction of the air jet, intending to catch a frontal view of the lips hole. Images are taken at a rate of 17 images per second, which provides a sufficiently large sampling rate to capture the dynamics of the control. A mirror is placed near the embouchure forming an angle of approximately 45 degrees with the flute and thus providing a lateral view of the lips when observed from the front. Fig.3.3 shows the type of images captured by the camera.

3.4 Data processing

The pressure measured inside the mouth p_m contains a slowly moving component P_m added to a fast moving component p'_m that oscillates at the frequency of the note

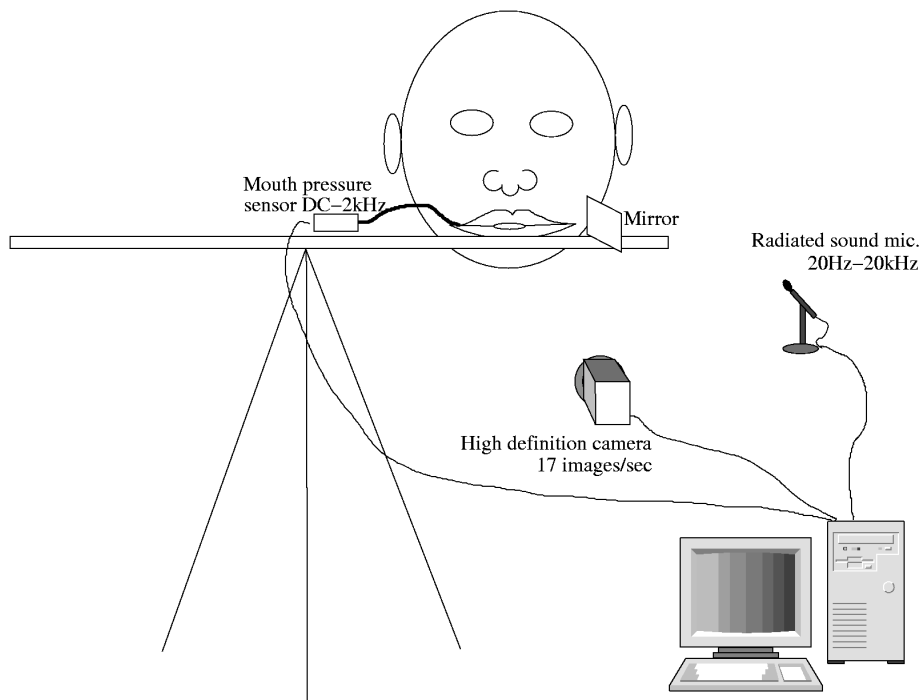


Figure 3.2: Experimental setup.

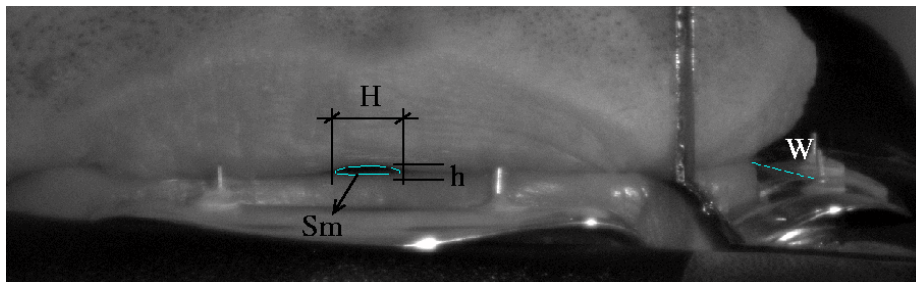


Figure 3.3: Image captured by the camera with detection of lips hole and flue-labium distance, showing on the right of the picture the 45° mirror that allows to measure simultaneously lip opening and lip-edge distance.

played, $p_m = P_m + p'_m$. The two signals are isolated through filtering with a cutoff frequency of 100 Hz.

Considering the very short length of the flue channel formed between the lips of the player, the flow boundary layers are assumed to be negligible and the mean jet velocity (U_j) is estimated using Bernoulli's equation :

$$U_j = \sqrt{\frac{2P_m}{\rho_0}} \quad (3.4)$$

where ρ_0 is the air density.

Frontal and lateral images provide the raw data from where geometrical information is extracted: the area of the lips hole (S_m), the height (h) and width (H) of the hole, and the distance from the lips to the sharp edge (W), as shown in fig.3.3. The detection of these parameters is based on a morphological analysis of the images, which includes stretching the contrast, black and white conversion, and edge detection. Two independent analyzes are carried out to detect the lips hole parameters and the lips-to-edge distance.

The radiated sound (p'_{rad}) captured by the external microphone is used to estimate the frequency of the note played (f) and the energy radiated. The harmonic product spectrum algorithm is used to pitch track the signal as described in [24]. The total jet flow is estimated as $Q_j = U_j S_m$. Finally the values of signals sampled at audio sampling rate (44100 Hz) are decimated to synchronize with the parameters measured at images rate (17Hz) through low-pass/down-sampling techniques to avoid aliasing. The left side of fig.3.4 shows an example of the collected data.

3.5 Experienced flautist analysis

In the following section we examine data produced by the experienced flautist (F_A) who has completed a formal musical education and has been playing the flute for more than 20 years. The scope of this analysis of sound production is described in section 2.

3.5.1 Three cases : D major scale, diminuendo and octaves

First F_A is asked to play a D major scale from D3 (293Hz) to A4 (880Hz) with a constant dynamic mf . Details of measured and calculated data are shown in fig.3.4. It is observed that P_m follows the pitch raise, as it was also observed by Fletcher [35]. A zoom on the data shows that the pressure fluctuations in the player's mouth p'_m are at the same frequency as the played tone. The mean blowing pressure P_m increases of a factor 2 (300 to 600 Pa) over the scale, corresponding to a factor 1.4 in the jet velocity while the frequency increases by a factor 3. The jet length W is decreased by a factor 1.8 (8mm to 4.5mm). The combined adjustment of blowing pressure and jet length allows the Strouhal number Str_W to present a small variation (0.1 to 0.15).

The increment in the jet velocity seems to be compensated by a decrease of lips hole surface, yielding a decreasing total jet flow Q_j , that could be interpreted as an attempt to keep the loudness of the radiated sound more or less constant. Indeed the player was asked to play the scale at constant dynamics.

For complementary observation, the player was also asked to play constant pitch B4 (494Hz) decreasing the loudness of the note: the data measured and calculated for a *diminuendo* are shown in fig.3.5. Here again, the large variation of blowing pressure is partly compensated by adjusting the jet length W to keep Str_W almost constant. It is furthermore observed that Re , Q_j and W follow the dynamics of the note in just the right proportion to maintain stability of f and Str_h . Playing both *crescendo* and *diminuendo* show values of Str_W ranging from 0.14 at the loudest to 0.23 at the softest.

Playing loud is difficult in the flute because of its natural tendency to jump to the higher pipe resonances when blowing harder. This is indeed the case for the octaves from first to second register that make use of the same fingerings to play the two notes one octave apart. For instruments of fixed blowing geometry, like the recorder, the jet length W is fixed and doubling U_j is required to double the frequency (octave) while keeping the same relative position of the frequency played with respect to the passive resonances of the tube, in other words, keep Strouhal number Str_W constant. In the transverse flute W can be adjusted while playing so that, if desired, the combined effect of the two parameters can stabilize Str_W .

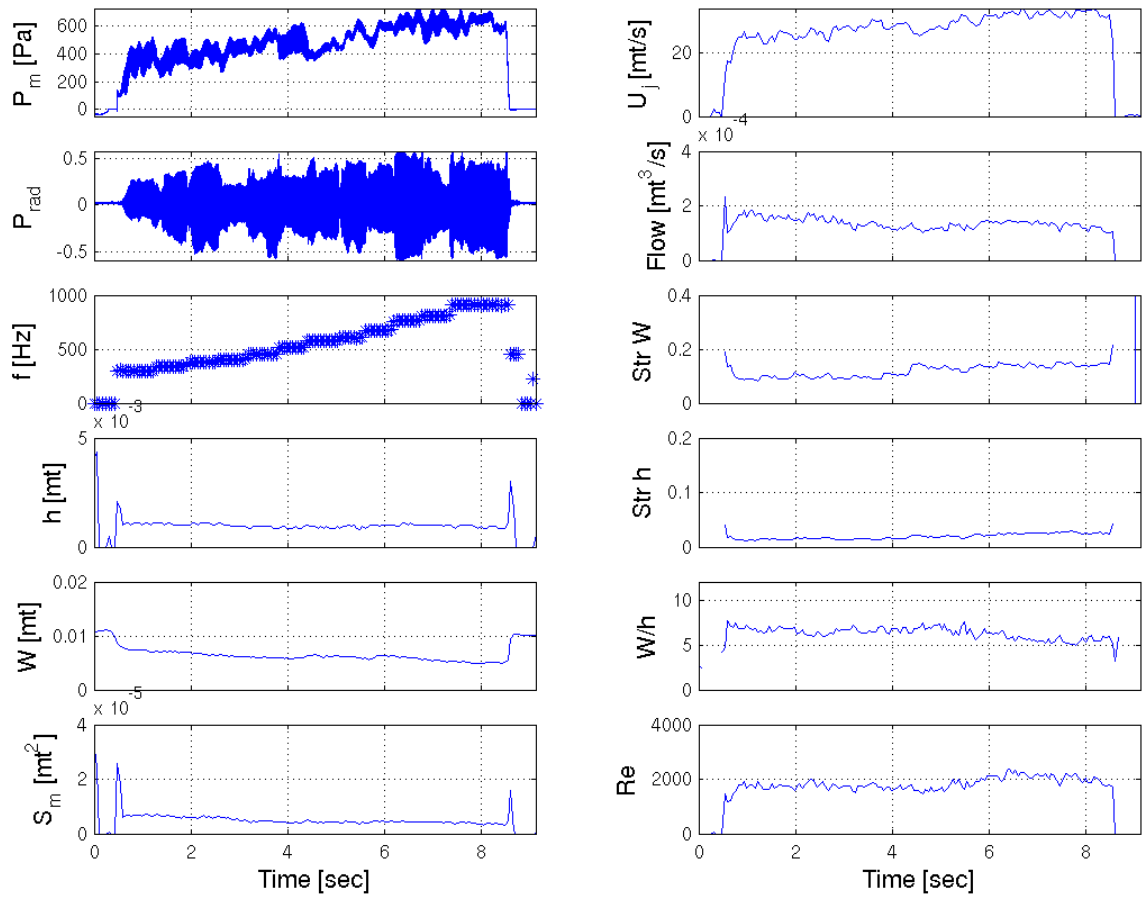


Figure 3.4: Parameters measured and calculated for the experienced player F_A playing a slurred D major scale from D3 (293Hz) to A4 (880Hz)

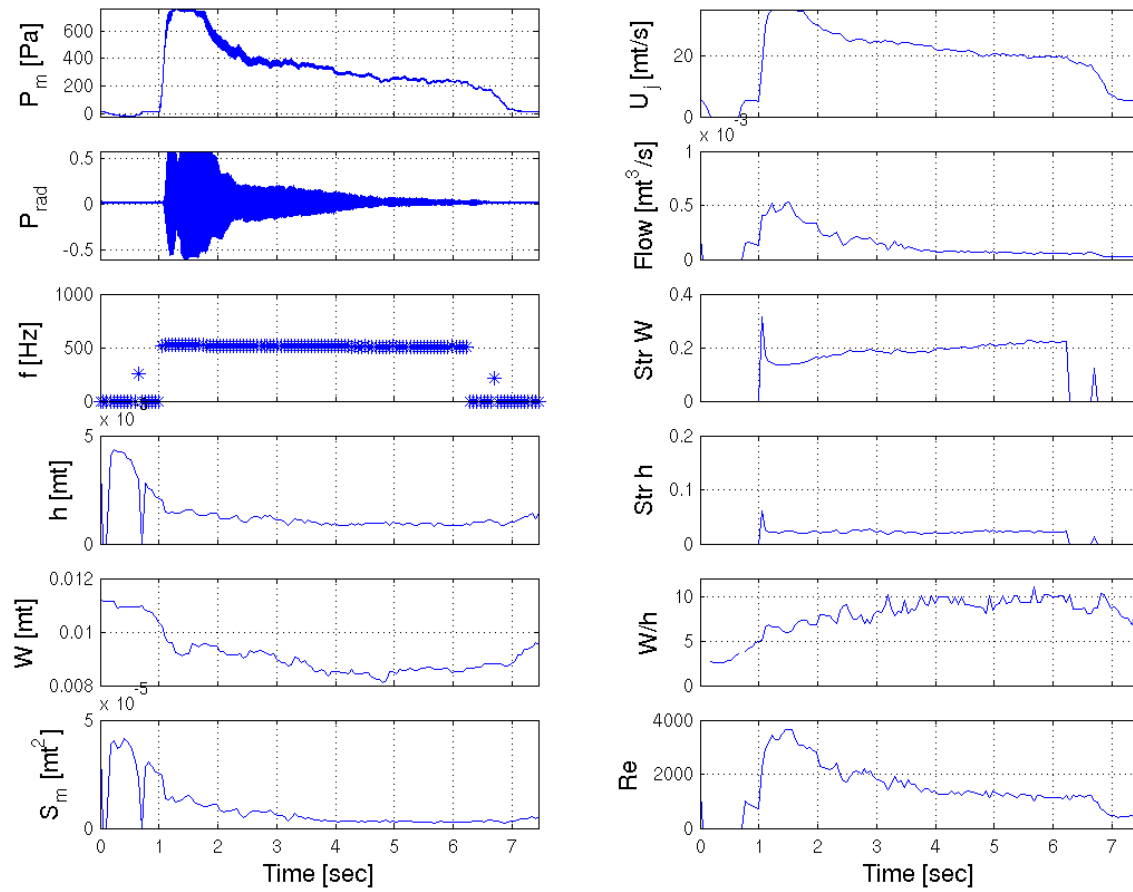


Figure 3.5: Parameters measured and calculated for the experienced player F_A playing a B4, diminuendo

It is then interesting to observe the minimum value of Str_W above which the oscillation would jump to the octave for intervals D3 to D4, up to G3 to G4. The data is presented in fig.3.6. The octave jumps appear to happen at $Str_W \approx 0.1$ which is slightly lower than the minimum value observed for *crescendo* playing and suggest a lower limit.

Measurements on playing the octaves also show that control parameters P_m , W and h , change very little for octave jump, inducing a jump of almost a factor 2 in Str_W and Str_h . Consequently, it is very difficult to identify the mechanisms utilized to trigger the jump, except for the octave D3-D4 that relies on the opening of the octave key. Obviously, the player is trying to play both notes very closely in terms of the control parameters, which requires a fine control and relies on the hysteresis between registers as discussed by Ségoufin [77]. Further work is required to understand the way in which octave jumps are triggered.

3.5.2 Global analysis

Aiming to identify common patterns in the control applied by F_A , several musical excerpts are analyzed together.

A global tendency to increase U_j with frequency has been observed. Fig.3.7(a) shows the jet velocity U_j as function of frequency for an ascending chromatic and diatonic scale. Every point represents the estimated velocity between two consecutive images. It is observed that the variation of U_j is small, about 1.35 of increment per octave. At the same time the jet length W decreases as shown in fig.3.7(b), as observed also by Coltman [12]. The combination of these two parameters produces a variation of the Strouhal number Str_W which remains in the range [0.1 - 0.15] as shown in fig.3.8(b). It lies at the lower end of the theoretic estimations, close to the octave jump which may be dictated by an attempt to have a rich sound without overblowing. The increment on U_j with increasing frequency is also compensated by changing the lip opening surface, resulting in a decreasing of the total jet flow as shown in fig.3.8(a).

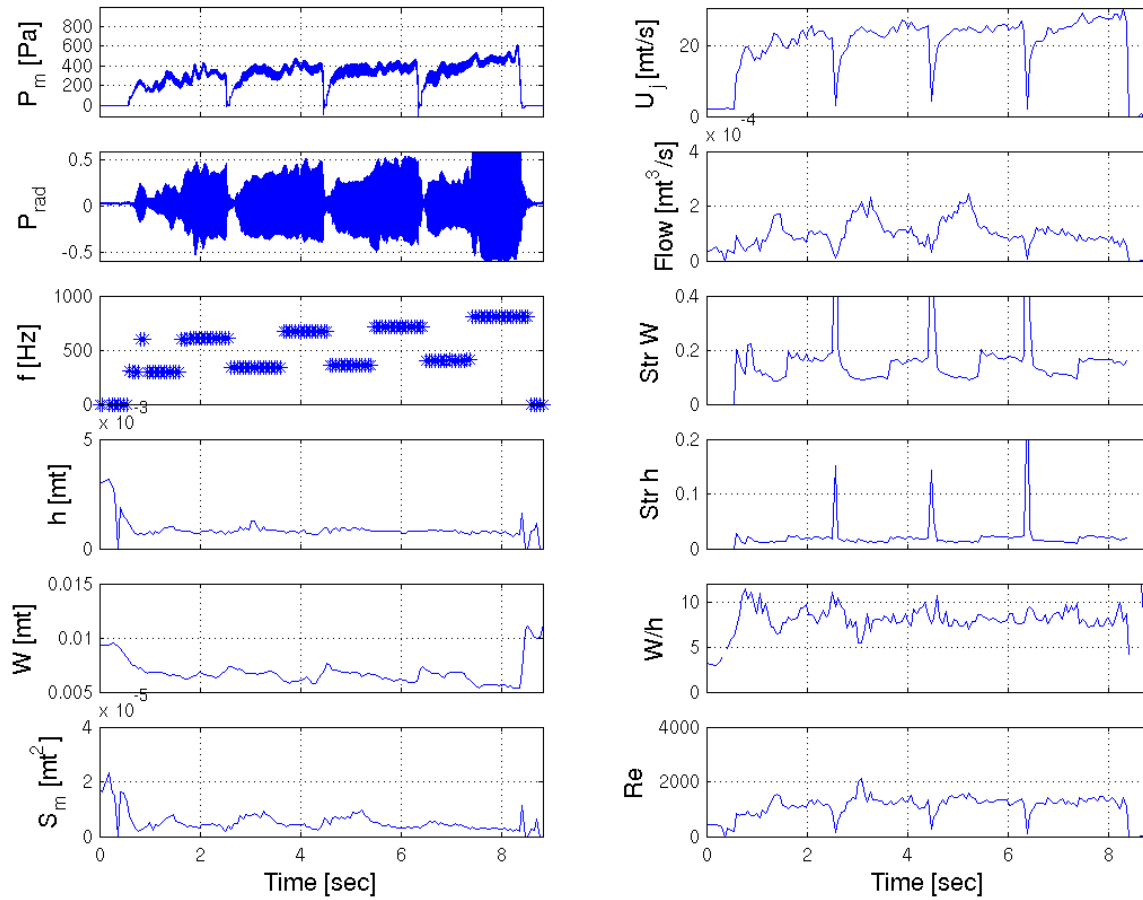


Figure 3.6: Parameters measured and calculated for the experienced player F_A playing octave intervals : D3-D4 ; E3-E4 ; F3-F4 ; G3-G4 with medium dynamics (mf)

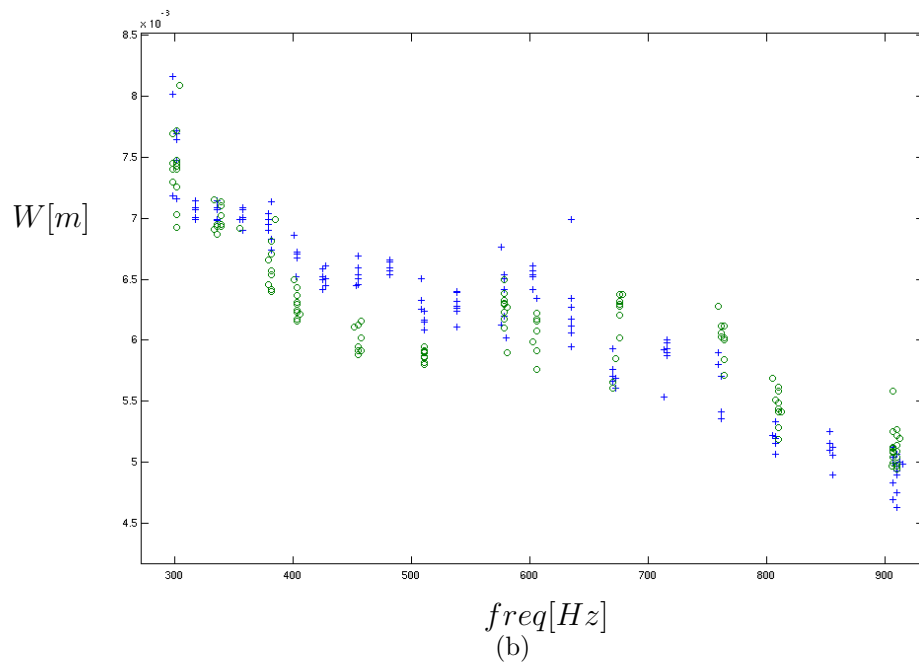
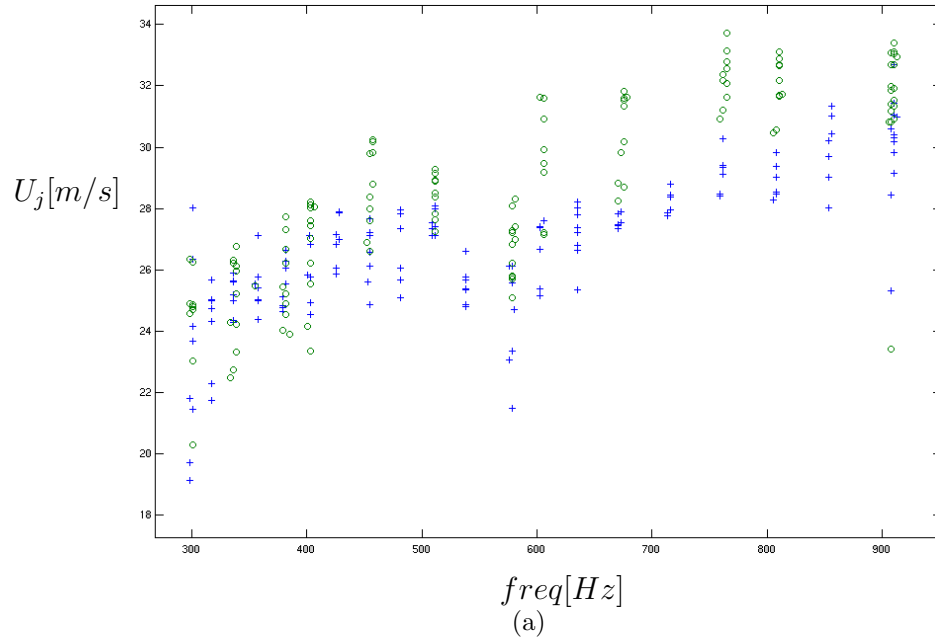


Figure 3.7: Global dependency between a) Jet velocity U_j and b) Jet length W with the frequency played. Ascending chromatic scale (+) and diatonic scale (o)

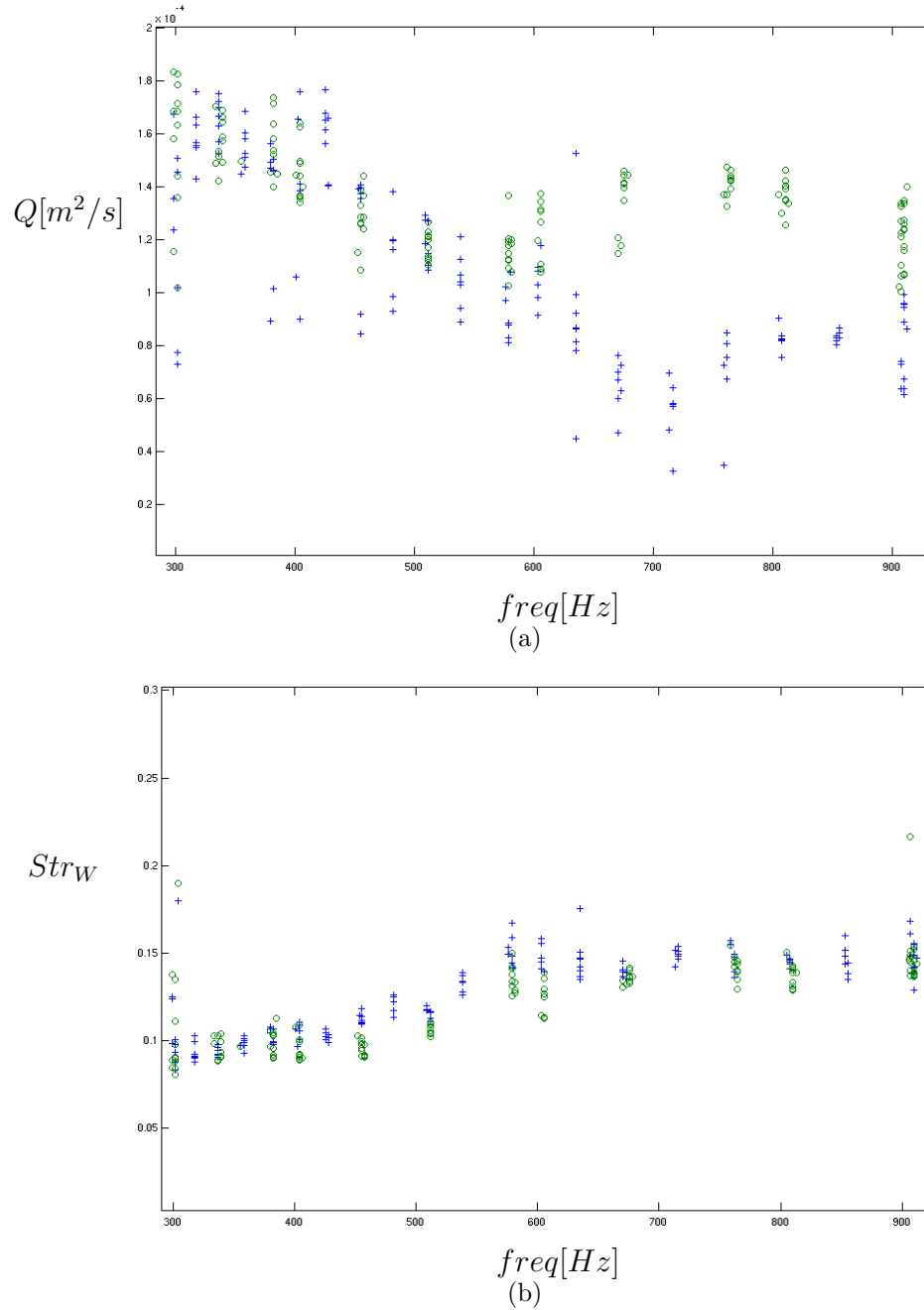


Figure 3.8: Global dependency between a) Flow Q and b) Str_w with the frequency played. Ascending chromatic scale (+) and diatonic scale (o)

3.6. COMPARISON BETWEEN A NOVICE AND AN EXPERIENCED FLAUTIST65

In fig.3.9(a) several musical excerpts have been collapsed in one plot showing the shape of Re as function of W/h . It is observed that range of operation of W/h mainly goes from 4 to 10, which coincides with the observations made in section 3.2, while most of the data is below $Re = 2500$ where the jet is laminar. Thus for laminar jets the trajectory of data as frequency or loudness grows seems to increase linearly approximately following:

$$3500 = Re + 250W/h \quad \text{for} \quad \begin{cases} 1000 \leq Re \leq 2500 \\ 4 \leq W/h \leq 10 \end{cases}, \quad (3.5)$$

As the jet becomes turbulent, for Re greater than 2500, the slope of the trajectory changes in such a way that less reduction of W/h is required to follow the increment on Re .

Fig.3.9(b) shows the Strouhal numbers Str_h and Str_W for the same set of musical excerpts. The data is observed to collapse into a small, well-defined region, bounded by $0.07 \leq Str_W \leq 0.3$ and $0.005 \leq Str_h \leq 0.035$. Furthermore, both variables seem to increase as the pitch raises or the loudness is increased, roughly following the trajectory described by:

$$Str_h = 0.2Str_W - 0.01 \quad \text{for} \quad \begin{cases} 0.07 \leq Str_W \leq 0.3 \\ 0.005 \leq Str_h \leq 0.035 \end{cases}, \quad (3.6)$$

3.6 Comparison between a novice and an experienced flautist

Our second subject (F_B) is a self-trained flautist who at the time of the experiment had been playing the flute for only four months. He has no classical musical education but shows great interest in music. He was requested to play only simple intervals due to his limited flute skills.

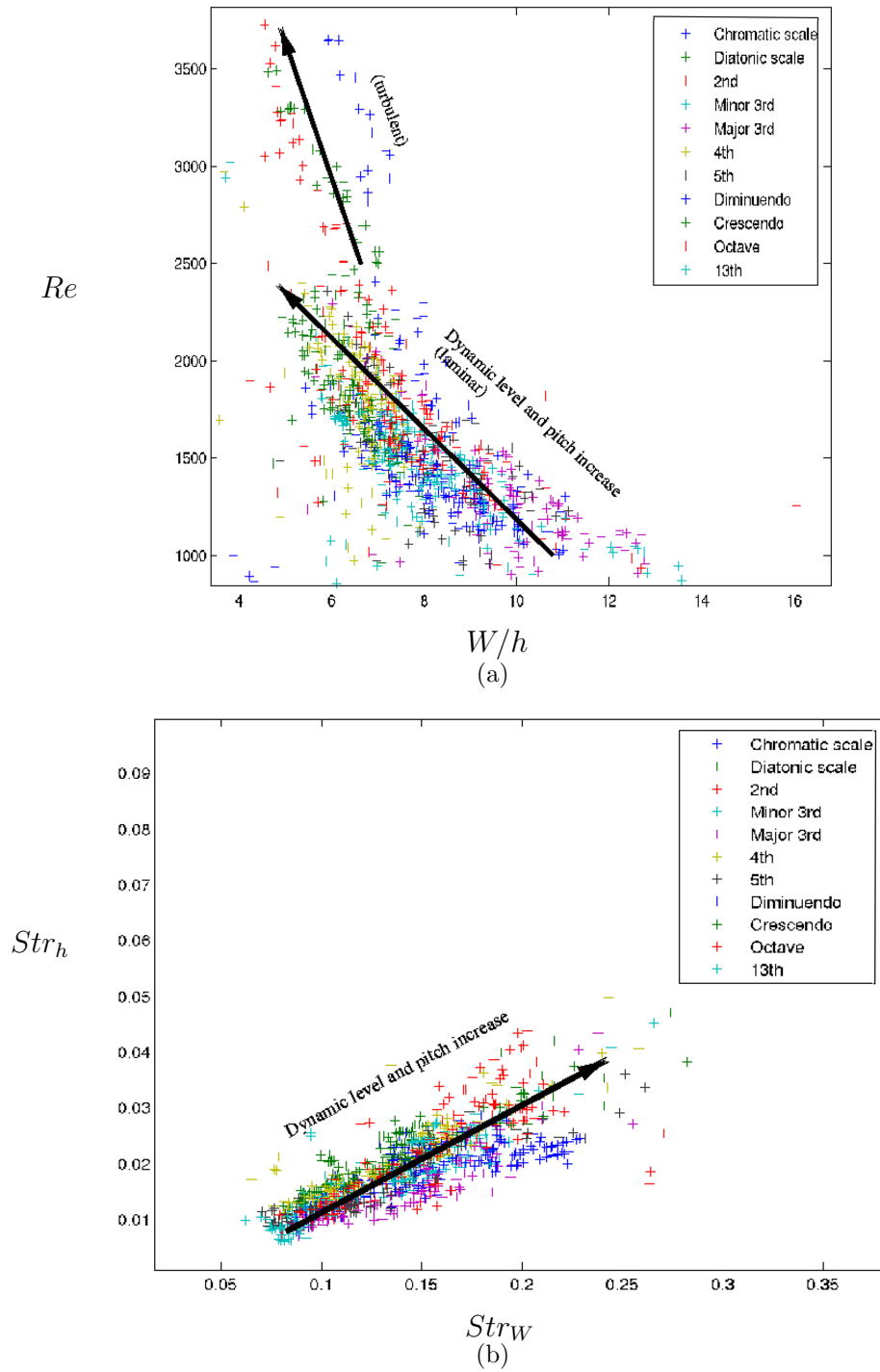


Figure 3.9: Collapsed data from several musical excerpts. a) Re vs. W/h b) Str_h vs. Str_w

3.6.1 Sound production

Fig.3.10(a), compares the jet velocities measured from F_A and F_B playing intervals of octaves. F_B shows lower jet velocity on low notes and higher jet velocity on high notes than F_A , resulting in an average increment of 60% per octave for F_B and only 10% per octave for F_A .

Although W decreases with frequency for both players (fig.3.10(b)), F_B requires a longer W to compensate the high U_j , giving more room for turbulence to develop and adding noise to his sound. Yet, the resulting Str_W remains in the range [0.08-0.3] (fig.3.11) which seems to be a necessary condition to produce a flute sound.

3.6.2 Control of the sound quality

Because of the high U_j and the lack of control over the shape of the lips hole, F_B uses a much bigger lips hole surface (fig.3.12(a)) and amount of air to produce his sound, which results in higher values of the total jet flow (fig.3.12(b)). For example on E3, the total jet flow used by F_A is approximately 0.6 *liters/s* and for F_B is 0.2 *liters/s*. If we consider a respiratory capacity of 4.8 liters (average value for a 70 kg. male [56]), F_B can hold that note for 8 seconds while F_A can do it for 24 seconds.

The increase in total jet flow affects the Reynolds number, which for F_B has an average value of 3000 and maximum up to 7000. F_A keeps the values of Re in a small and well defined region below the transition limit to turbulent and below F_B , who spreads data over a much wider region. Which means that F_B is putting more energy into producing his sound and his jet can more easily become turbulent producing a noisy sound. When turbulences are triggered before the jet reaches the labium, the jet velocity slows down rapidly, asking for even more blowing pressure from the player to maintain the oscillations.

The efficiency of the sound production is also compared. First, an upper bound of the sound power radiated P_{rad} is estimated from the microphone placed outside the instrument at a distance r . Using a free field monopole approximation:

$$P_{rad} \leq \frac{1}{T} \int_T \frac{|p(r)|^2}{\rho_0 c} 4\pi r^2 dt \quad (3.7)$$

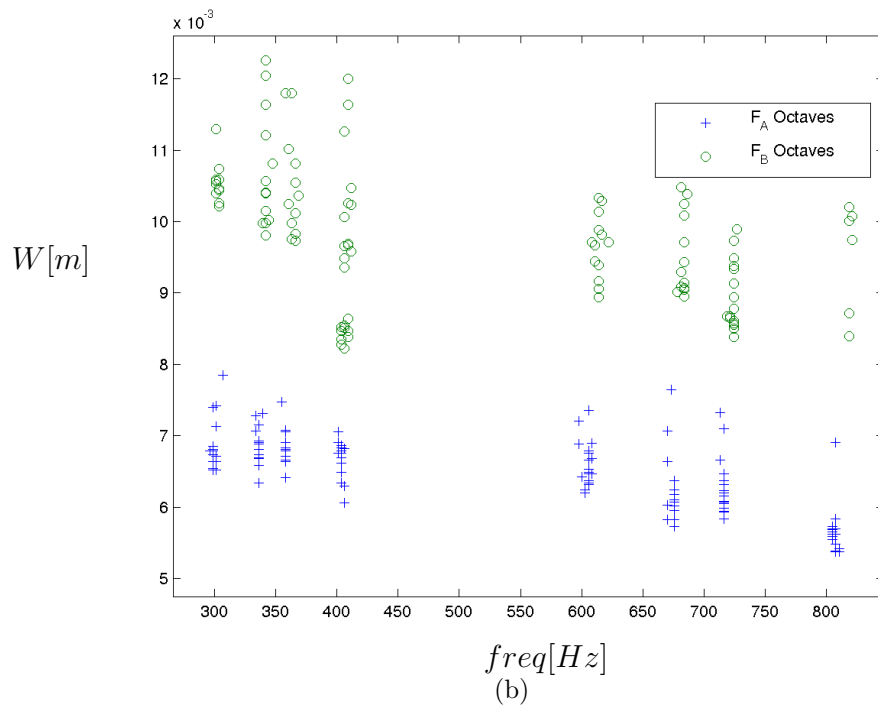
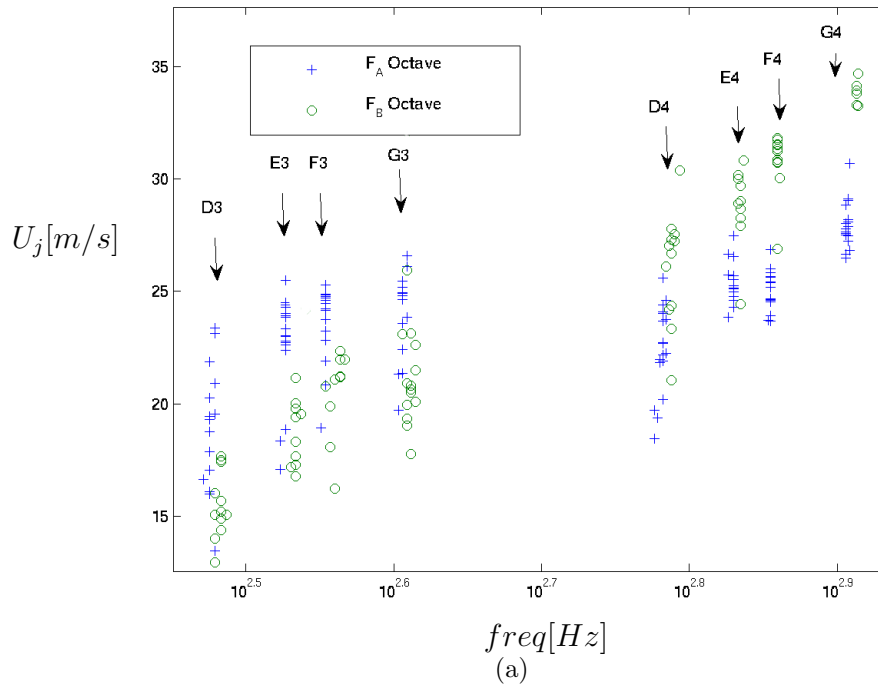


Figure 3.10: a) Jet velocity U_j and b) Jet length W as functions of frequency. Octave series, experienced flautist (+), novice (o)

3.6. COMPARISON BETWEEN A NOVICE AND AN EXPERIENCED FLAUTIST69

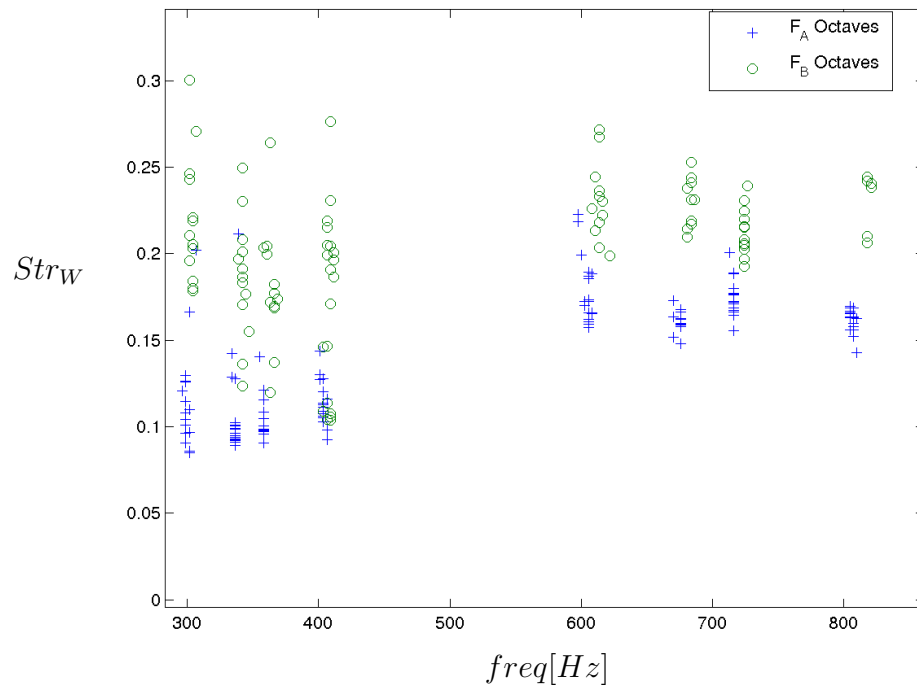


Figure 3.11: Str_W as function of frequency. Octave series, experienced flautist (+), novice (o)

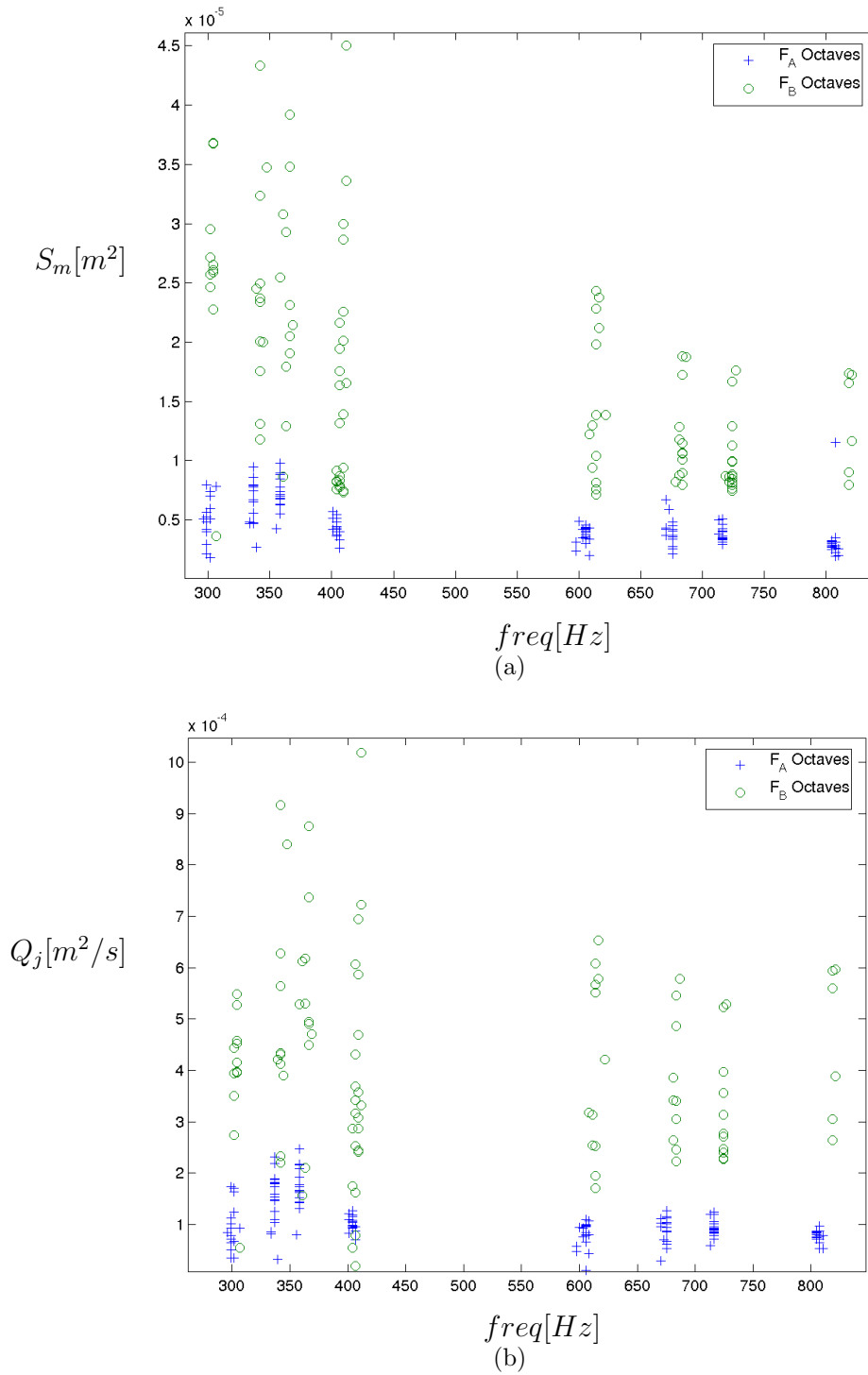


Figure 3.12: a) Lips surface S_m and b) Flow Q_j as function of frequency. Octave series, experienced flautist (+), novice (o)

3.6. COMPARISON BETWEEN A NOVICE AND AN EXPERIENCED FLAUTIST71

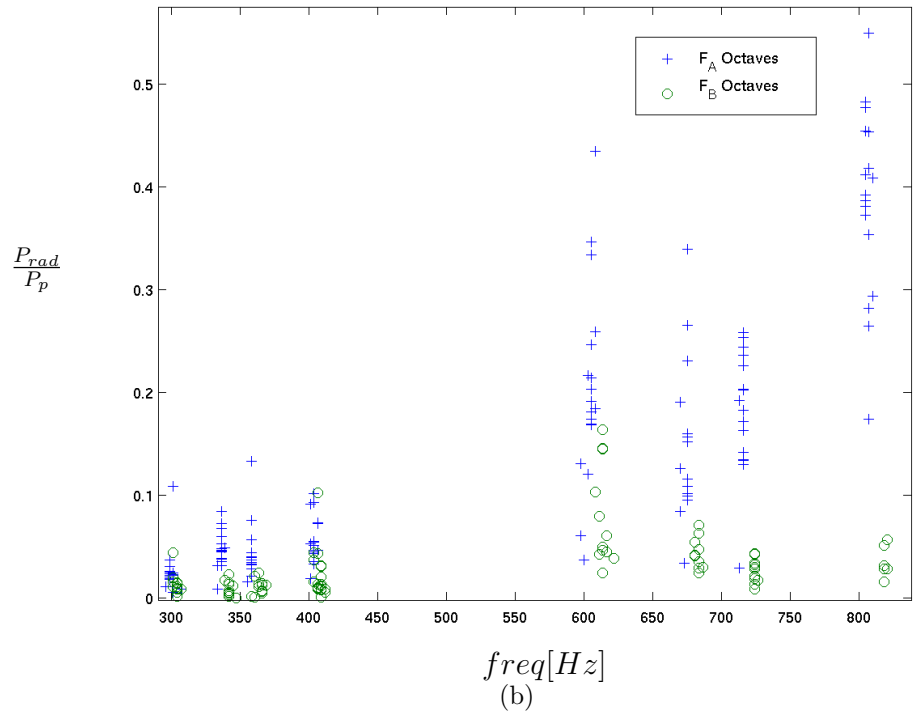
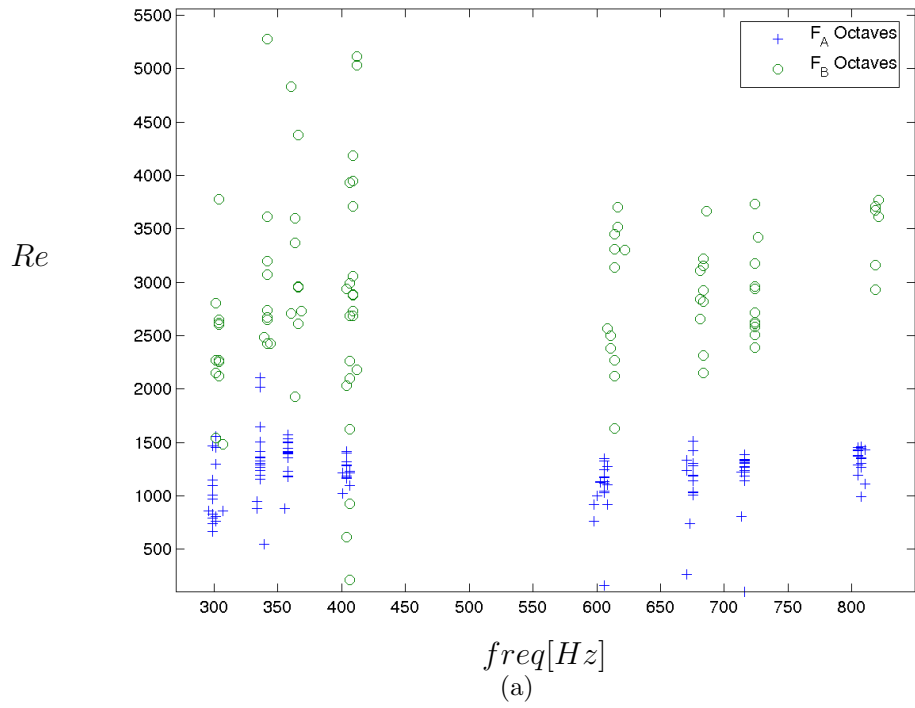


Figure 3.13: a) Re and b) Radiated power over power of the jet flow $\frac{P_{rad}}{P_p}$ as function of frequency. Octave series, experienced flautist (+), novice (o)

where $p(r)$ is the radiated pressure, T the period of oscillations and c the speed of sound in the air.

The power of the jet flow P_p is estimated as

$$P_p = \frac{1}{T} \int_T S_m U_j P_m dt \quad (3.8)$$

Finally, the upper bound η of the efficiency estimated as $\eta = \frac{P_{rad}}{P_p}$ is presented in fig.3.13(b). It's observed that the two groups are inverted. Therefore, F_A is achieving a more efficient use of the available resources and F_B 's poorer showing might be attributed to non-optimal transverse dimensions of the jet compared to the dimensions of the sound hole of the flute or the fast dissipation of energy due to turbulence and the increased jet spreading associated with it.

Coupling between the instrument and the performer's mouth cavity has been observed. Fig 3.14 shows the ratio p'_m/P_m displayed as a function of frequency for F_A and F_B playing intervals of octaves. This ratio is much bigger in F_A than F_B and decreases with frequency. p'_m can induce varicose modes in the jet that could have been utilized by F_A to influence his tone. At the same time, p'_m excites the head of the musician adding another possible source of resonance. The real influence of the observed coupling on the resulting sound remains to be studied in more detail.

3.7 Discussion

Simultaneous pressure and geometry measurements allow estimations of the principal parameters suggested by the theory presented above in section 3.2: Str_W, Str_h, Re .

It has been observed that the basic operation of the flute requires Str_W to be close to 0.20 regardless of the quality of the sound produced. A clear and noiseless sound, which is normally requested for playing traditional repertoire in the flute, is achieved by keeping Re controlled and below its transition threshold for turbulence. Efficiency and control over the flute timbre requires coordinated control over several parameters, where the coordination among W , U_j and h are particularly important. This coordination is not intuitive and requires assimilation through training.

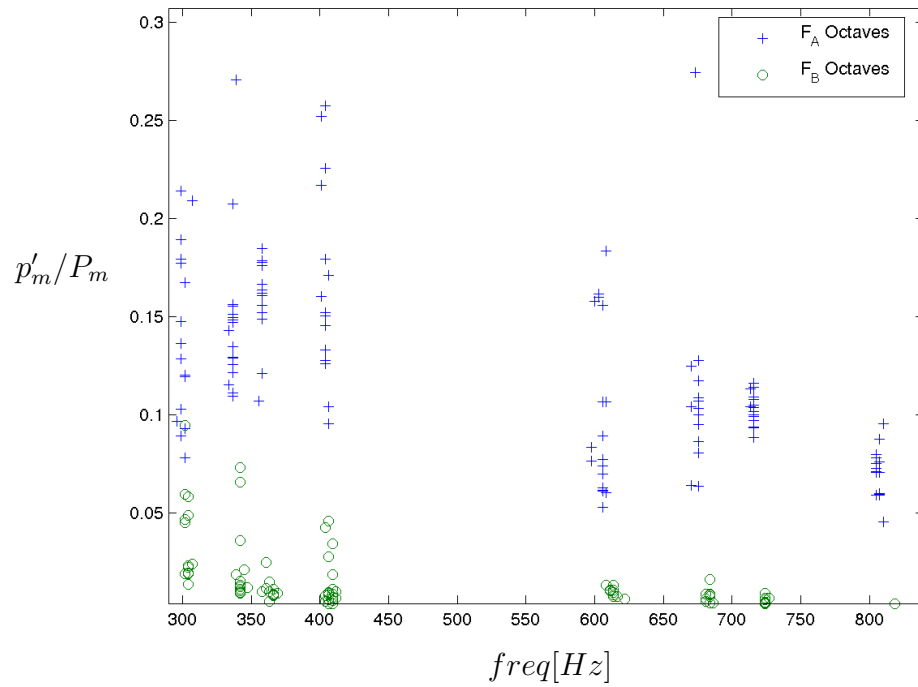


Figure 3.14: Acoustic pressure inside the mouth. Octave series, experienced flautist (+), novice (o)

	min	max
Str_W	0.07	0.35
Str_h	0.005	0.035
W/h	2	10
Re	-	2500

Table 3.1: ranges for measured non-dimensional values

Since the maximum amplification of the jet perturbation occurs for $Str_h \approx 0.025$ it is expected that a trained flautist will adjust the control parameters to approach that value and achieve good efficiency. Both Str_W and Str_h are observed to remain stable to keep the timbre homogeneous. Nevertheless, some flexibility is desired in order to obtain timbrale variations and a wide dynamic range from the instrument.

In table 3.1, a range of parameters for laminar operation of the instrument is shown, which together with the trajectories described in section 3.5.2 can be used as starting values for synthesis with linear physical models.

The shape of the lips holes in our two subjects is very different. Although this could have an influence on the sound, a trained flautist can optimize the behavior of his jet and produce a beautiful sound regardless of the shape of his or her lips [44]. Good control over the flow helps keep the timbre homogeneous throughout the register of the instrument.

As discussed in section 3.5.2 and also pointed out by Fletcher [35], changes in frequency are accompanied by comparatively small changes in the jet velocity. This strategy may have a kinesthaetic explanation: an instrument capable of playing fast melodies needs to keep some independence between P_m and the frequency played. Muscles controlling the pressure such as the diaphragm and chest muscles, are comparatively much slower than melodies played by flutes. A way to achieve this economy in the P_m variations is to 'overplay' the lower register and underplay the higher. That is, playing low notes at frequencies slightly higher than the passive resonances and high notes slightly lower than the passive resonances, thus putting both registers closer.

Although an extensive set of measurements has been studied, a complete description of the mechanisms utilized by the flautist to control their instrument can only

come from a study with several subjects. We have presented findings based on two subjects in attempt to understand the range of interactions and lay the groundwork for a wider study of these phenomena which are basic to flute performance.

Chapter 4

A physical model and experimental testbed for real-time simulation of flute-like instruments

Abstract

In the last decades, a wealth of experimental data has been gathered concerning sound production in flute-like instruments. These data have driven the development and fine tuning of analytical models for the physical processes involved. Here, a number of these results are integrated into a real-time physical model of a flute-like instrument. The model proposed is one-dimensional and driven by a single input pressure.

4.1 Introduction

With the improvement of computers in the last decades of the 20th century there was a renewed interest in modeling musical instruments. One of the first flute physical models was proposed in 1988 by McIntyre et. al [59]. In his model the relation between the control parameters and the physical variables of the instrument were obscure. Therefore its flexibility and range of sound possibilities were very limited. Despite its limitations it served as motivation for searching better solutions [18].

After a more detailed study of the physics of flutes, Verge [87] proposed a model for an organ pipe that greatly expanded the possibilities of the generated sound. Since then there have been years of experimentation and refinement of the model elements. Some of them are collected here and put together in a model of a flute-like instrument capable of real-time operation and flexible enough to morph among various types of flute geometries and operation conditions.

The time domain model proposed here deals entirely with pressures in the system, and remains valid only for the linear behavior of flutes, i.e. for low Reynolds number and relatively small amplitudes of operation. The model is split in two parts, the resonator detailed in section 4.2 and the excitation described in section 4.3.

4.2 Resonator

The resonator is modeled from the geometry of the European transverse flute, which consists of three connected tubes: a bore, a chimney leading to the open end, and an upper cavity (fig. 4.1).

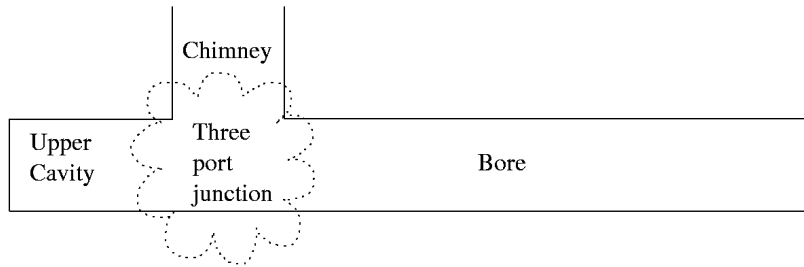


Figure 4.1: Resonator from a transverse type flute

Wavefronts are assumed planar inside the resonator, and the one-dimensional wave equation is used to model wave propagation.

$$\frac{1}{c_0^2} \frac{\partial^2 p_p}{\partial t^2} - \frac{\partial^2 p_p}{\partial x^2} = 0 \quad (4.1)$$

D'Alembert's solution of this equation enables one to represent the resulting pressure signal p_p as the sum of two traveling waves p_o and p_i ,

$$p_p = p_o(x - c_0t) + p_i(x + c_0t), \quad (4.2)$$

and permits implementation using digital waveguide techniques [78].

The three tubes in the resonator are connected in the model through a three-port junction in which pressure equilibrium and flow conservation are obeyed. An optimized implementation is used [74] in which only one multiplication per input sample is necessary to connect the three ports.

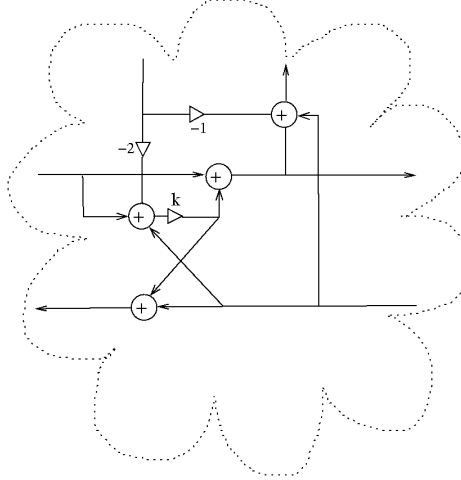


Figure 4.2: Optimized implementation for a three-port junction

Where k is expressed in terms of the radius of the tube sections as:

$$k = \frac{-r_{chimney}^2}{r_{chimney}^2 - 2r_{cavity}^2} \quad (4.3)$$

4.2.1 Visco-thermal Losses

The effects of viscosity and thermal conduction of sound in cylinders are much greater than for propagation in free space because of the boundary conditions imposed by the cylinder walls. Visco-thermal damping induces a frequency-dependent dispersion and exponential decay of traveling waves. Its effects can be represented, in the frequency

domain, by the use of a complex wave number k [68].

$$p_p = (p_0 e^{-ikx} + p_1 e^{ikx}) e^{i\omega t} \quad (4.4)$$

where,

$$k = \frac{\omega}{c} + (1 - i)\alpha_{wall} \quad (4.5)$$

The value of α_{wall} is approximated for a wide cylinder, large enough for the boundary layers to occupy a very small fraction of the cylinder's cross-sectional area, as:

$$\alpha_{wall} \approx \frac{\sqrt{2\nu\omega}}{ca} \left[1 + \frac{\gamma - 1}{\sqrt{Pr}} \right] \quad (4.6)$$

where ν is the air kinetic viscosity, c the speed of sound in the air, γ the specific-heat ratio, and Pr the Prandtl number. Only the dispersive component needs to be modeled since the pure delay can be added to the resonator delay line.

$$H_{disp} = e^{-(1+i)\alpha_{wall}L}, \quad (4.7)$$

where L is the length of the tube. Fig.4.3 shows the frequency response of the visco-thermal losses for a 60 cm bore and 9 mm radius.

4.2.2 Radiation and reflection from the end of the bore

Most of the radiated sound exits from the open ends of the the resonator. Though depending on the size of the toneholes and the fingering of a note, an important amount of energy can be radiated through the toneholes.

Toneholes can be modeled using three-port junctions and fractional delays [74, 88] which adds complexity to the frequency response of the model's feedback loop. For the sake of simplicity a sliding-flute approach has been chosen in which the pitch of the note is changed by adjusting the length of the resonator and the instrument radiates only from its open ends.

The radiation impedance at the end of the bore \mathbf{Z}_r can be approximated by that of a circular piston of radius a . The impedance is calculated as a ratio between the

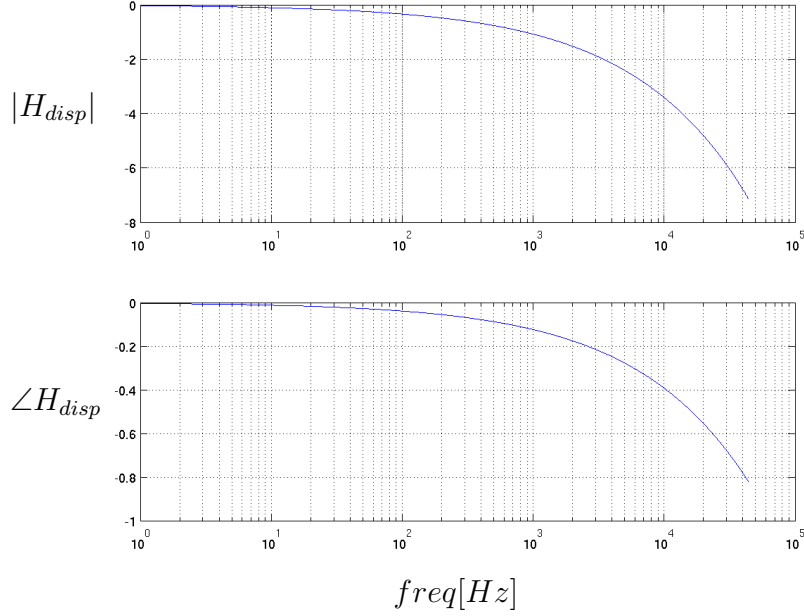


Figure 4.3: Visco-thermal losses for a 60 cm cylinder with 9 mm radius.

pressure and velocity radiated [50].

$$\mathbf{Z}_r = \frac{\rho_0 c}{S} [R_r(2ka) + jX_r(2ka)] \quad (4.8)$$

where $S = \pi a^2$ is the area of the piston face, ρ_0 the air density and c the sound speed in the air.

The radiation resistance R_r and reactance X_r are given by

$$R_r(x) = 1 - \frac{2J_1(x)}{x} = \frac{x^2}{2 \cdot 4} - \frac{x^4}{2 \cdot 4^2 \cdot 6} + \frac{x^6}{2 \cdot 4^2 \cdot 6^2 \cdot 8} - \dots \quad (4.9)$$

$$X_r(x) = \frac{2\mathbf{H}_1(x)}{x} = \frac{4}{\pi} \left(\frac{x}{3} - \frac{x^3}{3^2 \cdot 5} + \frac{x^5}{3^2 \cdot 5^2 \cdot 7} - \dots \right)$$

Where J_1 and \mathbf{H}_1 are the first order Bessel function and the Struve function respectively.

In the low-frequency limit ($ka \ll 1$) the piston resistance function R_r and reactance function X_r can be approximated by the first terms.

$$R_r \approx \frac{1}{2} \rho_0 c S (ka)^2 \quad (4.10)$$

$$X_r \approx \frac{8}{3\pi} \rho_0 c S k a \quad (4.11)$$

The reflection coefficient Γ at the end of the tube can be implemented as a filter applied to the incident pressure p_0 producing the reflected pressure p_i , where

$$\Gamma = \frac{Z_r - 1}{Z_r + 1}. \quad (4.12)$$

This coefficient is shown in fig.4.4.

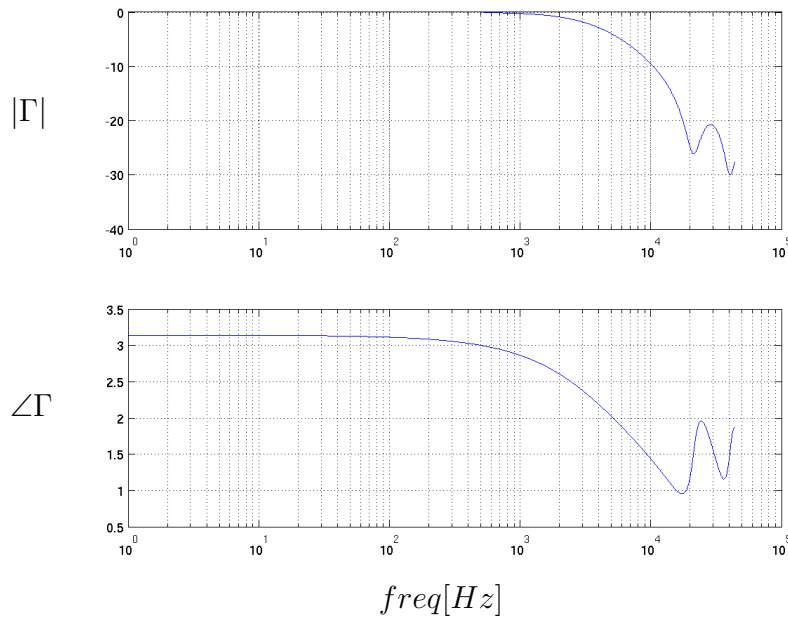


Figure 4.4: Reflection coefficient for a cylinder of radius = 9 mm

4.2.3 Frequency range

The assumption of plane waves traveling inside the resonator is reasonable only for wavelengths larger than the diameter of the tube $\lambda > a$. Below that, transversal propagations of waves can also be expected. For a diameter of $a = 2\text{cm}$ the frequency upper boundary is:

$$f < \frac{c}{a} \approx 17\text{kHz} \quad (4.13)$$

On the lower end of the spectrum, the assumption of wide cylinder made to estimate the visco-thermal losses is valid when the acoustic boundary layer is relatively small with respect to the diameter of the cylinder $\delta \ll a$.

$$\frac{\sqrt{\nu}}{2a} \ll 10^{-2} \quad (4.14)$$

where ν is the kinematic viscosity of the air. Thus, under the current assumptions the range of frequencies valid model is,

$$30\text{Hz} \ll f < 17\text{kHz} \quad (4.15)$$

In this range of frequencies both reflection and losses filter can be easily approximated using second order digital filters, which for real-time application gives a good compromise between speed and accuracy [49].

Visco-thermal losses dominates in the low frequencies corresponding to the first modes of the bore. Damping produced by the reflection at the end of the bore becomes more important as frequency grows, as can be observed in fig.4.5.

4.2.4 Parametric implementation

The reflection filter can be made parametric with respect to the radius of the bore a , so that it can be adjusted in real time without re-calculating the coefficient of the filters. The following transformation for the unit delay is utilized [65]:

$$T(z) = \frac{\lambda - z^{-1}}{1 - \lambda z^{-1}} \quad (4.16)$$

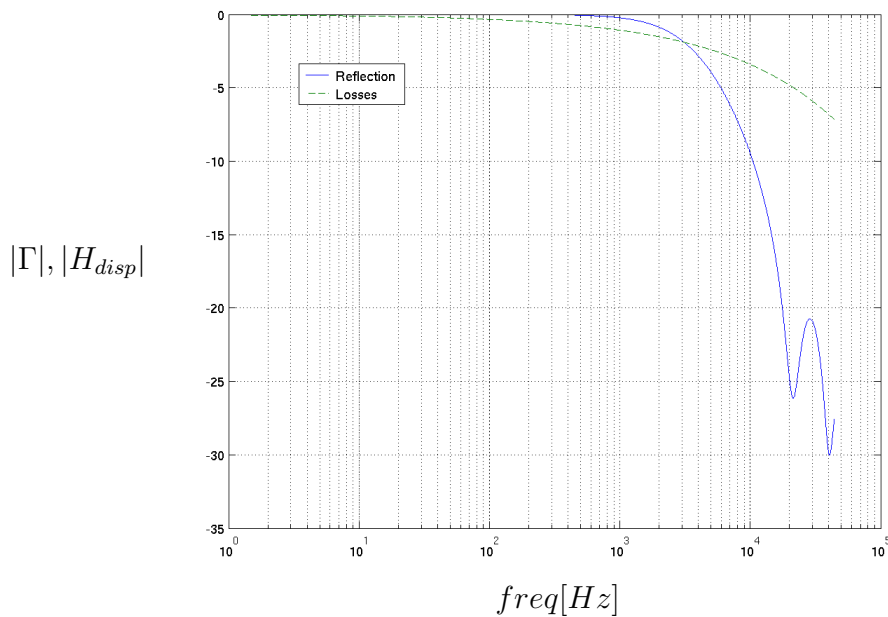


Figure 4.5: Comparison between reflection and visco-thermal losses for a cylinder of 9mm radius and 60 cm length

with,

$$\lambda = \frac{a_{ref} - a}{a_{ref} + a} \quad (4.17)$$

where a_{ref} is the reference or central radius value. Fig.4.6 shows a comparison between the theoretical values calculated with eq.4.12 for a radius $r = 9mm$ and variations of 20% above and below that value, and the response obtained with the transformation of eq.4.16 for the same values of the radius.

We observe a reasonable good approximation to the real theoretical curve for low frequencies with the advantage that the filter coefficients are not re-calculated in a real-time application.

4.2.5 Signal flow diagram

A schematic for the connections of the resonator elements: the three tubes, the radiation and losses, inputs and outputs, are displayed in fig.4.7. Pressure sources are injected at the embouchure, they propagate through the three-tubes resonator with

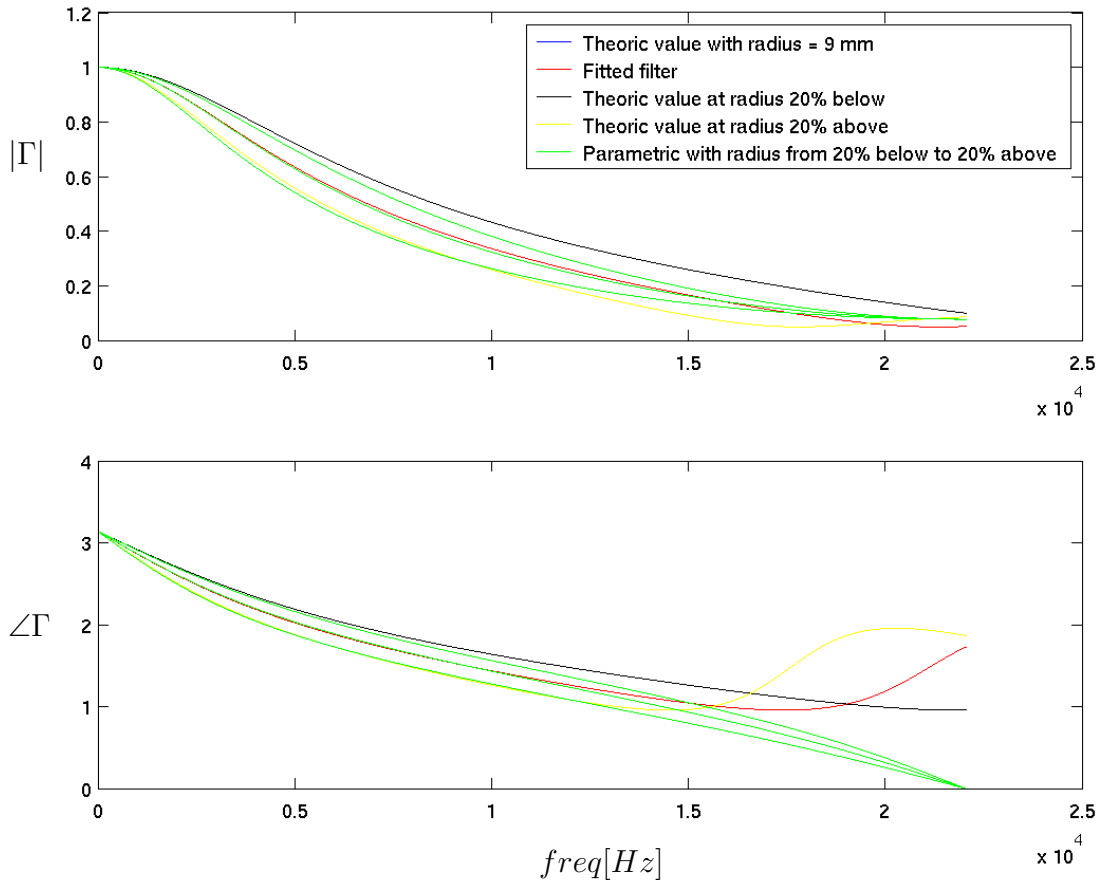


Figure 4.6: Reflection frequency response obtained by varying the parameter a

their losses and reflections, and come back to be produce the mouth pressure P_p and acoustic velocity V_{ac} .

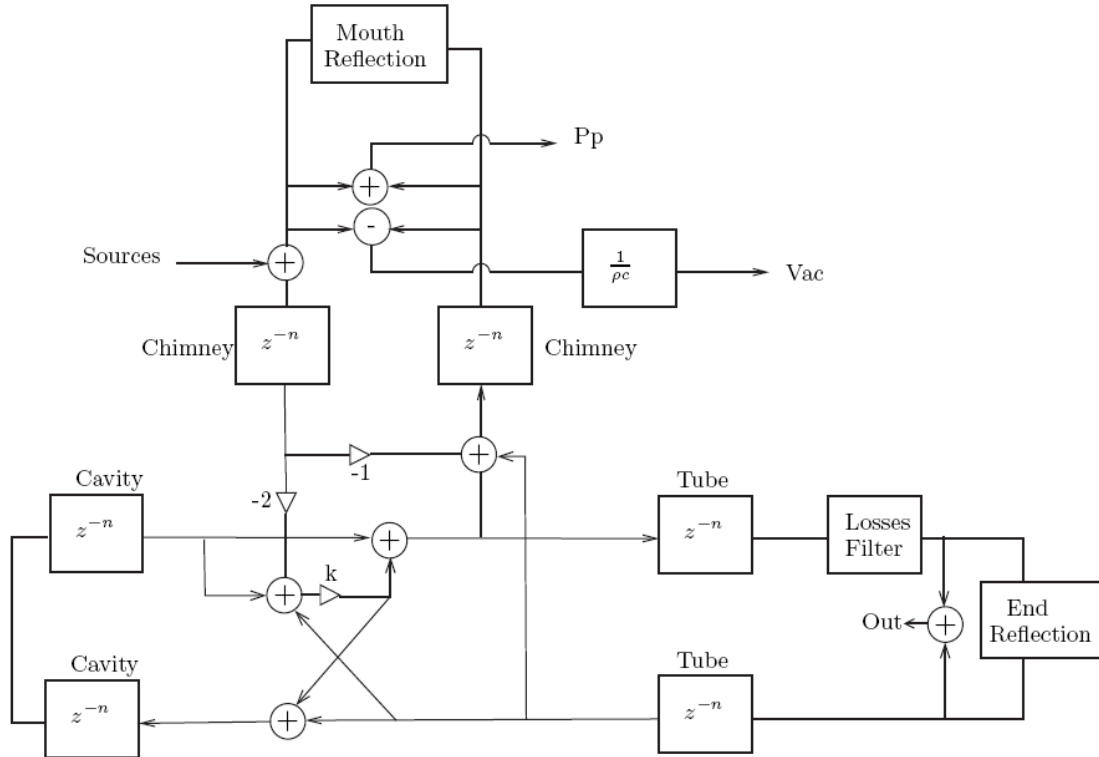


Figure 4.7: Block diagram of the flute model resonator

The output signals can be read at both open ends of the resonator by adding the traveling waves and an estimation of the acoustic velocity V_{ac} at the mouth of the instrument is obtained as:

$$V_{ac} = \frac{p_0 - p_1}{\rho c}. \quad (4.18)$$

4.2.6 Input impedance

The influence of the three-tubes geometry of the flute in the input impedance has been described by Benade [5], while Coltman [15] studied the influence of the conicity of the flute headjoint in the non-harmonicity of the impedance. Wolfe [89] measured the impedance for several combinations of fingerings. The input impedance of our model

has been determined by measuring pressure and acoustic velocity while feeding the system with a pressure impulse. The results are shown in fig.4.8.

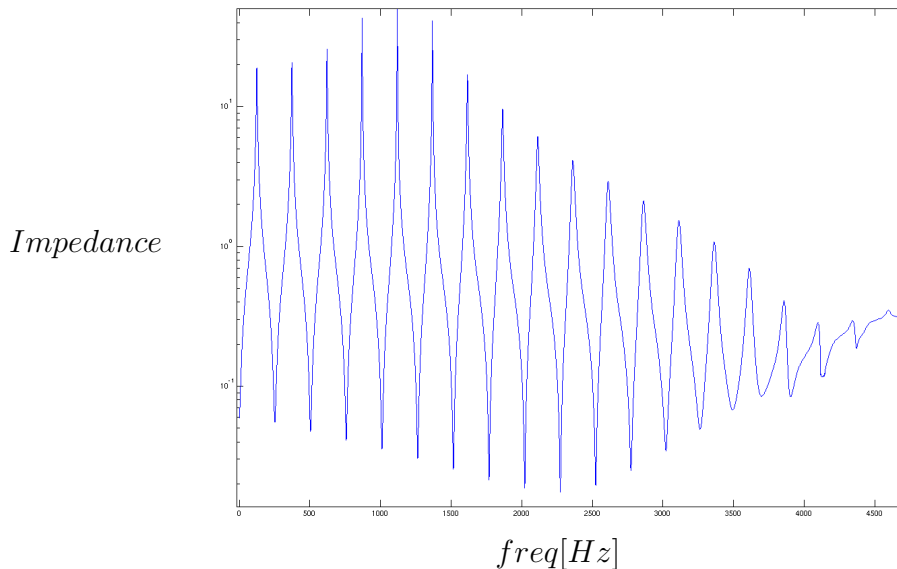


Figure 4.8: Input impedance of the three-tubes resonator model

A perfect cylinder without losses would create a periodic impedance with minima located in multiples of the fundamental. The complexity added by the three tubes, losses and reflection filter creates a shape where minima depths decreases at high frequencies and become less sharp. The dispersion slightly moves the minima from their harmonic locations.

4.3 Excitation

An intrinsically unstable air jet is responsible for injecting the necessary energy to maintain the oscillations. The geometry of an organ pipe (fig.4.9) is used to describe the elements involved in the excitation: formation channel, mouth, jet and labium. Its geometry is general enough to give adequate description for most flutes, including those played with the lips where the geometry is not fixed but adjusted continuously by the player.

The air jet exits the formation channel and crosses an open space before hitting a sharp edge called the labium. On its way it is perturbed by the air particles oscillating at the open end of the resonator, called the mouth of the instrument.

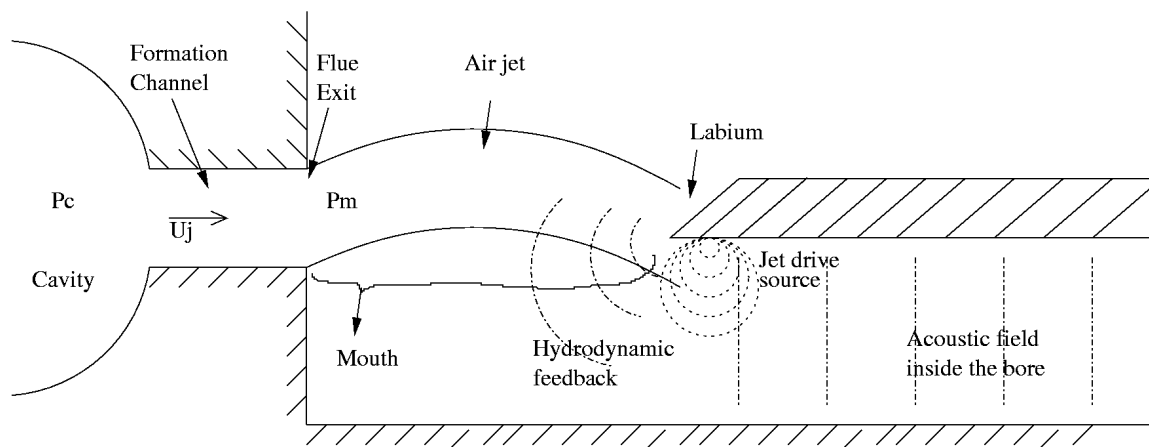


Figure 4.9: Organ pipe geometry.

In this section the formation of the jet is analyzed along with the mechanism used to trigger the initial oscillations. Then we describe the jet interaction with the resonator in terms of three processes: *receptivity*, *instability* and *sources*.

4.3.1 Attacks

Before oscillations have been established in the resonator, the jet coming out from the channel injects a pressure jump that is responsible for triggering the oscillations. To calculate this jump, a simplified estimation of the acoustic impedance at the mouth of the instrument is proposed.

Without the acoustic field at the flue exit, the jet coming out from the channel only sees an impedance that is formed by the combination in parallel of two elements: impedance from the resonator Z_r and mouth impedance Z_m . In a one-dimensional model impedances can be represented by small tubes (fig.4.10) whose lengths are chosen to preserve the magnitude of the impedance.

$$Z_r = i\rho c \tan(kL_r) \simeq i\omega\rho L_r \quad \text{if } kL_r \ll 1, \quad (4.19)$$

$$Z_m = i\rho c \tan(kL_m) \simeq i\omega\rho L_m \quad \text{if } kL_m \ll 1, \quad (4.20)$$

where L_r and L_m are the effective lengths of the resonator and the mouth impedance (or end correction) respectively.

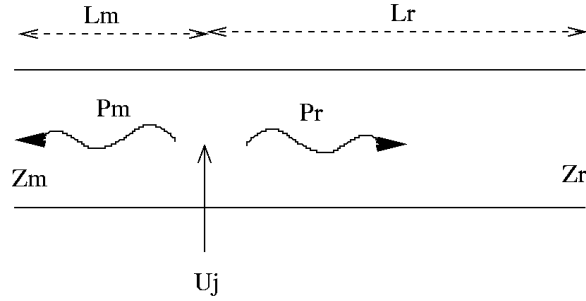


Figure 4.10: One-dimensional models for the impedance seen by the jet at the flue exit

The total impedance Z_t is the sum in parallel both impedances. Since $Z_m \ll Z_r$, $Z_t \simeq Z_m$. Thus the total pressure injected is,

$$P_t = Z_t U_j = \rho L_m \frac{dU_j}{dt}, \quad (4.21)$$

During the attack the linear term $\rho L_m \frac{dU_j}{dt}$ provides the impulse necessary to trigger the oscillations. For short times, before the first reflection has come back ($t < 2L_m/c$) a further simplification can be done. The pressure injected in each direction is equal and equivalent to half of the total injected pressure: $P_r = P_m = P_t/2$.

4.3.2 Jet formation

Pressure is raised in a cavity upstream from the formation channel (P_c in fig.4.9). On its way out the stream forms a jet whose velocity profile depends on the geometry of the formation channel. Its central velocity can be estimated using Bernoulli's

equation.

$$\rho_0 L_{eff} \frac{dU_j}{dt} + \frac{1}{2} \rho_0 U_j^2 = P_c - P_m \quad (4.22)$$

Where L_{eff} is the effective length of the formation channel as proposed by Verge [84], U_j is the jet central velocity, ρ_0 air mass density, P_c the pressure in the cavity and P_m the pressure in the mouth.

When the flute is operating in the stationary regime, P_m oscillates at the frequency of the note played, therefore U_j oscillates at that rate too. In real flutes this oscillation causes varicose modes in the jet that are not included in the model, therefore this effect is ignored almost everywhere in the model by forcing $P_m = 0$.

During the attack the linear term $\rho L_{eff} \frac{dU_j}{dt}$ dominates over the quadratic term, and is responsible for the initial rise of U_j . Later, in stationary regime the quadratic term dominates over the linear.

4.3.3 Receptivity and Instability

Receptivity refers to the jet response to a perturbation. The acoustic velocity V_{ac} seen by the jet as it emerges from the formation channel modulates its shear layers inducing a perturbation that propagates along it. V_{ac} is made out of two components: the acoustic field coming from the resonator and the hydrodynamic feedback produced by the interaction between the jet and the labium, as shown in fig.4.9.

Instability describes the way in which the perturbation propagates along the jet before hitting the labium, which under a linear model grows exponentially with a propagation velocity (c_p) and growth rate (α) that are both frequency dependent.

Fletcher [42] proposed model to describe the receptivity and instability, where an oscillating acoustic velocity V_{ac} is assumed and the displacement is calculated from it. One end of the jet is assumed to be fixed, which is equivalent to say that it responds to a negative displacement and arrangements are done to assure zero displacement at the origin.

$$\eta = \frac{V_{ac}}{i\omega} (1 - \cosh(\alpha x) e^{-i\omega(t-x/c_p)}) \quad (4.23)$$

This model was slightly modified by Verge [87] and used in his model despite the non-physical assumption used to derive it, because it fit data better than any of the available models.

There are two elements of this model that do not agree with our experiments. There is a phase difference of π between the acoustic velocity V_{ac} and the jet displacement at the origin ($\eta_{x=0}$), and there is a factor of $1/\omega$ on the jet displacement that misbehaves at low frequency. Neither of them have been observed in our measurements [23].

Alternatively we propose a simple and empirical model, that consists of an exponential growth.

$$\eta = \eta_0 e^{i(\omega t - kx)} \quad (4.24)$$

where k is complex value, $\Im\{k\} = \alpha(\omega)$ and $\Re\{k\} = \omega/c_p(\omega)$.

Phase difference between V_{ac} and η_0 has been measured to be zero, and the complex valued wave number k and η_0 are obtained from real jet measurements. An estimation of the upper boundary for η_0 is obtained by using momentum conservation in the jet, from the exit up to the vortex street formed after the linear growth [47].

The convection velocity c_p is observed to be weakly dependent on ω (fig.4.11) therefore, for simplicity, it is assumed constant to a value of 30% of the jet velocity, $c_p = 0.3U_j$. This simplification allow us to replace the factor $e^{i(x/c_p)}$ in eq.4.24 by a simple delay line.

The amplification growth rate α , can be measured [23, 64] and also theoretically estimated [57, 75] by assuming jet velocity profile and solving Rayleigh's equation for the conservation of vorticity [72]. In both cases a non-dimensional representation can be obtained, as shown in fig.4.11.

The non-dimensional description captures the complete behavior of the jet, but when observed as a filter, its frequency response changes with the variables involved. In the case of the filter describing the amplification of the jet perturbations α , the varying parameters are the jet velocity U_j and jet height h that stretch the frequency response and h also scales the amplitude of the response.

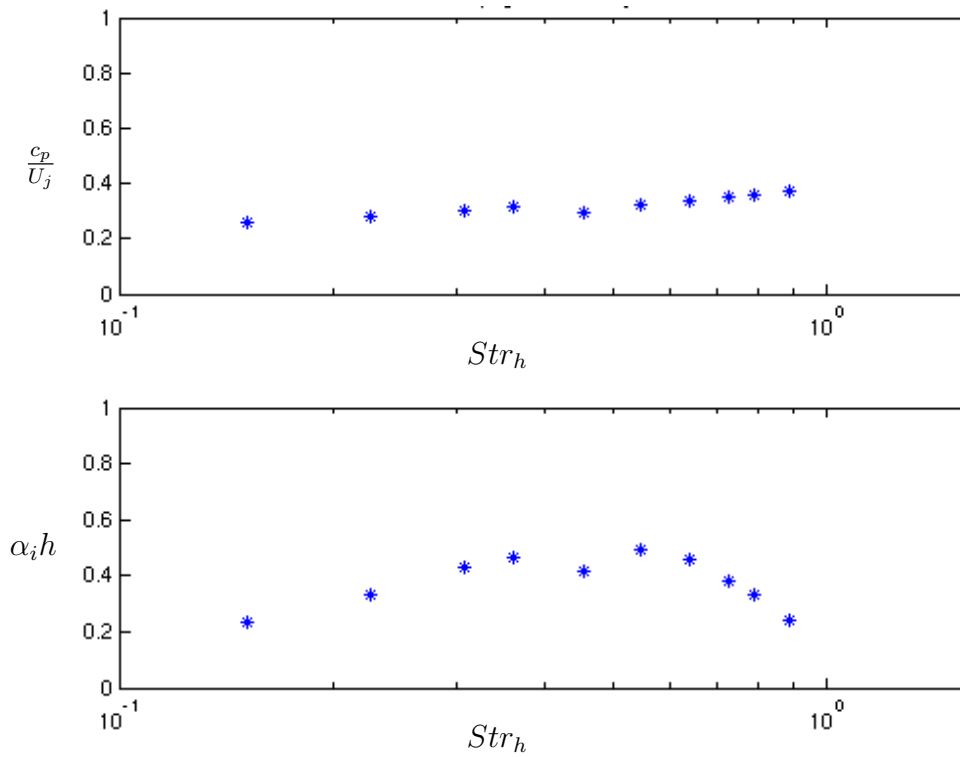


Figure 4.11: Measured values for (top) the convection velocity times jet height (αh) and (bottom) the amplification growth over jet velocity (c_p/U_j) as function of Strouhal number ($\omega h/U_j$).

So as to allow real-time implementation and parameter control, a novel time-varying jet filter has been developed which not only closely matches measured jet oscillation amplitudes as a function of jet geometry and frequency, but may be rapidly slewed in response to quickly changing performance parameters. The filter is a cascade of second-order peaking and shelving filters, as described in [1]. Such a structure enables fitting desired jet filter magnitudes via linear least-squares techniques. As the second-order sections can be made nearly self-similar on a log frequency axis and a dB amplitude scale, the cascade can be scaled and stretched around a nominal jet filter characteristic without having to recalculate the fit with each jet parameter change. A jet filter fit and scaled in this way is shown in fig.4.12.

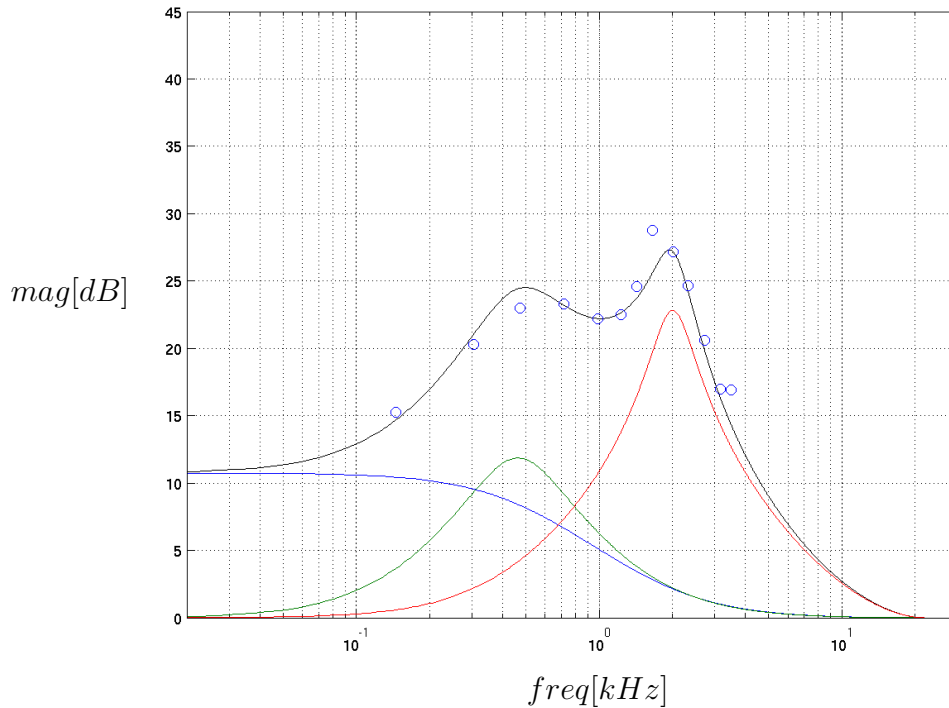


Figure 4.12: Jet filter frequency response projected in two peak and one shelf filter, for a $U_j = 20m/s$, $x = 4.5mm$ and $h = 1mm$

4.3.4 Sources

In the model, the *sources* are simplified representations that intend to capture the complex transfer of energy between the oscillating jet and the acoustic field in the resonator. For convenience they are artificially split [32] into three lumped elements: jet drive, vortices and turbulences.

The nature of the sources were first investigated by Helmholtz (1885) and Rayleigh (1894). Helmholtz viewed the jet as a volume source injecting periodically flow inside the resonator and acting as a monopole. Rayleigh realized that the jet is an unstable structure which can amplify the acoustic field from the pipe, but he argued that a flow monopole could not be efficient at producing acoustic work since it is located in the mouth of the instrument, a point of low pressure near an open end of the bore. He therefore explained the effects of the jet motion in terms of an acoustic force at the edge of the labium placed at a point of maximum jet velocity.

Jet drive

The *jet drive* refers to the transfer of energy due to the injection of flow by the jet inside and outside the resonator.

The jet velocity profile is assumed to be Bickley ($U(y) = U_0 \text{sech}^2(y/b)$), where b is a parameter proportional to the height of the jet h . The flow going inside the resonator (Q_{in}) can be calculated by integrating the jet profile up to the labium position [20]:

$$Q_{in} = \int_{-\infty}^{(\eta-y_0)} U j(y) dy, \quad (4.25)$$

$$Q_{in} = bHU_0 \left(1 + \tanh \left(\frac{\eta - y_0}{b} \right) \right). \quad (4.26)$$

where y_0 is the position of the jet with respect to the vertical center of the formation channel and H the jet width.

The velocity profile has an important incidence in the quality of the sound generated. Its shape depends on the geometry of the formation channel and it gets smoother as it travels away from the flue exit.

To control small variations to its shape, a simple transformation that changes the slope of the profile keeping total flow constant is proposed,

$$Q_{in} = bHU_0 \left(1 + \tanh \left(\frac{\eta - y_0}{\psi b} \right) \right), \quad (4.27)$$

where ψ is a parameter that can be controlled in real time and represents how spread the jet is when reaching the labium. It makes changes in the slope of \tanh as shown if fig.4.13.

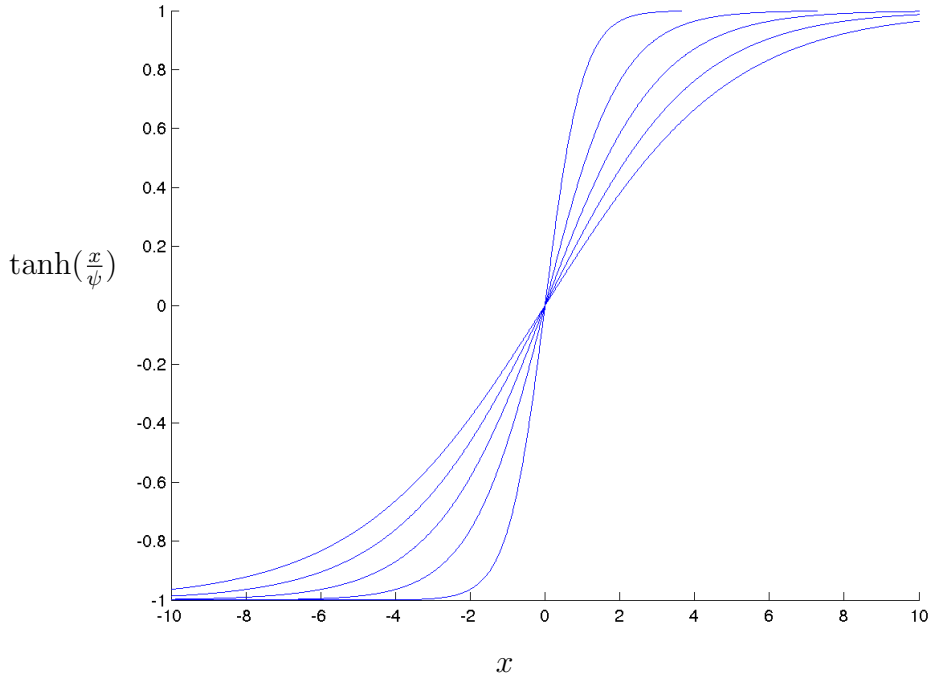


Figure 4.13: Hyperbolic tangent stretched with the factor ψ

The pressure injection has been observed to resemble a dipole [16] and has been modeled as such by Fabre and Verge [87]. To estimate the pressure jump they utilize a conformal mapping [52, 51], obtaining a pressure source whose amplitude strongly depends on the position of the sources with respect to the edge of the labium δ_d .

$$\Delta p_{jd} = -\frac{\rho_0 \delta_d}{S_m} \frac{dQ_{in}}{dt} \quad (4.28)$$

where ρ_0 is the air density and S_m the mouth surface.

Digression A dipole produces a convenient expression to estimate the magnitude of the pressure jump, but it creates equi-potential lines that do not fit with the measurements done by Coltman [16] (fig.4.14).

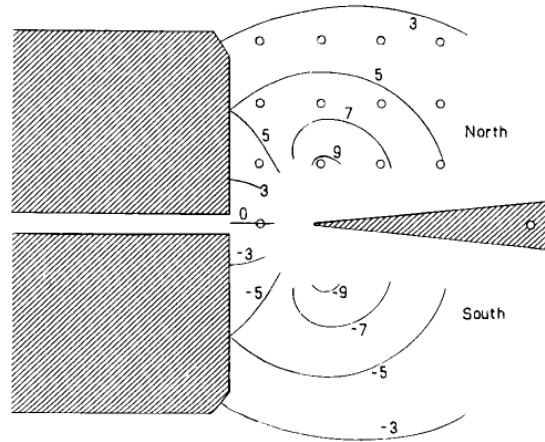


Figure 4.14: Contour of acoustic pressure (relative peak values) during edge-tone generation, measured by Coltman [16]

Alternatively the flow injection could be modeled as a doublet located close to the sharp edge (fig.4.9) (Coltman [16] suggested a position of 4mm away from the edge for his measurements).

Potential flow analysis is done to compare a dipole with a doublet. The pressure contours are parallel to the potential lines and perpendicular to the streamlines. In fig.4.15 the stream and potential lines are presented for both cases. Potential lines from a doublet (fig.4.15(d)) match correctly the shape of the pressure contours measured by Coltman (fig.4.14). While potential lines from a dipole (fig.4.15(b)) appear almost orthogonal to the measurements.

The drawback of the doublet is that some streamlines cross the resonator walls, which can be neglected if the interaction between the spherical waves produced by the doublet and the planar waves in the resonator is assumed to occur close to the source.

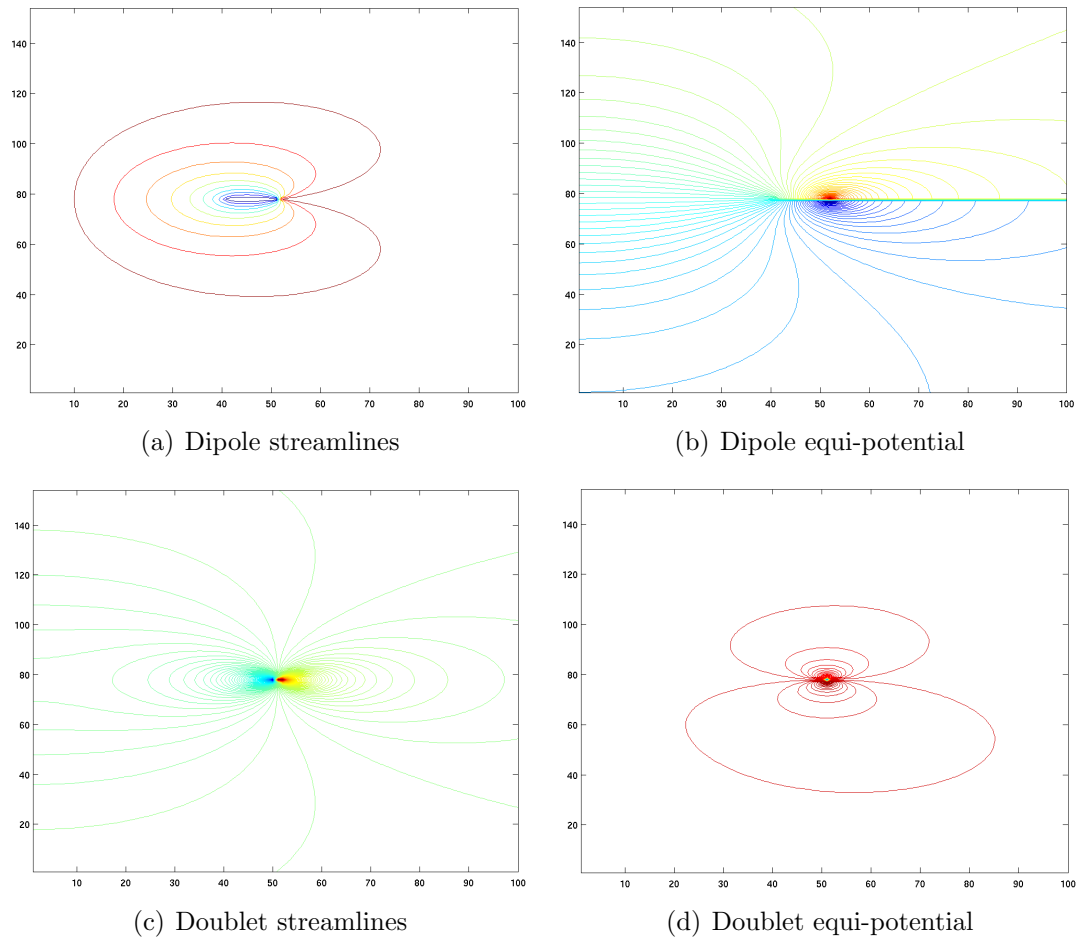


Figure 4.15: Comparison between the equi-potential and streamlines produced by a doublet and a dipole. a) Dipole streamlines; b) Dipole equi-potential lines; c) Doublet streamlines; d) Doublet equi-potential lines.

Vortices

The presence of vortices is observed in three places. In the shear layers of the jet; at the moment when the jet interacts with the labium and in the flow produced by the separation at the labium of the acoustic field exiting the mouth of the instrument. The first two are mechanisms of energy injection while the third one has been shown to damp energy for the fundamental [33]. Vortices are responsible for generating energy in high harmonics as well as for some non linear behaviors of the flute.

The power generated by shear layers has been calculated by Dequand [27] using Howe's [48] generalization of Powell's vortex-sound analogy [69]. The acoustical power averaged over one period of oscillations T is

$$P_v = \frac{-\rho}{T} \int_0^T \int_{V_s} (\omega \times v) u' dV dt. \quad (4.29)$$

where the volume of integration is taken over the source region of volume V_s and where the local acoustical flow velocity u' represents the unsteady part of the potential flow component of the velocity v .

The damping mechanisms produced by the vortex shedding in the mouth is model as a pressure jump across the mouth of the instrument

$$\Delta p_{vm} = -\frac{1}{2} \rho \left(\frac{V_{ac}}{\alpha_v} \right)^2 \text{sign}(Q_p) \quad (4.30)$$

where α_v is a geometric factor that can vary within the range $0.6 \leq \alpha_v \leq 1$.

Finally, the vortices generated by the jet labium interaction are neglected in our model.

Turbulences

Turbulences are critical in the perceptive evaluation of a synthesized flute sound. They are modeled following Verge's model of colored noise whose amplitude is proportional

to the square of the jet velocity,

$$\Delta p_t = K \frac{1}{2} \rho U_j^2, \quad (4.31)$$

where the constant K is adjusted empirically.

A block diagram of the interaction of different elements in the excitation is presented in fig.4.16.

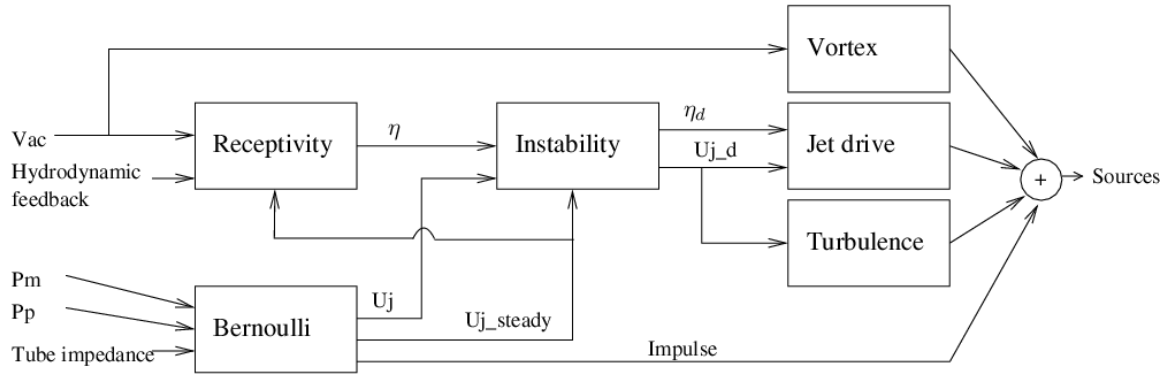


Figure 4.16: Sources detail

4.4 Implementation

The code has been developed as a C++ class. It has a modular structure in which each block is designed independently and only exchange inputs and outputs with other blocks.

In the highest level of the hierarchy (fig.4.17), the class *Flute* contains two subclasses *Resonator* and *Excitation*. The former implements the elements described in section 4.2 while the latter includes what is described in section 4.3. Building blocks such as delay lines, filters and tables are developed using the C++ library STK [19].

This modular and object-oriented structure allow independent substitution and adjustment of any of the model blocks and creates a model that can be instantiated

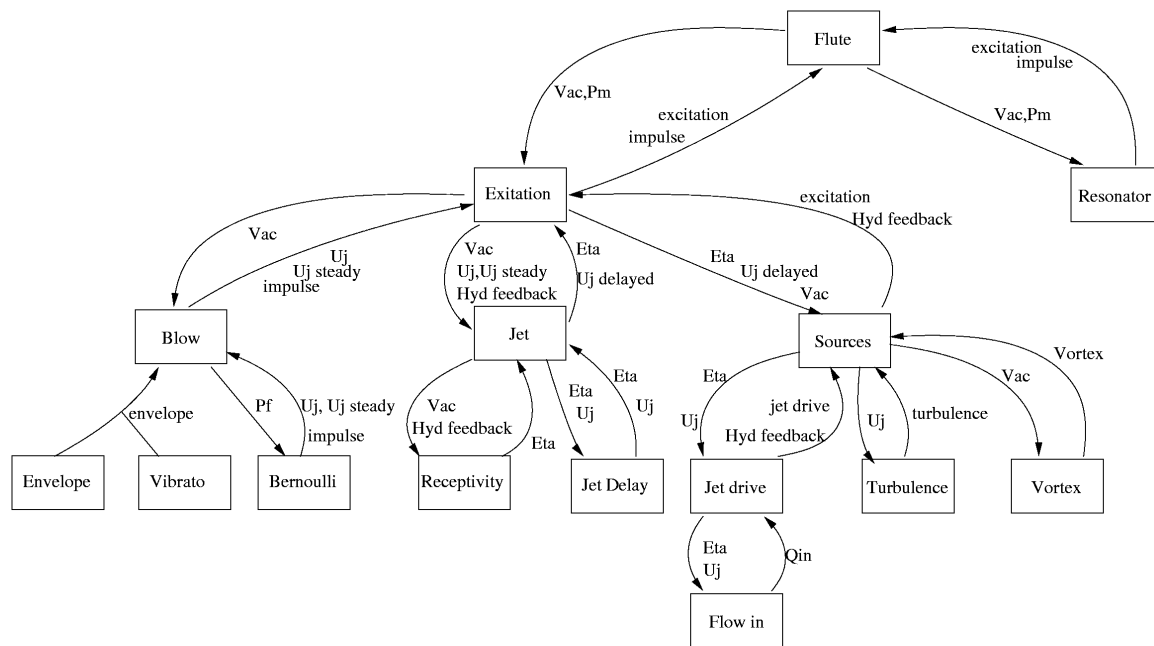


Figure 4.17: Code structure

under different environments. For the moment two possible instantiation have been chosen:

- A self contained program with a GUI designed in the spirit of a laboratory, that allow the user to control parameters in real time and visualize several physical variables both in time and frequency domain.
- A pd/Max-MSP external object capable of real time control over a set of parameters

4.4.1 Pitch adjustment

The pitch of the note depends on the length of the resonator, but also on the right adjustment of the excitation parameters. With the same resonator length, changes in the blowing can produce small variations in the pitch and jumps to different partials.

An optional mode of pitch control has been included. It allow the user to define a desired Strouhal number $Str = 2\pi fh/U_j$, so that when a frequency f is chosen the

jet velocity U_j and the cavity pressure p_c are automatically calculated and set. This mode provides a convenient way to obtain tuned melodies from the model controlling only one parameter f .

4.4.2 Flute laboratory

The system was designed in the spirit of a laboratory testbed, where geometric and performance parameters can be controlled in real time, and in which important physical quantities can be viewed in real time, either in the time domain or frequency domain. In this way, the user may observe and validate the behavior of variables that would otherwise be hidden in the feedback loop.

The graphical user interface (GUI) is developed using the qt library [71]. The control interface is separated in two tabs in the main widget. One to control the excitation parameters (fig.4.18) and another to control the resonator parameters and pitch adjustment (fig.4.19).

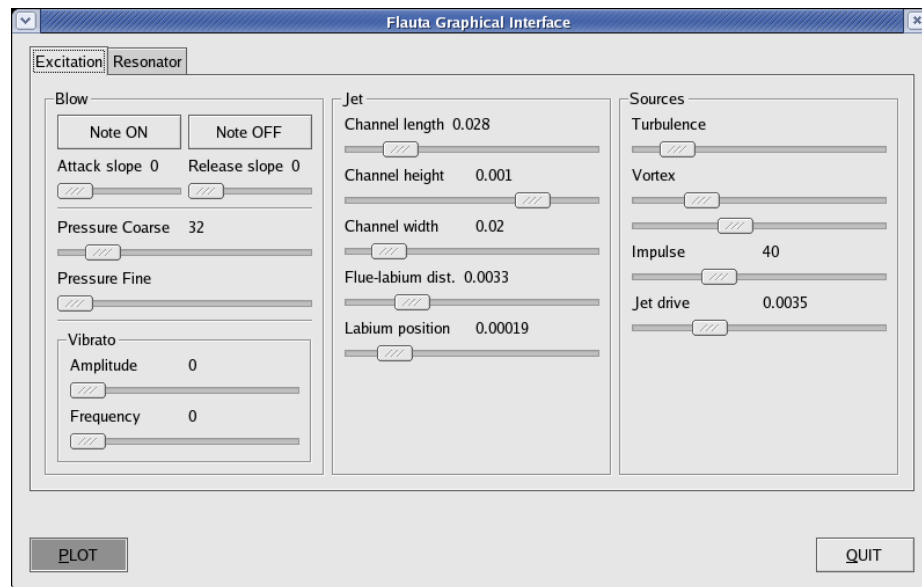


Figure 4.18: Excitation widget

In the visualization widget several variables can be visualized simultaneously by selecting them from a list available at the bottom of the widget.

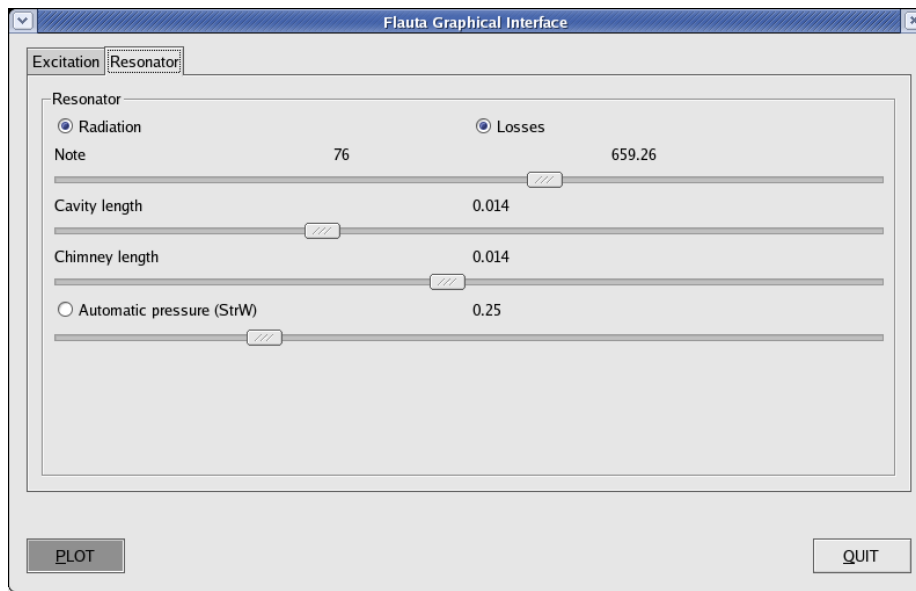


Figure 4.19: Resonator widget

While visualizing the signals in time domain, the refreshment rate of the image can be set with the slider on top of the plot and the length of the visualized frame can be adjusted with the slider below the plot as shown in fig.4.20.

In the frequency mode of the visualization widget (fig.4.21), the frame length is fixed and the lower slider provides a zoom into the lower part of the spectrum.

4.4.3 Pd/Max-MSP external object

Pd and Max-MSP are modular programmable software for music applications that allow event control through MIDI and other protocols. It a widely used application for musical creation and interactive performance.

The model has been instantiated as a Pd/Max-MSP external object where a set of control parameters allow for a real-time use of the system. Fig. 4.22 show a pd patch with an instantiation of the flute model under the name *flauta_pd*.

The pitch adjustment modes are set by passing messages to the first inlet with the text “pressure_free” or “pressure_from_pitch”.

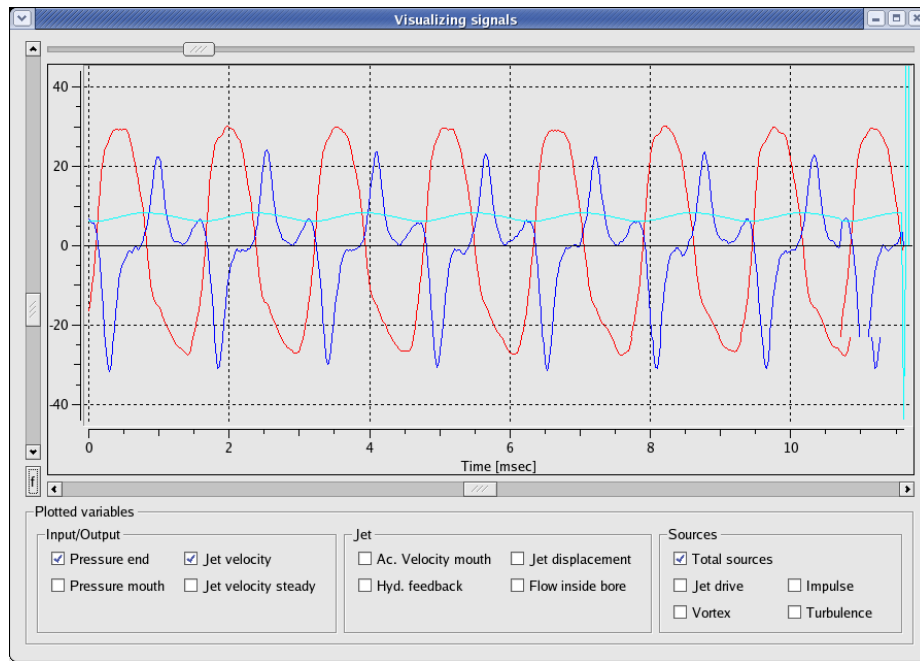


Figure 4.20: Time-domain visualization widget

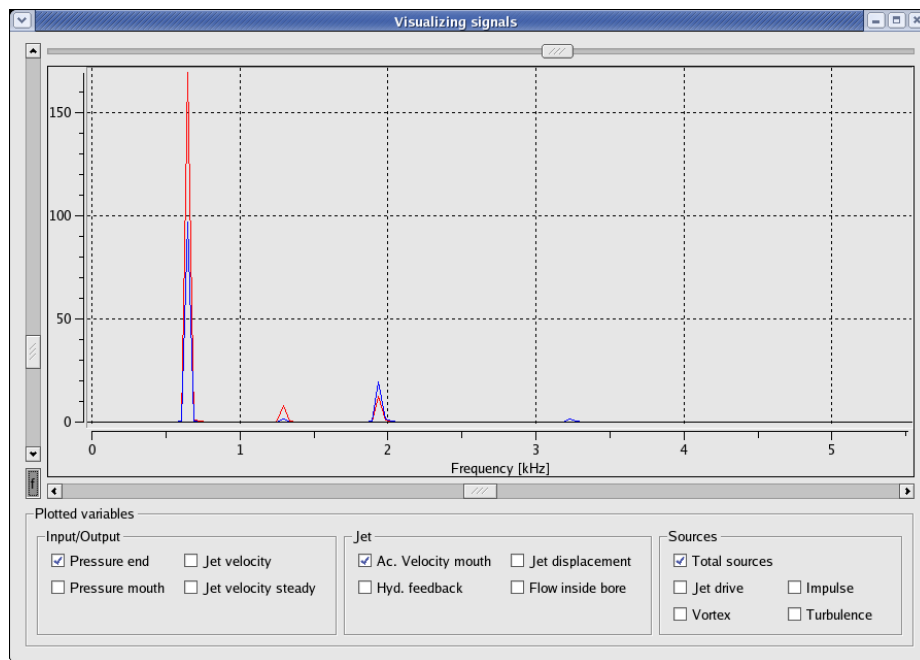


Figure 4.21: Frequency-domain visualization widget

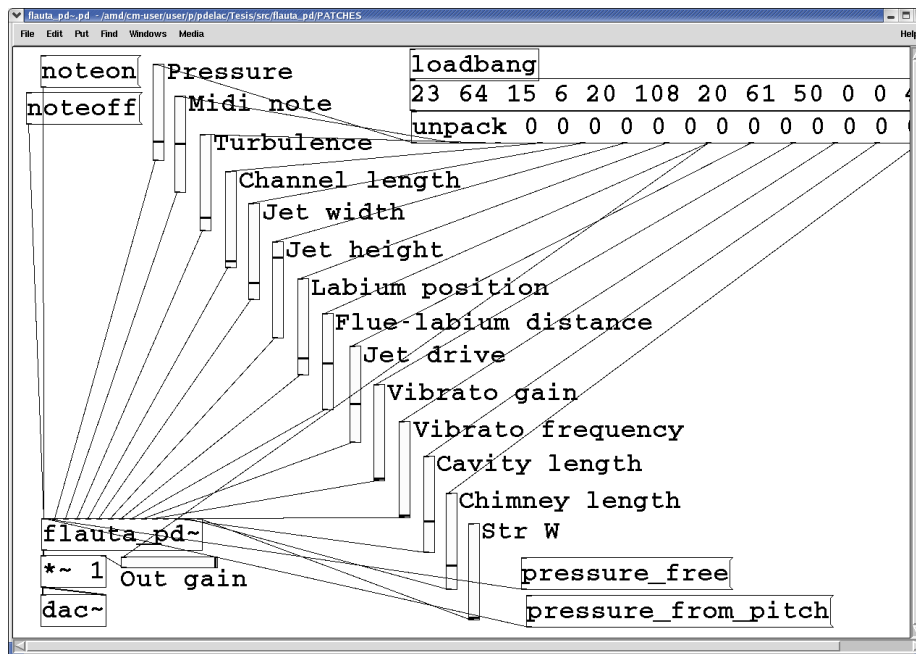


Figure 4.22: pd patch with external object of the flute model

4.5 Conclusions

Knowledge developed through decades of research are collected in a flute-like synthesis model capable of real-time operation. It provides an attractive tool to simulate, test and verify the different elements involved in the physics of the instrument. It also provides an interesting tool to both create and perform music. The sounds created, because their physical origin, remain close to our experience of natural flute sounds.

Chapter 5

A flute physical model application: the Ouldémé flutes

Abstract

This chapter describes the work done as part of an ethnomusicology study of the Ouldémé flute players that was carried out by an interdisciplinary group. A virtual flute based on physical modeling and controlled by the flutists through a dedicated midi control interface has been developed. A description of the project and the physical model is presented together with preliminary experimental results on the Ouldémé flute functioning.

5.1 Introduction

A virtual flute based on a physical model and controlled in real-time by MIDI sensors has been implemented as part of a collaboration project with ethnomusicologists. The aim of the project is to better understand musical scales used by Ouldémé flutists from North Cameroon [34]. Ouldémé culture is essentially oral, and the concept of musical analysis doesn't exist. Therefore, experiments with musicians are essential to better understand the underlying musical structure, including musical scales and more precisely the tuning strategy.

A typical female flute band is made by four or five women. Each one plays two flutes and sings one note before each blowing. Fine tuning is of crucial importance

and each player spends a lot of time choosing the right flute among a lot of nearly similar ones.

5.1.1 Experimental protocol

From preliminary experiments carried out by ethnomusicologists, it was not possible to find a precise tuning strategy since no reliable scale could be extracted from successive frequency measurements. The idea of ethnomusicologists was then to use synthesis models of flutes, with precisely adjustable pitch so that they could both record player's pitch adjustment and test their reaction to an imposed detuning, in the spirit of the work done for xylophones from Central Africa [2, 3].

Within this scope, we proposed to build a physical model of the Ouldémé flute to use for time domain sound synthesis. In order to avoid changing too much their habits of playing, we decided to create a controller for the physical model through gestural interfaces very close to real Ouldémé flutes and provide a synthesized sound as close as possible to the real one.

A description of the flutes functioning and some considerations on the model are described in section 5.2. Then, we focus on the real-time implementation of the model: the physical model, its implementation and the adjustment and control of the parameters are described in section 5.3 and section 5.4.

5.2 Investigation on Ouldémé Flute Functioning

5.2.1 Description of the way of playing

The Ouldémé flute is a simple piece of cylindrical bamboo closed at one end, without toneholes, similar to the Latin American pan pipes or *zampoñas*. There is no particular cut for the mouthpiece. The length of each flute is chosen to match the desired playing frequency. For our set of flutes, the length varies from 14cm to 42cm.

Placing the tongue outside of the mouth, the player shapes the air stream between her tongue and her upper lip, directed toward the edge of the cane, as shown in fig.5.1.

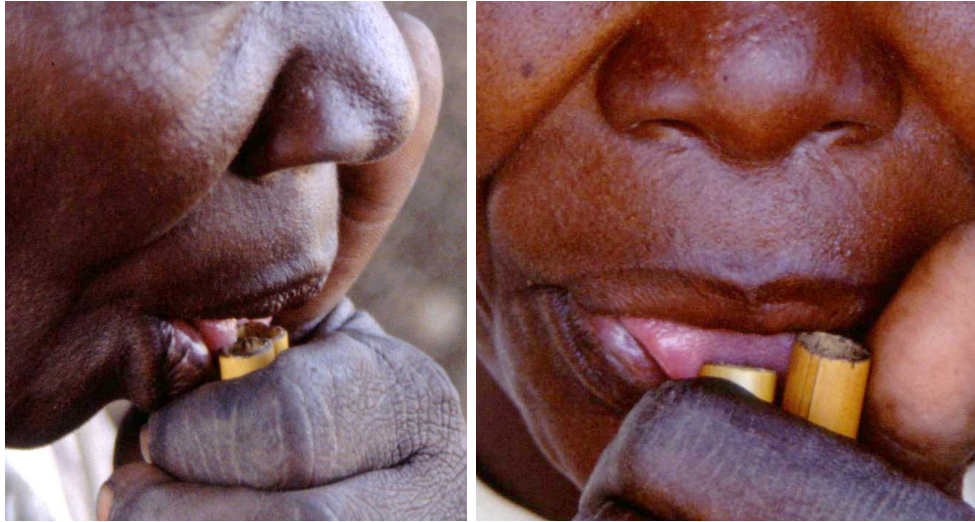


Figure 5.1: Ouldémé flutists.

Before playing, the inside of the flute is moistened creating a thin film of water. Its effect on the flute functioning is studied in section 5.2.2.

The Reynolds estimated from mouth pressure measurement together with lip opening evaluation was found to be of the order of $Re \simeq 6000$. This value together with the noisy sound produced by the flutes make us assume the presence of a turbulent jet. An experimental study aimed to characterize the behavior of the turbulent jet submitted to a transverse acoustical field has been initiated, and preliminary results are presented in section 5.2.3.

5.2.2 Adding water

Three effects of the addition of water have been considered.

First, like in many other bamboo instruments, the inner surface has to be moisturized in order to prevent air leakage due to the porosity of bamboo.

A second effect is the fine tuning of the flute. In addition to the frequency shift due to the decrease of the inner volume, the thin film of water in the inner surface produces a non-negligible effect. Indeed, impedance measurements made with wet and dry flutes show that the first resonance frequency (close to $300Hz$) is increased by 1.5% (1/8 of a tone, i.e. 25 cents) when they are wet. The third effect is the amplitude

increment of the resonance peak by 9% for wet flutes. Therefore adding water on inner surface makes playing easier, effect that is well known among musicians.

5.2.3 Turbulent jet

Flue instruments like other sustained instruments, can be described as an excitation coupled to a resonator. The excitation consists of an intrinsically unstable jet which is directed toward a sharp edge, known as labium.

Instruments operating with a laminar jet have been widely studied and the literature on recorder-like instruments is important (see for example [84] and [32]). However, this is not the case for instruments, like the Ouldémé flute and some other flutes used in traditional or popular music, which can be suspected to operate with a turbulent jet.

The behavior of turbulent jet and their coupling with the transverse acoustic field coming from the resonator is less understood than the laminar one. For that reason, an experimental study has been initiated [53] oriented to better describe turbulent jets and its implications in the Ouldémé flute functioning.

Experimental setup

The aim of the experiment is to characterize the behavior of a turbulent free jet submitted to a transverse acoustic field. The jet is created by blowing compressed gas through a channel with rectangular cross section. The periodic acoustic field is induced by a pair of speakers, facing each other and connected in opposite phase. Stroboscopic visualization of the jet is done using the Schlieren technique. Image detection algorithms are applied to each image in order to determine the time evolution of the centerline of the turbulent jet, as shown in fig.5.2.

The Reynolds number is controlled by varying the blowing pressure, while the Strouhal number is controlled by changing the driving frequency of the speakers. Experiments have been carried out for Re lying between 1000 and 6000, and for Str lying between 0.01 and 0.03. Fig.5.3 shows a the evolution from laminar jet (low Re) to a turbulent jet (high Re).

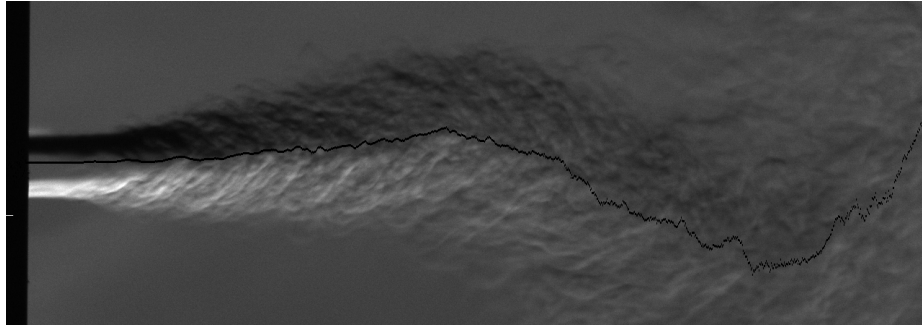


Figure 5.2: Center line detection by image processing

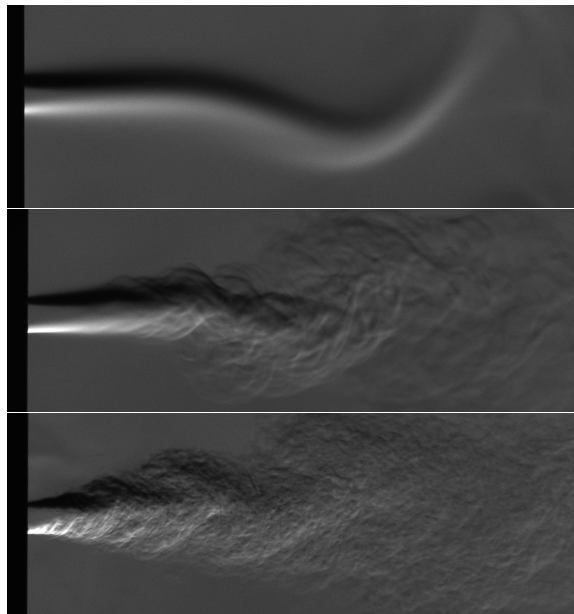


Figure 5.3: Jet under acoustic excitation by loudspeakers. From top to bottom: $Re = 200, 500$ and 3000 .

Preliminary results

It has been observed that the behavior of the turbulent jet is qualitatively similar to the behavior of a laminar jet in the sense that transverse waves propagate along the jet.

A relevant parameter to describe the behavior of the jet is the propagation velocity of the transverse waves traveling along the jet. Measurements carried out for different Re (see fig.5.4) indicate that during the transition from a laminar to a turbulent regime, the velocity of hydrodynamics perturbations (adimensionned by the jet average velocity at the channel output, estimated using Bernoulli's equation) slow down by a factor 2. This result could explain the stability of the Ouldémé flute on the first regime of oscillation for a larger range of blowing pressures than the recorder. A decrease on the wave propagation velocity in turbulent jets was also measured by [80] although the magnitudes found are different.

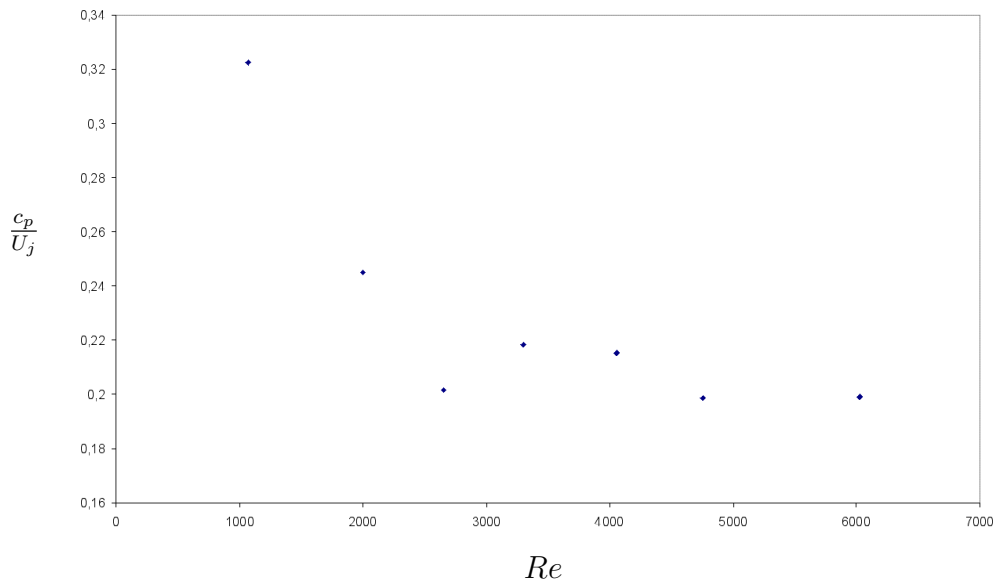


Figure 5.4: Influence of Reynolds number (Re) over the speed of the perturbations (c_p/U_j) for a constant Strouhal number ($Str=0,018$).

Another relevant parameter to describe the jet is the amplitude of the jet deflection (adimensionned by the acoustic displacement) when it is submitted to periodic transverse perturbations. Experiments clearly indicate that a turbulent jet is far less

sensitive to perturbations than a laminar jet. Like in the laminar jet, for a given Re , the sensitivity of the jet is highly dependent on the Str number. For example, fig.5.5 shows the dimensionless amplitude of the jet deflection at a given distance from the channel output, for different Str .

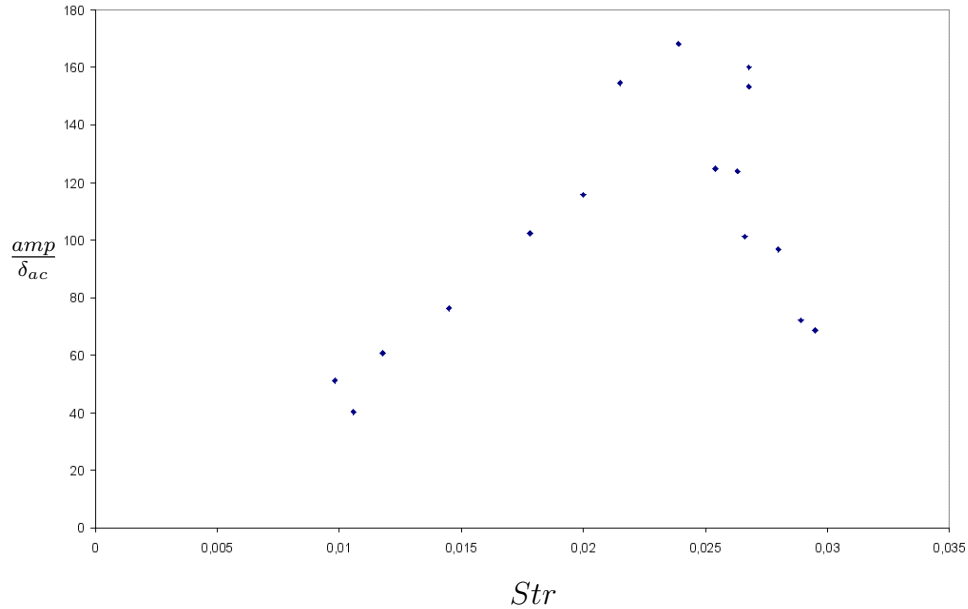


Figure 5.5: Influence of Strouhal number over adimensional amplitude, for a constant Reynolds number ($Re = 2600$).

5.2.4 Discussion - Toward a model of the Ouldémé flute

The effects of water inside the flute (discussed in section 5.2.2) can easily be included in a physical model by decreasing the equivalent length of the resonator and by lessening viscous losses.

Concerning the behavior of the turbulent jet, further investigations are now being carried out to refine the results presented above [54]. However, these first results already provide us with a guideline concerning the physical modeling. Indeed, as discussed in section 5.2.3, transverse perturbations propagate along the turbulent jet. Clearly as seen in 5.2.3, compared to the laminar case, they propagate at a different

speed and with different amplification along the jet. However these differences can be taken into account by different scaling factors in a physical model.

Therefore, within the context of a simple model, the well known model of recorder-like instruments can be adapted to the particular characteristics of Ouldémé flutes. This is done in section 5.3.

5.3 The model - Implementation

A one-dimensional model of a flue instrument [87] has been ported to MAX/MSP [58] and STK [19]; two platforms that allow real time execution. In order to have control over the timbre, the implementations were designed allowing interactive manipulation of a set of relevant parameters.

The model is driven by the input pressure. The bore is modeled by a one dimensional waveguide [79] using fractional delay lines [45] to allow continuous pitch control. Low-pass digital filters are used to describe radiation and visco-thermal losses in the bore.

For the excitation, the following lumped elements are included:

- Jet-labium interaction, including the contribution of the acoustic field from the pipe, the direct hydrodynamic feedback from the edge of the labium, the amplification of the perturbations in the jet and its convection toward the labium.
- Vortex shedding at the labium is believed to be responsible for the major non-linear amplitude limiting mechanism of the pressure in the bore as well as the generation of high harmonics in the spectra.
- Turbulent noise is added by filtering white noise and scaling it by a constant depending on the jet velocity.

These elements model the most relevant features of the jet dynamics including the formation, velocity fluctuation and oscillations.

Even though there are some quantitative differences between the behavior of a turbulent and laminar jet (which could motivate the development of more specific

models), the current model captures the common principle of operation and allows us to stretch its possibilities obtaining sounds that closely resemble those of the Ouldémé flute.

5.4 Adjusting and controlling the model

After exploring the influence of all the parameters on the synthesized sound the following set was chosen:

- Jet traveling distance before reaching the labium
- Jet position with respect to the labium
- Coupling gain; incidence of the jet injection over acoustic waves
- Vortex amplitude; damping effect caused by vortex shedding at the labium
- Cutoff frequency of visco-thermic losses filter
- Turbulent noise gain

The desired timbre was obtained by tuning these parameters and comparing the results with a recorded sound from the real flute.

To emulate a real performance situation, a cylindrical bakelite device was built keeping the dimensions of the original flutes. A differential pressure sensor has been inserted close to the embouchure of the flute to assure short delays in the response of the instrument. The blow is directed toward one edge of the flute, therefore the sensor was located near the upper side of the bore. It was necessary to create a conic shape to conduct the maximum amount of flow into the sensor.

Analog amplification and low-pass filtering was used to create an envelope of the pressure signal.

Another controller was designed to adjust the pitch of the synthesized sound. Two buttons have been inserted in the tube allowing the performer to raise or lower the pitch. Signals are then fed into an analog-to-midi interface [43] giving MIDI inputs

for the input pressure and pitch of the model. The complete system is shown in fig.5.6 and 5.7.



Figure 5.6: Synthetic flute with sensors.

5.5 Conclusion

An ethnomusicologist study regarding the tuning strategy of the Ouldémé flutists has been assisted by the use of sound synthesis by physical modeling and real-time MIDI control.

Through a preliminary experimental study of the Ouldémé flute functioning, it has been highlighted that a simple physical model could reasonably be derived from the (better known) model of recorder-like instruments. Parameters of the model have then been adjusted to produce sounds very close to natural sounds. Efficient real time implementation has been performed allowing the use of up to ten instantiations of flutes with 30 MIDI controllers simultaneously using MAX/MSP in a Macintosh laptop (PowerBook G4, 400MHz).

It is worth noting that an alternative synthesis technique based on samples of their original flutes, was tested by Ouldémé players using the same MIDI control interface. The preferred synthesis technique was incontestably physical modeling, judged more natural by Ouldémé flute players.



(a)



(b)

Figure 5.7: Ouldémé flute players using synthetic flutes.

Appendix A

Understanding the Schlieren method

A.1 Fluid flow as a refractive index field

Changes in the fluid density cause variations in the refractive index. But these variations remain invisible to the naked eye, and optical methods are required for making them visible [62].

A light transmitted through a flow field could be used to visualize the changes on its refractive index. The beam is deflected from its original direction and that effect could be used not only to visualize the field but also to perform quantitative density measurements.

We will first find a relation between the fluid density ρ and the refractive index n , which is a measure of the speed reduction of the light when it crosses a transparent medium, $n = c_0/c$. Then we show how light gets deflected when it crosses through an inhomogeneous media and finally we use both facts to show how Schlieren method works.

A.1.1 Relation between fluid density ρ and refractive index n

The light is an electromagnetic wave with an electric field vector \mathbf{E} that distorts the charge configuration of the fluid molecules as it travels through them. Thus a dipole moment \mathbf{p} is induced per molecule proportional to \mathbf{E} :

$$\mathbf{p} = \alpha \mathbf{E} \quad (\text{A.1})$$

The proportional factor α can be estimated using the classical radiation interaction theory of Lorentz. Where \mathbf{p} is related to \mathbf{E} using the model of an induced harmonic electron oscillator:

$$\mathbf{p} = \frac{e^2 \mathbf{E}}{4\pi^2 m_e} \sum_i \frac{f_i}{\nu_i^2 - \nu^2} \quad (\text{A.2})$$

therefore,

$$\alpha = \frac{e^2}{4\pi^2 m_e} \sum_i \frac{f_i}{\nu_i^2 - \nu^2} \quad (\text{A.3})$$

where e is the charge and m_e the mass of an electron, ν the frequency of the light used ($\mathbf{E} = \mathbf{E}_0 \exp(i2\pi\nu t)$), ν_i the resonant frequencies of the fluid and f_i its correspondent amplitudes.

The neighbor molecules also become electric dipoles inducing a secondary field in the molecule being analyzed. If we include this effect, eq.A.1 becomes $\mathbf{p} = \alpha \mathbf{E}_{eff}$ where \mathbf{E}_{eff} is an effective field vector which also takes into account the secondary field:

$$\mathbf{E}_{eff} = \mathbf{E} + \frac{4}{3}\pi \mathbf{p} \quad (\text{A.4})$$

\mathbf{p} designates again the polarization vector, that is the net dipole moment per unit volume of the dielectric medium. Let N be density number of molecules in the fluid, then Eq.A.1 reads:

$$\mathbf{p} = \alpha N \left(\mathbf{E} + \frac{4}{3}\pi \mathbf{p} \right) \quad (\text{A.5})$$

The following relation is also known, from Maxwell equations:

$$\mathbf{p} = (\varepsilon - 1) \frac{\mathbf{E}}{4\pi} \quad (\text{A.6})$$

where ε is the dielectric constant of the medium.

In Eq.A.5, N can be replaced by the density ρ through $N = \zeta\rho/M$, where ζ is the Loschmidt's number and M the molar weight of the fluid. The refractive index $n = \sqrt{\varepsilon}$, which together with eq.A.2 and A.6 give us the relation between the refractive index n of a fluid and its density ρ , known as the Clausius-Mosotti equation:

$$\frac{n^2 - 1}{n^2 + 2} = \frac{\rho\zeta e^2}{3\pi m_e M} \sum_i \frac{f_i}{v_i^2 - v^2} \quad (\text{A.7})$$

This relation apply both to gases and liquids although in most gases $n \simeq 1 \Rightarrow (n^2 - 1) \simeq 2(n - 1)$ and $(n^2 + 2) \simeq 3$. Then we obtain the Gladstone-Dale relation:

$$n - 1 = \rho \frac{\zeta e^2}{2\pi m_e M} \sum_i \frac{f_i}{v_i^2 - v^2} \quad (\text{A.8})$$

or the abbreviated form:

$$n - 1 = K\rho \quad (\text{A.9})$$

The constant K depends on certain characteristics of the gas as well as on the frequency of the light used. K is about $0.23 \text{ cm}^3/\text{g}$ for air at standard conditions, given visible illumination.

A.1.2 Deflection of a light ray in an inhomogeneous density field

We now investigate the problem of how a light ray is disturbed in an inhomogeneous refractive field. The refractive index n is assumed to vary as a function of the three coordinates in the flow field, i.e $n = n(x, y, z)$. The incident light beam is assumed to arrive parallel to the z axis, as shown in Fig.A.1.2.

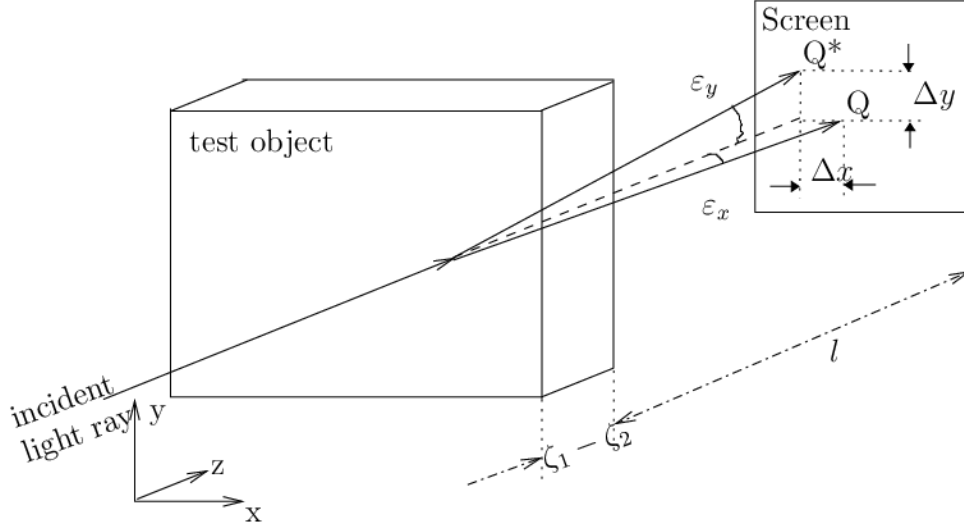


Figure A.1: Deflection of a light ray in an inhomogeneous test object

The propagation of a single light ray in the refractive field is described by Fermat's principle, which states that *the variation of optical path length along a light ray in the object must vanish*; hence:

$$\delta \int n(x, y, z) ds = 0, \quad (\text{A.10})$$

where s denotes the arc length along the ray and ds is defined by $ds^2 = dx^2 + dy^2 + dz^2$. Eq.A.10 is equivalent to the following set of differential equations:

$$\frac{d^2x}{dz^2} = \left\{ 1 + \left(\frac{dx}{dz} \right)^2 + \left(\frac{dy}{dz} \right)^2 \right\} \left\{ \frac{1}{n} \frac{\partial n}{\partial x} - \frac{dx}{dz} \frac{1}{n} \frac{\partial n}{\partial z} \right\} \quad (\text{A.11})$$

$$\frac{d^2y}{dz^2} = \left\{ 1 + \left(\frac{dx}{dz} \right)^2 + \left(\frac{dy}{dz} \right)^2 \right\} \left\{ \frac{1}{n} \frac{\partial n}{\partial y} - \frac{dy}{dz} \frac{1}{n} \frac{\partial n}{\partial z} \right\}$$

System which is normally difficult to solve without doing some simplifications. Deviations from the z direction of a light ray in a compressible gas flow are negligibly small,

but the ray may leave the test field with a non-negligible curvature. Therefore one may assume that the slopes of the ray, dx/dz and dy/dz , are very small with respect to 1; and since in most cases $\frac{\partial n}{\partial x}$, $\frac{\partial n}{\partial y}$ and $\frac{\partial n}{\partial z}$ are of the same order of magnitude. The simplified system of equations becomes:

$$\frac{d^2x}{dz^2} = \frac{1}{n} \frac{\partial n}{\partial x}, \quad \frac{d^2y}{dz^2} = \frac{1}{n} \frac{\partial n}{\partial y} \quad (\text{A.12})$$

We can now use these expressions to obtain the following observable quantities in the recording plane (see Fig.A.1.2):

$$(QQ^*)_x = l \int_{\zeta_1}^{\zeta_2} \frac{1}{n} \frac{\partial n}{\partial x} dz, \quad (\text{A.13})$$

$$(QQ^*)_y = l \int_{\zeta_1}^{\zeta_2} \frac{1}{n} \frac{\partial n}{\partial y} dz, \quad (\text{A.14})$$

$$\tan \varepsilon_x = \int_{\zeta_1}^{\zeta_2} \frac{1}{n} \frac{\partial n}{\partial x} dz, \quad (\text{A.15})$$

$$\tan \varepsilon_y = \int_{\zeta_1}^{\zeta_2} \frac{1}{n} \frac{\partial n}{\partial y} dz, \quad (\text{A.16})$$

The shadowgraph technique visualizes the displacement QQ^* while the Schlieren system measures the deflection angle ε .

A.2 Schlieren method

The principle of this method was developed around 1860 and is attributed to Foucault or Toepler, depending on the authors' national preference. Its strength is based on the combination of relatively simple optical arrangement with a high degree of resolution.

Fig.A.2 shows the basic implementation. The beam from a punctual light source is made parallel with a lens, which then crosses a test area. The second lens refocuses the beam to an image of the point source. From there the beam proceeds to a viewing

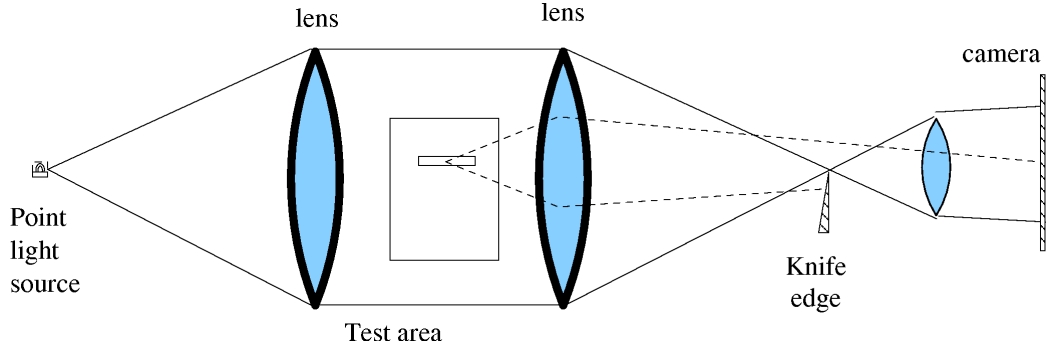


Figure A.2: Schlieren basic implementation

screen where a real inverted image of the test area is formed. A knife edge is placed in the focus of the second lens.

A.2.1 Analytical description

Let's assume that the light source has rectangular section $b * a$, with a being the height. The intensity I at any point (x, y) at the arriving screen is given by:

$$I(x, y) = \eta I_0 (ab / f_c^2) = \text{const}, \quad (\text{A.17})$$

where I_0 is the original intensity of the light source, η an absorption coefficient describing the loss of intensity on the way from the light source to the knife-edge plane, and f_c is the focal length of the camera lens.

If a disturbance in the test section deflects the light rays by an angle of ε , its correspondent image in the screen will be shifted by Δa and Δb as shown in Fig. A.3. If ε_y is the vertical component of ε and f_2 is the focal length of the right lens, then

$$\Delta a = f_2 \tan(\varepsilon_y) \cong \varepsilon_y f_2 \quad (\text{A.18})$$

The light intensity is changed by

$$\Delta I = \eta I_0 (\Delta ab / f_c^2) \quad (\text{A.19})$$

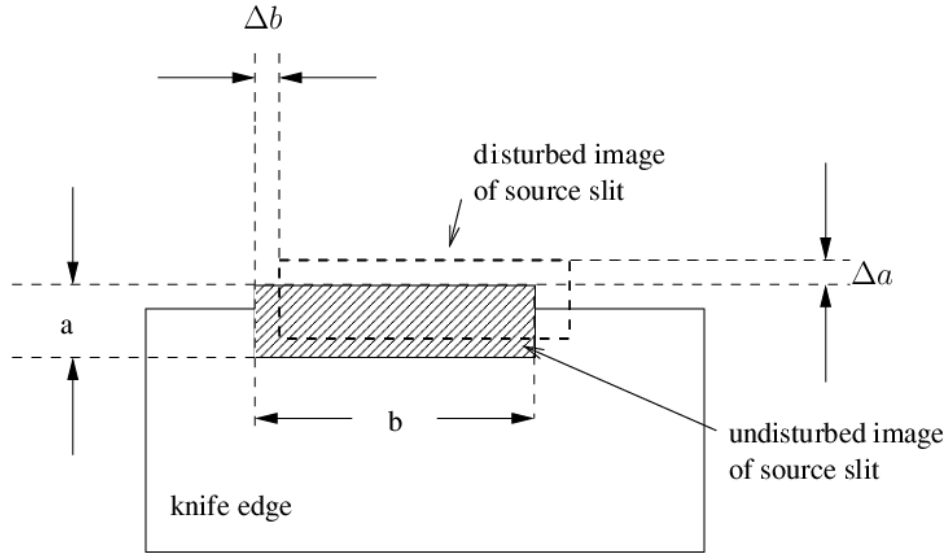


Figure A.3: Shift of slit-shaped light source image in the plane of the schlieren knife edge

The photographic process allows one to measure relative changes, then

$$\frac{\Delta I}{I} = \frac{\Delta a}{a} = \varepsilon_y (f_2/a) \quad (\text{A.20})$$

Replacing ε_y from Eq.A.15 we can see that the local change of intensity ($\Delta I/I$) in a Schlieren image can be evaluated to obtain the gradient of the refractive index in the test field:

$$\frac{\Delta I}{I} = \frac{f_2}{a} \int_{\zeta_1}^{\zeta_2} \frac{1}{n} \frac{\partial n}{\partial y} dz \quad (\text{A.21})$$

For gases $n \cong 1$ and using the Gladstone-Dale relation we obtain:

$$\frac{\Delta I}{I} = \frac{K f_2}{a} \int_{\zeta_1}^{\zeta_2} \frac{\partial \rho}{\partial y} dz \quad (\text{A.22})$$

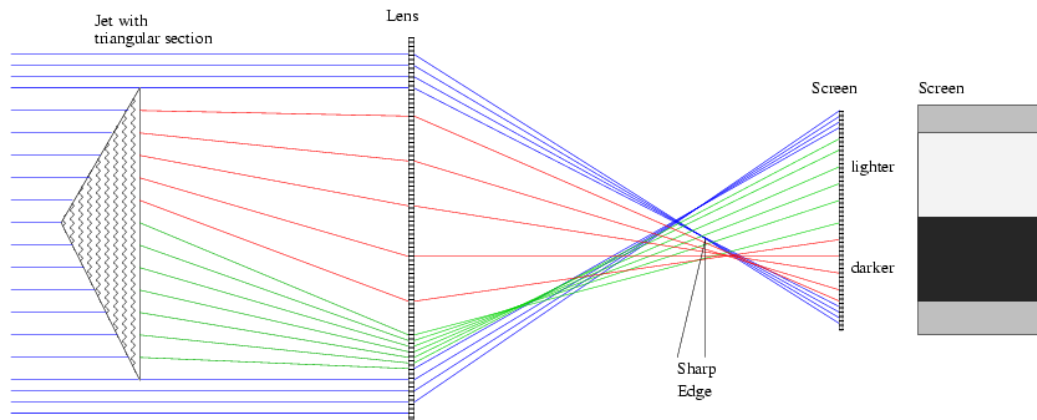


Figure A.4: Idealized triangular jet traveling perpendicular to the plane shows how the density changes are converted into light intensity in the screen

A.2.2 Geometric description

If we add an object to the test area, it bends light rays away from their original path. Let us assume that our object is a jet traveling perpendicular to the plane of the figure with a triangular section as shown in Fig. A.4. It will provide two constant vertical density gradients $\partial n/\partial y$. The light rays going closer to the central corner are going to be more deflected. Then the lens is going to focus the parallel rays to a common focal point and those that came with a certain angle are going to be misplaced. We notice that the object produced a non-homogeneous distribution of light between the lens and the screen. This allows us to block some of the rays by placing a sharp edge in the proper place, producing a change of intensity in the screen. In other words, the phase difference causing a vertical gradient $\partial n/\partial y$ in the test area is converted to an amplitude difference, making the invisible field visible. It is important to notice that for the orientation of the knife shown in Fig. A.4 only the vertical component $\partial n/\partial y$ of the gradient could be visualized.

Appendix B

Image detection algorithms

Part of this appendix has been published as a conference paper in [8].

B.1 Image processing

The goal of the image processing algorithm is to detect the position of the jet (or its center) for every image. Three algorithms are proposed pointing out the strengths and weakness of each one.

B.2 Cross-correlation method

A first algorithm explores the possibility of including all the imperfections of the image sequence as useful information to find the position of the jet. A typical intensity shape of one column of a Schlieren image is shown in Fig.B.1. The maximum and minimum correspond to the brighter and darker part of the image, which ideally should be of the same height, but it is very difficult to obtain experimentally. For a particular column that shape doesn't change much as time goes on, it is only shifted following the movement of the jet. Every column has its own particular shape, which is determined by the mass distribution of the jet and varies as the jet moves away from the flue exit. The algorithm will try to find the relative position of that shape.

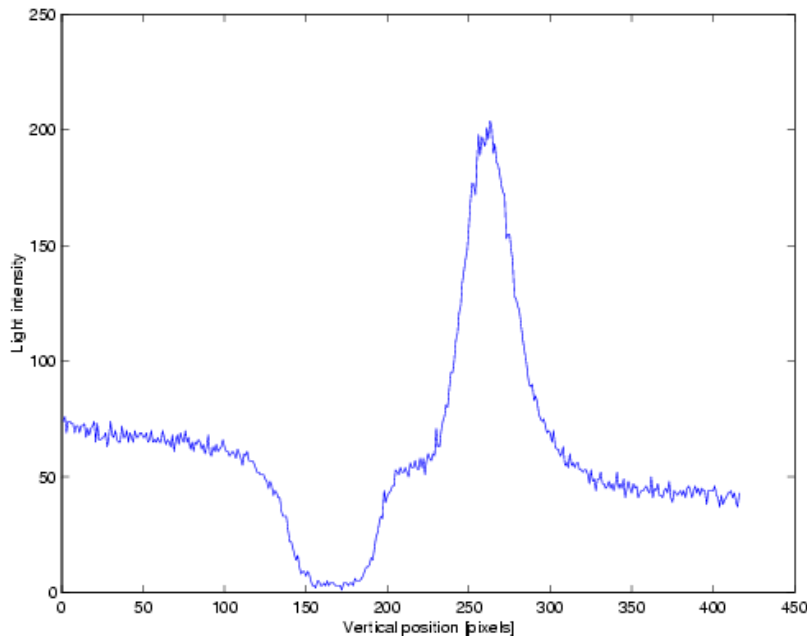


Figure B.1: Intensity level of a single column from a Schlieren image

The background intensity is also difficult to adjust experimentally. Ideally it should be homogeneous, which corresponds to a horizontal line in Fig.B.1. However we observe that it normally has some inclination.

B.2.1 The algorithm

An arbitrary image is set as a reference. It normally corresponds to the first image. The position of the other images from the sequence are calculated as distances from the reference obtaining a relative position for the whole sequence. Finally the position of the reference is determined and subtracted from the relative position to obtain the actual position.

The gray intensity shape is used to calculate a cross-correlation between every column from the first image X_{ref} and the same column from all other images of a

sequence X_t .

$$Y(l, t) = \sum_{i=1}^N X_{ref}(i) * X_t(l + i),$$

$$l = -N + 1, \dots, 0, \dots, N - 1 \quad (\text{B.1})$$

$$t = 1, \dots, M$$

where, N is the number of dots per column, and M the number of images

A typical curve for the cross correlation output $Y(l, t_0)$ is shown in Fig.B.2. The horizontal distance from the peak to the center of the frame corresponds to the distance from the current position of the jet column with respect to the reference.

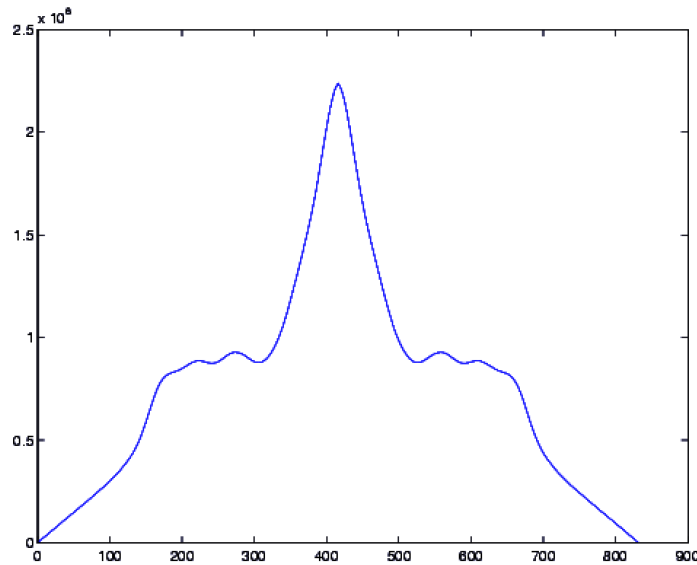


Figure B.2: Curve obtained from a cross-correlation of the same column in different moments of the sequence

Changes on the jet position are normally smaller than one pixel. Therefore, in order to improve the resolution of the detection parabolic interpolation is used. A parabola of the form $y(x) = a * (x - p)^2 + b$ is fit to the three highest points and

the position p is determined as an approximation to the real peak position. Fig.B.3 shows the result of a sequence of images obtained.

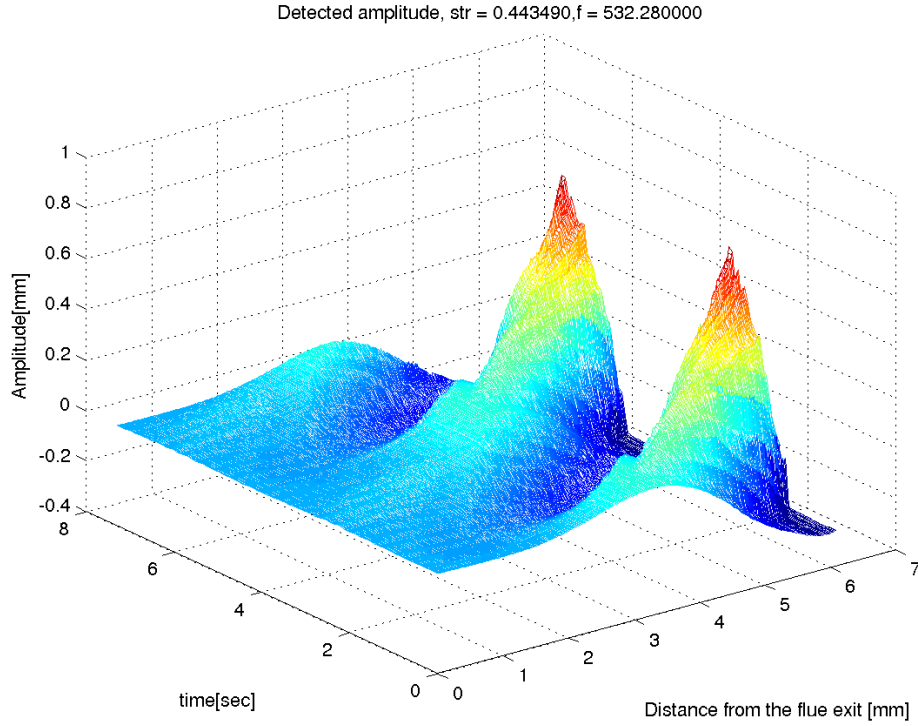


Figure B.3: Position of jet, excitation frequency = 532.28 Hz

B.2.2 Position of the reference image

Positions for every image are calculated as distances from the reference image. So an estimation of the actual position of the reference is needed to subtract it from the rest of the sequence and obtain the real position of the jet in time.

Sequences of images are defined to cover exactly 2 cycles of oscillation. For each column, a sinusoid is fit with an offset that has to be estimated:

$$X_m = A \cos(\omega t + \phi) + \Delta \quad (\text{B.2})$$

a good estimation $\hat{\Delta}$ of Δ is

$$\hat{\Delta} = \frac{\int_0^T X_m}{T} \quad (\text{B.3})$$

since we can retrieve the original signal X by doing:

$$X = X_m - \hat{\Delta} = A \cos(\omega t + \phi) + \Delta - \frac{\int_0^T X_m}{T} = A \cos(\omega t + \phi) \quad (\text{B.4})$$

Therefore the position of the reference image $\hat{\Delta}$ is estimated by calculating the time average of every column.

B.2.3 Phase analysis

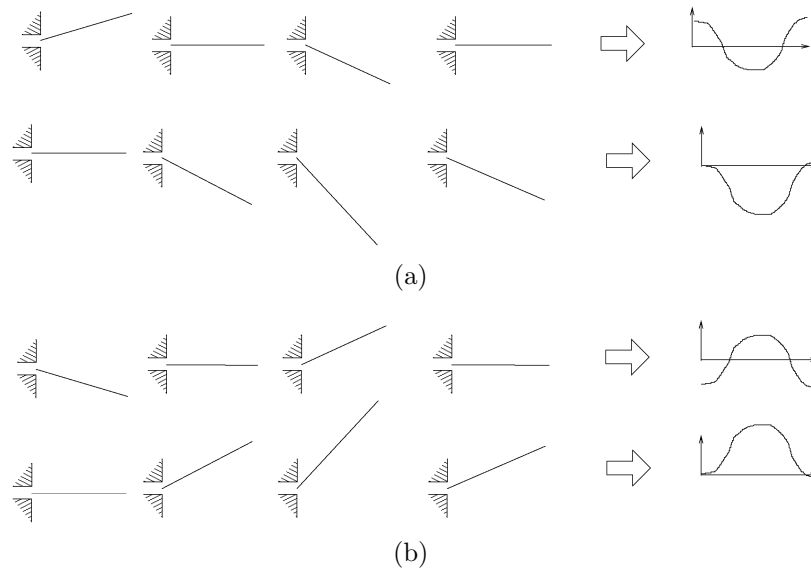


Figure B.4: The phase is preserved using the cross-correlation algorithm

The phase of the oscillation of each column is preserved, as can be graphically observed in fig.B.4. There are two cases, fig.B.4(a) the jet starts the oscillation with a positive value, (i.e. it begins above the center line) and fig.B.4(b) the jet starts the oscillation with a negative value. In both cases it is assumed that the jet is moving as a straight line, which is a correct simplification since the analysis is done column by column and they are all oscillating at the same frequency.

The first row of fig.B.4(a) show a plot of the displacement of the jet in four moments of the oscillation in time $(0, \pi/2, \pi, 3\pi/2)$. The second row shows what cross-correlation algorithm would detect if the first image is used as reference. The

time displacement of both the actual jet and the cross-correlation detection are shown to the right of the figure. We observe that the phase is exactly the same but there is an offset in amplitude. The same analysis with the jet starting in the lowest position is shown in fig.B.4(b).

B.3 Morphological method

The idea of this method is to apply morphologic functions on binary images to find large scales in the image that correspond to the jet. This is done by the five steps:

- Contrast homogenization and enhancement by histogram equalization.
- Conversion from gray scale to black and white images: a statistical method based on the Otsu principle is used to estimate the threshold that better separates the histogram within two classes. The binary threshold is therefore different for each image.
- Extract the largest spatial scales in the image: a morphological opening is performed to clean all small structures. Then a morphological closure is applied to highlight large scales in the image. The size of the structuring element is found empirically and is the same for all the images of a sequence.
- Identification of the jet among the large scales found at previous step : the image is analyzed in terms of groups of contiguous pixels. A separation criteria is created based on geometrical characteristics calculated for each region. It involves the area of the jet region jet and the localization of each region in the image.
- Jet edges and median line estimation: jet edges detection is performed with Sobel algorithm which uses gradient information. Finally, for every column of the image the median point is found using empirical criteria to select the correct path among several options. This guarantees that the resulting median line is single-valued, but possibly discontinuous where vortices appear.

Since we are interested in both halves of the jet (darker and brighter in fig.B.5), all the operations described above are applied to a 1-complemented image. The results of the method are shown in fig.B.5. Putting together median lines found for each image, a 3D plots similar to fig.B.3 can be created.

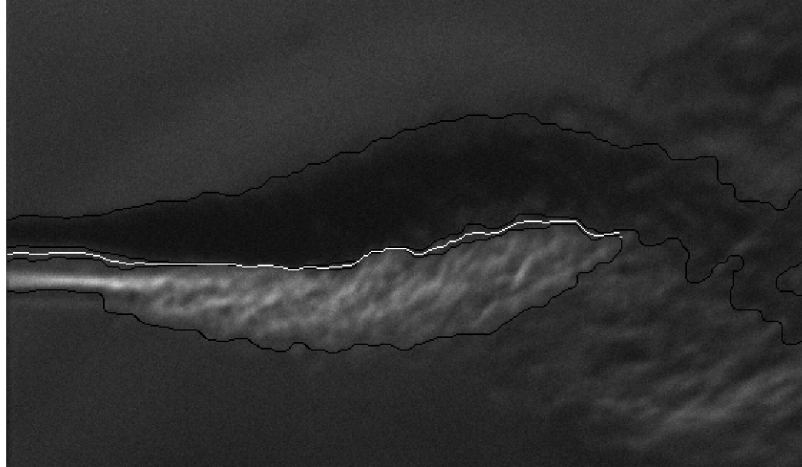


Figure B.5: Original Schlieren image superimposed with edge detection (black line) and median line (white line).

B.4 Harmonic analysis method

The gray intensity of some pixels in the image $c(x, y, t)$ change in time due to the movement of the jet, as can be observed in fig.B.6.

The average oscillation in time $\bar{c}(x, y) = \frac{1}{N} \sum_{t=1}^N c(x, y, t)$ is calculated for every pixel of the image, as shown in fig.B.7, and subtracted from the average:

$$c'(x, y, t) = c(x, y, t) - \bar{c}(x, y)$$

The oscillation frequency of the jet corresponds to that of the excitation and therefore it is possible to fit a sinusoid to the movement each pixel's intensity in time. Every pixel is then projected in sinusoidal bases.

$$c'(x, y, t) = \sum \hat{c}_n(x, y) \exp^{i\omega_0 n t}$$

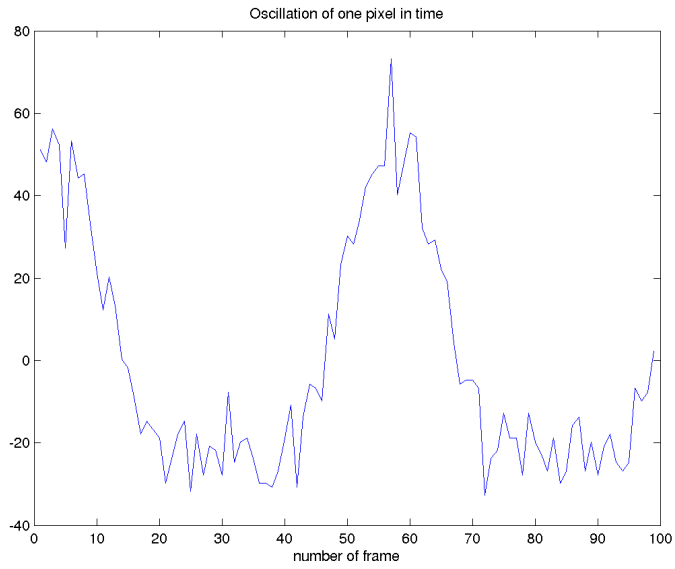


Figure B.6: Evolution of one pixel $c(x, y, t)$ in time

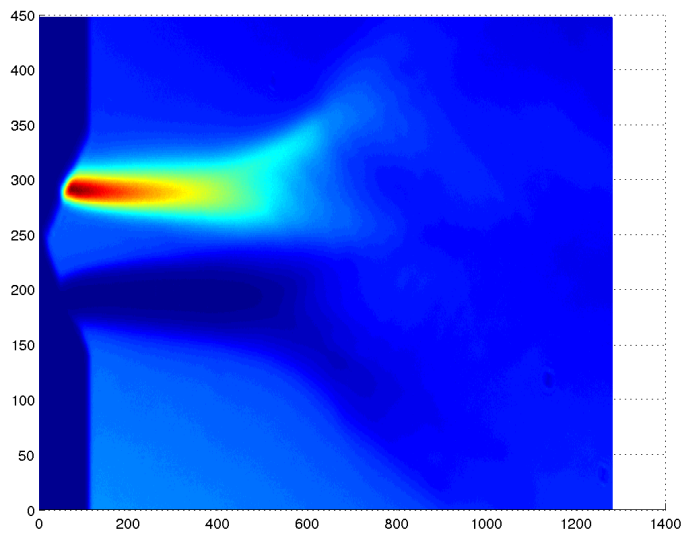


Figure B.7: Continuous value $\bar{c}(x, y)$ for the oscillation of each pixel in time

where ω_0 is the frequency of excitation and n is the number of harmonics included. The amplitude of these sinusoids $\hat{c}_n(x, y)$ are shown in fig.B.8.

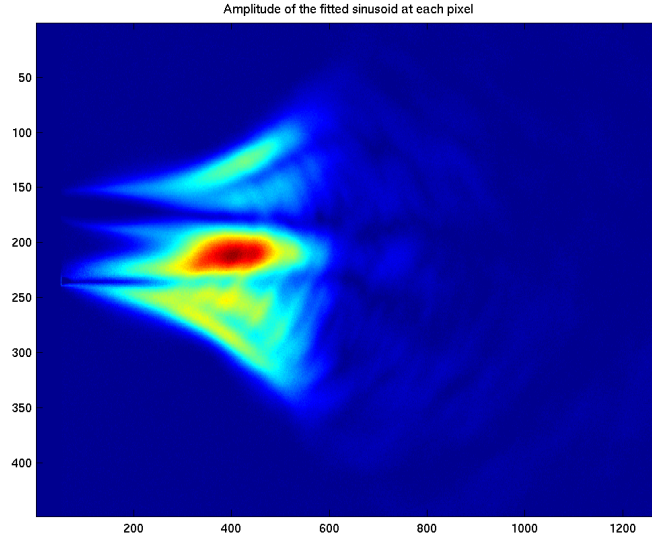


Figure B.8: Amplitude of the fitting sinusoid to each pixel $|\hat{c}_n(x, y)|$.

For each column the energy of the sinusoids are sum:

$$D_n(x) = \sum \hat{c}_n(x, y)^2 \quad (\text{B.5})$$

Fig.B.9 shows the values of $D_n(x)$ for the first four harmonics. It can be shown that the first harmonic $D_0(x)$ grows at the same rate as the amplification growth α_i .

B.5 Data analysis

Since every column of the image oscillates in time at the same frequency, it is possible to fit a sinusoid to each column and obtain the amplitude $|Y(f)|$ and phase $\angle Y(f)$ of the fitted curve:

$$Y(f) = \frac{1}{N} \sum_{i=0}^{N-1} X_i \exp \frac{-j2\pi f}{f_s} \quad (\text{B.6})$$

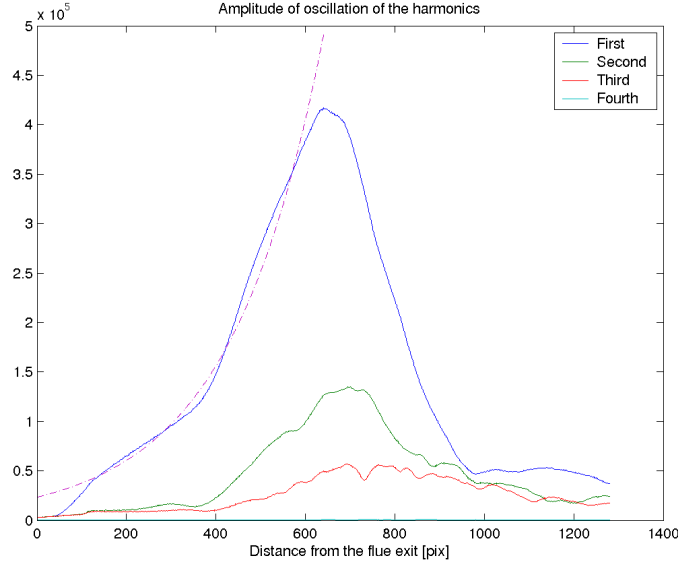


Figure B.9: Integrated amplitudes along the columns, values for the first four harmonics. Linear amplitude

These values are used to recreate a fitted version of the position as shown in Fig.B.10, and to analyze how the perturbation behaves.

Inspired from Rayleigh [72] theory, the experimental data can be analyzed assuming a jet transverse displacement η following :

$$\eta(x, t) = \eta_0 e^{\alpha_i x} e^{i\omega(t-x/c_p)} \quad (\text{B.7})$$

where η_0 represents a complex initial amplitude of the oscillation, α_i is the spatial growing rate and c_p is the convection velocity.

B.6 Methods comparison

The growing rate α_i can be estimated by fitting an exponential to the detected amplitude curve. The convection velocity c_p of the perturbation can be estimated as the slope of the linear fitting to the phase. Fig.B.11 show the fit for a laminar jet ($Re = 500$) with cross-correlation and morphological method.

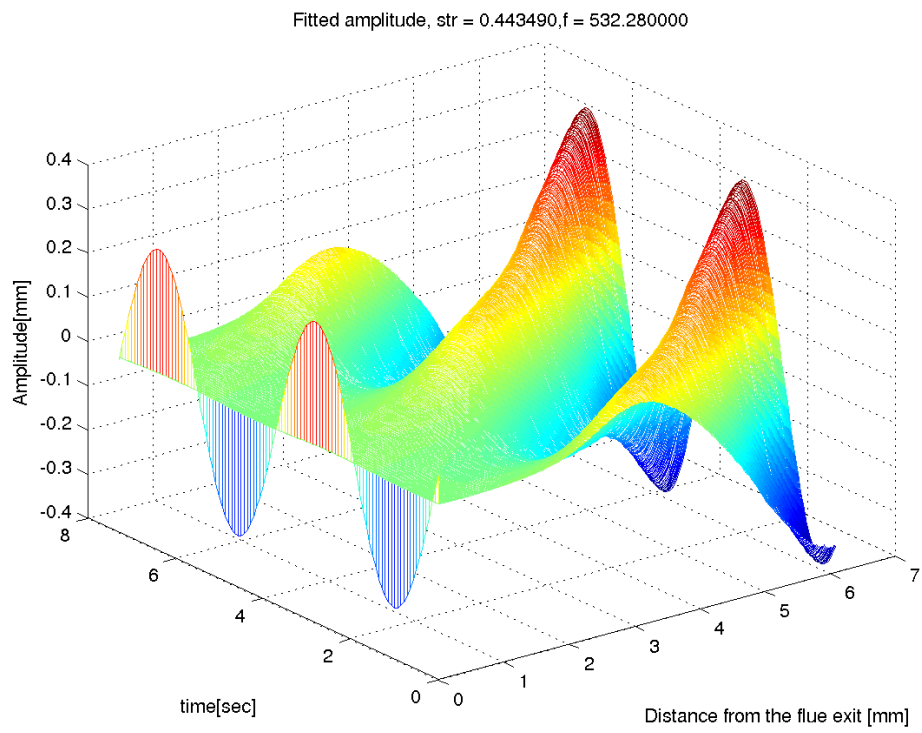


Figure B.10: Fitted position of jet, excitation frequency = 532.28 Hz

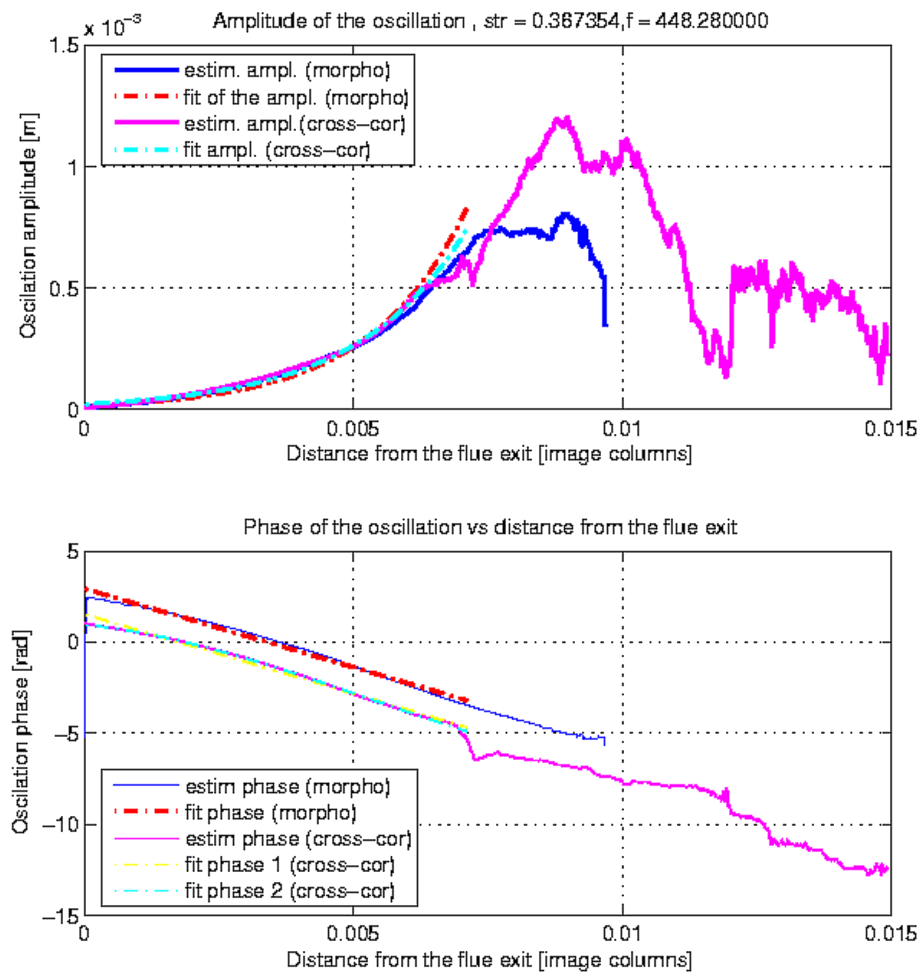


Figure B.11: Amplitude and phase of the jet transverse displacement of the jet using the cross correlation method (pink line) and the morphological method (green line), excitation frequency = 448.28 Hz

, Laminar jet ($Re=500$).

The harmonic analysis method shows to be robust in detecting the amplitude of the perturbation but does not provide an estimation of its phase, therefore is left outside of this comparison. The other two methods show very similar results. The oscillation amplitude follows roughly an exponential up to a distance of $x/h \approx 7$ where h is the thickness of the slit. The phase shift of the oscillation decreases roughly linearly downstream from flue exit, corresponding to the delay induced by the convection of the perturbation on the jet at constant velocity.

Looking closer at the upper part of fig.B.11, the morphological method tracks the oscillation up to larger distances ($x/h \approx 7.5$) than the cross-correlation method ($x/h \approx 6.8$). The morphological method tracks the phase of the oscillation up to distances of $x/h \approx 9.5$ where the amplitude curve clearly shows that the linear description of jet oscillation is no longer valid due to non-linear roll-up of the jet [22] and turbulences [76]. This is due to the ability of the morphological method to extract large scale structures in the flow image.

This ability yields very little advantage to the cross-correlation method in the case of laminar jets but makes the morphological better suited for turbulent jets as shown fig.B.12. The morphological method detects better the amplitude in this case. The slope of the phase shifts increases with distance from flue-exit as expected in the case of a rapidly slowing jet velocity induced by turbulence.

Summarizing, harmonic method estimates only the amplitude of the oscillation on an intra image, column based analysis; cross-correlation method correctly estimates amplitude and phase evolution of the perturbation on a inter-image based analysis, is better suited for laminar jets; morphological method correctly estimates amplitude and phase evolution of the perturbation on an intra-image based analysis, requires heuristic to function and is better suited for turbulent jets.

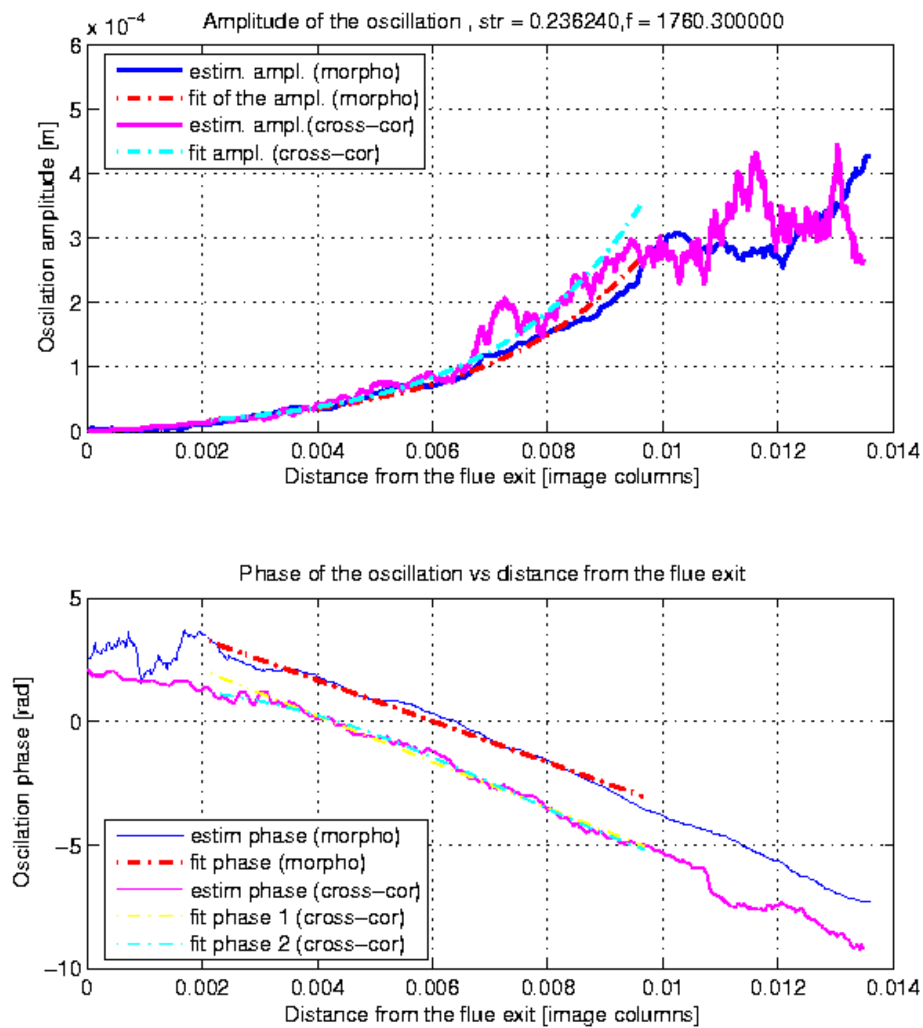


Figure B.12: Amplitude and phase of the jet transverse displacement of the jet using the cross correlation method (pink line) and the morphological method (green line), excitation frequency = 1760.30 Hz, Turbulent jet ($Re=3000$).

Bibliography

- [1] J. Abel and D. Berners. Filter design using second-order peaking and shelving sections. *Proceedings of ICMC 2003, International Computer Music Conference*, September 2003. [93](#)
- [2] S. Arom and F Voisin. Theory and technology in african music. In *The Garland Encyclopaedia of World Music 2 : Africa, New-York, Garland*. in Ruth Stone (ed.), 1998. [106](#)
- [3] S. Arom, F. Voisin, and G. Léothaud. *Experimental Ethnomusicology : An Interactive Approach to the Study of Musical Scales*, in Irne Delige&John Sloboda (ed.). Irène Deliège&John Sloboda, Howe(UK), Erlbaum, Taylor&Francis, 1997. [106](#)
- [4] D.W. Bechert. Excitation of instability waves in free shear layers part 1: theory. *J. Fluid Mech.*, 186:47–62, 1988. [3](#), [7](#), [51](#), [53](#)
- [5] A. H. Benade and J. W. French. Analysis of the flute head joint. *J. Acoust. Soc. Am.*, 37:679–691, 1965. [86](#)
- [6] A.H. Benade. *Fundamentals of Musical Acoustics*. Oxford University Press, Inc., London, 1976. [52](#)
- [7] D. Bernoulli. *Sur le son et sur les tons des tuyaux d’orgue differemment construits*. Memoire, Academie Royale des Sciences, 1762. [2](#)

- [8] P. de la Cuadra C. Vergez and B. Fabre. Jet motion in flute-like instruments: experimental investigation through flow visualization and image processing. *Forum Acusticum. Budapest, Hungary*, 2005. [125](#)
- [9] M. Castellengo. *Contribution à l'étude expérimentale des tuyaux à bouche*. PhD thesis, Université de Paris VI, Paris, France, 1976. [52](#)
- [10] M. Castellengo and B. Fabre. The contemporary transverse flute and the shakuhachi: analysis of performance techniques. *Contemporary Music Review*, 8 (Part 2):217–237, 1994. [53](#)
- [11] R. Caussé, C. Vergez, B. Fabre, C. Ségoufin, and P. de la Cuadra. Developing experimental techniques and physical modeling for ethnomusicology project on oudémé flutes. *Forum Acusticum*, 2002. [9](#)
- [12] J.W. Coltman. Resonance and sounding frequencies of the flute. *J. Acoust. Soc. Am.*, 40:99–107, 1966. [50](#), [61](#)
- [13] J.W. Coltman. Sounding mechanism of the flute and organ pipe. *J. Acoust. Soc. Am.*, 44:983–992, 1968. [2](#), [3](#), [53](#)
- [14] J.W. Coltman. Sound radiation from the mouth of an organ pipe. *J. Acoust. Soc. Am.*, 46:477, 1969. [3](#)
- [15] J.W. Coltman. Mouth resonance effects in the flute. *J. Acoust. Soc. Am.*, 54(2):417–420, 1973. [52](#), [86](#)
- [16] J.W. Coltman. Jet drive mechanism in edge tones and organ pipes. *J. Acoust. Soc. Am.*, 60(3):725–733, September 1976. [3](#), [54](#), [95](#), [96](#)
- [17] J.W. Coltman. Momentum transfer in jet excitation of flute-like instruments. *J. Acoust. Soc. Am.*, 69:1164–1168, 1981.
- [18] J.W. Coltman. Time-domain simulation of the flue. *J. Acoust. Soc. Am.*, 92(1):69–73, July 1992. [52](#), [77](#)

- [19] P. Cook and G. Scavone. The synthesis toolkit (stk). URL: <http://www-ccrma.stanford.edu/software/stk/>, 2000. 99, 112
- [20] L. Cremer and H. Ising. Die selbsterregten Schwingungen von Orgelpfeifen. *Acustica*, 19:143–153, 1967–68. 3, 94
- [21] D.G. Crighton. The edgetone feedback cycle. Linear theory for the operating stages. *J. Fluid Mech.*, 234:361–391, 1992. 3, 7, 51
- [22] P. de la Cuadra and B. Fabre. Analysis of jet instability in flute-like instruments by means of image processing: effect of the excitation amplitude. *ISMA, International Symposium on Musical Acoustics*, 2004. 9, 137
- [23] P. de la Cuadra, B. Fabre, N. Henrich, and T. Robin. Analysis of jet instability in flute-like instruments by means of image processing : effect of the channel geometry on the jet instability. *ICA, 18th International Congress on Acoustics*, 2004. 9, 52, 91
- [24] P. de la Cuadra, A. Master, and C. Sapp. Efficient pitch detection techniques for interactive music. *Proceedings of ICMC 2001, International Computer Music Conference, La Habana, Cuba*, September 2001. 57
- [25] P. de la Cuadra, T. Smyth, C. Chafe, and H. Baoqiang. Waveguide simulation of neolithic chinese flutes. *Proceedings of ISMA, International Symposium on Musical Acoustics, Perugia, Italy*, 2001. 1
- [26] P. de la Cuadra, C. Vergez, and R. Caussé. Use of physical-model synthesis for developing experimental techniques in ethnomusicology- the case of the oudeme flute. *ICMC*, 2002. 9
- [27] S. Dequand. Simplified models of flue instruments : influence of mouth geometry on the sound source. *J. Acoust. Soc. Am.*, 113(3)(3):1724– 1735, 2003. 54, 98
- [28] S.A. Elder. On the mechanism of sound production in organ pipes. *J. Acoust. Soc. Am.*, 54:1554–1564, 1973. 2, 3, 7, 51

- [29] B. Fabre. *La Production de Son dans les Instruments à Embouchure de Flûte: Modèle Aéro-Acoustique pour la Simulation Temporelle*. PhD thesis, Université du Maine, Le Mans, France, 1992. [4](#), [5](#)
- [30] B. Fabre. "les bois". notes from the course "journées pédagogiques physique des instruments de musique". organized by sfa at enst paris. *Available at: www.sfa.asso.fr*, 2000. [1](#)
- [31] B. Fabre. "acoustique des instruments de musique de la famille des flûtes". habilitation à diriger des recherches. *Université Paris 6, Pierre et Marie CURIE*, 2003. [8](#)
- [32] B. Fabre and A. Hirschberg. Physical modeling of flue instruments: a review of lumped models. *Acta Acustica*, 86:599–610, 2000. [3](#), [8](#), [13](#), [20](#), [51](#), [94](#), [108](#)
- [33] B. Fabre, A. Hirschberg, and A.P.J. Wijnands. Vortex shedding in steady oscillations of a flue organ pipe. *Acta Acustica*, 82:811–823, 1996. [3](#), [5](#), [14](#), [53](#), [98](#)
- [34] N. Fernando. A propos de statut de l'octave dans un systeme pentatonique du nord camerun. *Musicae Scientiae, European Society for the Cognitive Sciences of Music*, 1(1):83–95, 2000. [105](#)
- [35] N.H. Fletcher. Acoustical correlates of flute performance technique. *J. Acoust. Soc. Am.*, 57(1):233–237, January 1975. [58](#), [74](#)
- [36] N.H. Fletcher. Jet-drive mechanism in organ pipes. *J. Acoust. Soc. Am.*, 60(2):481–483, August 1976. [3](#)
- [37] N.H. Fletcher. Sound production by organ flue pipes. *J. Acoust. Soc. Am.*, 60(4):926–936, October 1976. [52](#)
- [38] N.H. Fletcher. Transients in the speech of organ flue pipes - a theoretical study. *Acustica*, 34:224–233, 1976.

- [39] N.H. Fletcher. Air flow and sound generation in musical wind instruments. *Ann. Rev. Fluid Mech.*, 11:123–146, 1979. [3](#)
- [40] N.H. Fletcher and L.M. Douglas. Harmonic generation in organ pipes, recorders and flutes. *J. Acoust. Soc. Am.*, 68:767–771, 1980.
- [41] N.H. Fletcher and T.D. Rossing. *The Physics of Musical Instruments*. Springer, New-York, 2nd edition, 1999. [4](#), [52](#)
- [42] N.H. Fletcher and S. Thwaites. Wave propagation on a perturbed jet. *Acustica*, 42:323–334, 1979. [3](#), [13](#), [15](#), [19](#), [52](#), [90](#)
- [43] E. Fléty. Atomic pro: ”a multiple sensor acquisition device. *NIME, Dublin*, 2001. [113](#)
- [44] James Galway. *Flute, Yehudi Menuhin Music Guides*. Kahn & Averil, London, 1990. [50](#), [74](#)
- [45] R. Hänninen and V. Välimäki. An improved digital waveguide model of a flute with fractional delay filters. *Proc. Nordic Acoustical Meeting (NAM’96)*, 1(1):437–444, 1996. [112](#)
- [46] H. Helmholtz. *On the sensation of tone*. Dover edition, NY, 1885. [2](#)
- [47] D.K. Holger, T.A. Wilson, and G.S. Beavers. Fluid mechanics of the edgetone. *J. Acoust. Soc. Am.*, 62(5):1116–1128, November 1977. [3](#), [16](#), [36](#), [38](#), [43](#), [91](#)
- [48] M.S. Howe. Contribution to the theory of aerodynamic sound, with application to excess jet noise and the theory of the flute. *J. Fluid Mech.*, 71:625–673, 1975. [3](#), [7](#), [51](#), [53](#), [98](#)
- [49] T. Smyth J. Abel and J.O. Smith III. A simple, accurate wall loss filter for acoustic tubes. *Proceedings of DAFX 2003, International Conference on Digital Audio Effects, London, England*, September 2003. [83](#)
- [50] L. Kinsler, A. Frey, A. Coppens, and J. Sanders. *Fundamentals of Acoustics*. John Wiley & Sons, Inc, New-York, 4th edition, 2000. [81](#)

- [51] S.G. Krantz. Conformal mappings. *American Scientist*, 87, 1999. 95
- [52] Pijush K. Kundu. *Fluid mechanics*. Academic Pres, Inc., 1st edition, 1990. 95
- [53] J. Lamoine. Etude des propriétés d'un jet turbulent soumis à un champ acoustique transversal. *Rapport de stage, Universit Paris XI-Orsay*, 2001. 108
- [54] O. Macherey. Etude expérimentale dans les flûtes: modélisation de jet turbulent et influence de l'accord du résonateur, rapport de fin détudes ecn. *LAM Paris 6*, 2002. 111
- [55] R.R. Mankbadi. *Transition, turbulence and noise: Theory and applications for scientists and engineers*. Kluwer Academic Publishers, Boston, 2nd edition, 1994. 53
- [56] E. N. Marieb. *Human anatomy an physiology*. Addison Wesley Longman, Inc, Boston, MA, USA, 4th edition, 1998. 67
- [57] G.E. Mattingly and W.O. Criminale. Disturbance characteristics in a plane jet. *Phys. Fluids*, 14(11):2258–2264, 1971. 13, 18, 20, 30, 34, 52, 91
- [58] Max/MSP. Real-time audio development environment. *URL: <http://www.cycling74.com>*, 2000. 112
- [59] M.E. McIntyre, R.T. Schumacher, and J. Woodhouse. On the oscillations of musical instruments. *J. Acoust. Soc. Am.*, 74(5):1325–1345, November 1983. 3, 77
- [60] M. Meissner. Aerodynamically excited acoustic oscillations in cavity resonator exposed to an air jet. *Acustica/ Acta Acustica*, 88:387–400, 2002. 5, 54
- [61] M. Mersenne. *Harmonie Universelle*. Facsimil edition from CNRS, 1636. 2
- [62] W. Merzkirch. *Flow Visualization*. Academic Press, New-York, 1974. 14, 24, 117
- [63] C.J. Nederveen. *Acoustical aspects of woodwind instruments*. Northern Illinois University Press, De Kalb, 2nd edition, 1998. 52

- [64] A.W. Nolle. Sinuous instability of a planar air jet: Propagation parameters and acoustic excitation. *J. Acoust. Soc. Am.*, 103:3690–3705, 1998. [5](#), [17](#), [18](#), [19](#), [20](#), [34](#), [52](#), [91](#)
- [65] C. Nouvel. Synthèse sonore de sons de flûte par modèles physiques: influence de la modélisation du jet. rapport de stage de fin d'études supelec/dea traitement du signal et automatique. *LAM Paris 6*, 2002. [83](#)
- [66] N. Montgermont P. de la Cuadra, B. Fabre and C. Chafe. Analysis of flute control parameters: A comparison between a novice and an experienced flautist. *Submitten to J. Acoust. Soc. Am.*, 2005. [9](#)
- [67] N. Montgermont P. de la Cuadra, B. Fabre and L De Ryck. Analysis of flute control parameters: A comparison between a novice and an experienced flautist. *Forum Acusticum. Budapest, Hungary*, 2005. [9](#)
- [68] A.D. Pierce. *Acoustics: an Introduction to its Principles and Applications*. McGraw-Hill Book Company, New-York, 1981. Also available from the Acoustical Society of America, 1990. [80](#)
- [69] A. Powell. On the edgetone. *J. Acoust. Soc. Am.*, 33(4):395–409, April 1961. [3](#), [4](#), [15](#), [98](#)
- [70] Prandtl and Tietjens. *Fundamentals of Hydro and Aeromechanics*. Dover, New-York, 1934. [19](#)
- [71] Qt. Qt a comprehensive c++ application development framework. *URL: <http://www.trolltech.com>*, 2005. [101](#)
- [72] Lord Rayleigh. *The Theory of Sound*. Dover, reprint (1945), New-York, 1894. [2](#), [13](#), [14](#), [16](#), [19](#), [52](#), [53](#), [91](#), [134](#)
- [73] H. Sato. The stability and transition of a two-dimensional jet. *J. Fluid Mech.*, 7:53–80, 1960. [13](#)

- [74] G. Scavone and J. O. Smith. Digital waveguide modeling of woodwind toneholes. *Proceedings of ICMC 1997, International Computer Music Conference, Thessaloniki, Greece*, September 1997. 79, 80
- [75] C. Ségoufin. *Production du son par interaction écoulement / résonateur acoustique : influence du système amont et application à la flûte à bec*. Phd thesis, Université de Paris 6, Paris, France, 2000. 5, 18, 91
- [76] C. Ségoufin, B. Fabre, and L. de Lacombe. Experimental investigation of the flue channel geometry influence on edge-tone oscillations. *Acustica/Acta Acustica*, 90:966,975, 2004. 15, 16, 20, 30, 52, 137
- [77] C. Ségoufin, B. Fabre, M.P. Verge, A. Hirschberg, and A.P.J. Wijnands. Experimental study of the influence of the mouth geometry on sound production in a recorder-like instrument: Windway length and chamfers. *Acta Acustica*, 86:599–610, 2000. 16, 20, 52, 61
- [78] J.O. Smith. Physical modeling using digital waveguides. *Computer Music J.*, 16(4):75–87, 1992. 79
- [79] J.O. Smith. Physical modeling using digital waveguides. *Computer Music Journal*, 4(16):74–87, 1992. 112
- [80] S. Thwaites and N.H. Fletcher. Wave propagation on turbulent jet i. *Acustica*, 45:175–179, 1980. 53, 110
- [81] S. Thwaites and N.H. Fletcher. Wave propagation on turbulent jet ii. *Acustica*, 51:44–49, 1982. 53
- [82] Nancy Toff. *The flute book, a complete guide for students and performers*. Oxford University Press, New-York, 1996. 50
- [83] D.J. Tritton. *Physical fluid dynamics*. Oxford University Press, New-York, 2nd edition, 1998. 53

- [84] M.P. Verge. *Aeroacoustics of confined jets, with application to the physical modeling of recorder-like instruments*. Phd thesis, Eindhoven University of technology, The Netherlands, 1995. [3](#), [5](#), [13](#), [15](#), [17](#), [18](#), [20](#), [53](#), [90](#), [108](#)
- [85] M.P. Verge, R. Caussé, B. Fabre, A. Hirschberg, A.P.J. Wijnands, and A. van Steenbergen. Jet oscillations and jet drive in recorder-like instruments. *Acta Acustica*, 2:403–419, October 1994. [3](#), [5](#), [6](#), [38](#), [54](#)
- [86] M.P. Verge, B. Fabre, W.E.A. Mahu, A. Hirschberg, R. van Hassel, A.P.J. Wijnands, J.J. de Vries, and C.J. Hogendoorn. Jet formation and jet velocity fluctuations in a flue organ pipe. *J. Acoust. Soc. Am.*, 95(2):1119–1132, February 1994. [3](#), [54](#)
- [87] M.P. Verge, A. Hirschberg, and R. Caussé. Sound production in recorder-like instrument ii a simulation model. *J. Acoust. Soc. Amer.*, 101:2925–2939, 1997. [3](#), [52](#), [78](#), [91](#), [95](#), [112](#)
- [88] V. Vlimki. Fractional Delay Waveguide Modeling of Acoustic Tubes. Technical Report Report 34, Helsinki University of Technology, Faculty of Electrical Engineering, Laboratory of Acoustic and Audio Signal Processing, July 1994. [80](#)
- [89] J. Wolf, J. Smith, J. Tann, and N. Fletcher. Acoustic impedances of classical and modern flutes. *Journal of Sound and Vibration*, 2000. [2](#), [52](#), [86](#)